

Master of Science Thesis
Delft University of Technology - Faculty of Aerospace Engineering

Natural gas displacement by wind curtailment utilization in combined-cycle power plants

by

F.S.C. van den Oudenalder



Natural gas displacement by wind curtailment utilization in combined-cycle power plants

by

F.S.C. van den Oudenalder

to obtain the degree of Master of Science

at the Delft University of Technology,

to be defended publicly on Friday November 11, 2016 at 09:00 AM.

Student number: 4084160
Project duration: January 7, 2016 – November 11, 2016
Thesis committee: Prof. G. van Bussel, TU Delft, chairman
Prof. dr. ir. S.A. Klein, TU Delft
Dr. A. Gangoli Rao, TU Delft, supervisor

An electronic version of this thesis is available at <http://repository.tudelft.nl/>.

Acknowledgements

During my time as a student at the faculty of Aerospace Engineering I have learned more than I could have imagined. I hoped to learn about the design of aircraft and spacecraft, little did I know that I would learn about teamwork, friendship and failure. My thanks go to the wonderful people I have met during my time in Delft, Ames and Gothenburg. I would like to thank the colleagues I have had to pleasure of working with throughout the years. Without you the last few years would have never been as great and as amusing. I learned a great deal from all of you and had a lot of fun while doing so.

I would like to thank all the wonderful roommates I have had, both in the Netherlands and abroad, most of which became very close friends. Thank you for the great talks, trips and arguments. Finally, I would like to express my gratitude to the following persons:

Arvind Gangoli Rao - Thank you for your guidance, good advice and positive attitude throughout the entire project. It gave me a great deal of confidence and support to have you as my supervisor.

Sikke Klein - Thank you for your participation, positive attitude and knowledge with respect to combined-cycle power plants and their operation. Your involvement has greatly improved the quality of my thesis and my understanding of power plants, gas turbines and the electrical grid.

Theo Woudstra - Thank you for your kindness and extensive help with the Cycle-Tempo simulation software. Your continued efforts greatly enhanced my understanding of combined-cycle power plants and the means to simulate their performance.

Wilfried Visser - Thank you for your help on creating a model to simulate the performance of the Siemens SGT5-4000F gas turbine in GSP. Without your help I would never been able to capture certain features within the model.

Kenneth Martina - It was a great experience to visit the Sloecentrale. It was great to get the opportunity to see a real combined-cycle power plant in operation. Thank you for this opportunity.

Carlo De Servi & Mauro Gallo - Thank you both for your help with how to approach the simulation of a thermal energy storage. I appreciate your kindness and helpfulness whenever I came by without notice.

Jessica Dahlkvist - Thank you for always understanding and supporting me. Your support means a lot to me and has made my time as a student unforgettable.

Roderick van den Oudenalder - Thank you for the great confidence you have in me. Your perseverance has shown me that everything is possible as long as you believe in it.

Wilhelmina van den Oudenalder & George Attalla - I would like to express my deepest gratitude to my parents for their endless support, the freedom they have given me and for always believing in me. Without you I would have never been able to graduate. Your love and support will never be forgotten.

Thank you,

Frederick van den Oudenalder

Table of Contents

1	Introduction	17
1.1	Problem Definition and Significance	17
1.2	Research Topic Motivation	17
1.3	Research Objective and Research Questions	18
1.4	Report Structure	19
2	Constrained and Curtailed Wind	21
2.1	Constrained Wind versus Curtailed Wind	21
2.2	Curtailment Causes	22
2.3	Conclusions and Observations	23
3	Curtailment Modelling	25
3.1	Model Structure and Underlying Equations	25
3.2	Verification	26
3.3	Results	26
3.4	Conclusions and Observations	27
4	Combined-Cycle Power Plants	31
4.1	Power Plant Architecture	31
4.1.1	Gas Turbine	32
4.1.2	Heat Recovery Steam Generator	32
	Multiple Pressure Stages	33
	HRSG Variants	33
4.1.3	Steam Turbine	34
4.2	Thermodynamic Principles of the Combined-Cycle Power Plant	35
4.3	Conclusions and Observations	36
5	Combined-cycle Power Plant Modelling	39
5.1	Power Plant Selection	39
5.1.1	Technical Data	39
5.2	Gas Turbine Modelling	40
5.2.1	THERMOFLEX	41
5.2.2	GSP	41
5.2.3	Cycle-Tempo	41
5.2.4	Results	43
	Design Point Performance	43
	Off-design Performance	43
5.3	Combined-cycle Modelling	46
5.3.1	THERMOFLEX	46
5.3.2	Cycle-Tempo	46
5.4	Results	47
	Design Point Performance	47
	Off-design Performance	47

5.5	Validation	49
5.5.1	Gas Turbine Validation	49
5.5.2	Combined-Cycle Validation	49
5.5.3	Annual Performance	49
5.6	Conclusions and Observations	51
6	Energy Storage	53
6.1	Curtailement and CCPP Operation	53
6.2	Energy Storage Methods	53
6.2.1	Electrical Storage	54
	Supercapacitors	54
	Superconducting Magnetic Energy Storage (SMES)	54
6.2.2	Mechanical Storage	54
	Pumped Hydroelectric Storage (PHS)	54
	Compressed Air Energy Storage (CAES)	54
	Flywheel Energy Storage (FES)	54
6.2.3	Thermal Storage	55
	Sensible Heat Storage (SHS)	55
	Latent Heat Storage (LHS)	55
	Thermochemical Heat Storage (THS)	55
	Cryogenic Energy Storage (CES)	55
	Salts	55
6.2.4	Chemical Storage	56
	Hydrogen	56
	Batteries	56
	Flow Batteries	56
6.3	Techno-economic Performance Overview	56
6.4	Conclusions and Observations	57
7	Curtailement Utilization	61
7.1	Most Beneficial Location of Energy Addition	61
7.2	Maximum Transferable Energy	63
	7.2.1 Natural Gas Heating	63
	7.2.2 Air Heating	63
7.3	Ease of Energy Transfer to Gas	64
7.4	Practical Considerations	66
	7.4.1 In favour of natural gas heating	66
	7.4.2 In favour of compressor exhaust heating	66
7.5	Conclusions and Observations	66
8	Energy Storage Design and Modelling	69
8.1	Storage Layout	69
8.2	Phase Change Material Selection	70
8.3	Thermal Storage Modelling	71
	8.3.1 Underlying Assumptions	71
	8.3.2 Governing Equations and the Finite Difference Method	72
	8.3.3 Enthalpy method	75
	8.3.4 Heat Transfer Fluid Heating and Movement	75
	8.3.5 Heat Transfer Coefficient	76
	8.3.6 Natural Convection in the PCM	76
	8.3.7 Impact of Wall Presence	77
8.4	Numerical Errors	78
8.5	Grid Convergence	78
8.6	Verification and Validation	79
8.7	Results	80

8.8	Sensitivity Study	81
8.8.1	Effect of Module Dimensions	82
8.8.2	Effect of PCM properties	82
8.9	Conclusions and Observations	84
9	Annual Performance	87
9.1	Methodology	87
9.2	Results	88
9.3	Conclusions and Observations	90
10	Financial Feasibility	93
10.1	Financial Benefits	93
10.2	Investment Costs	94
10.3	Payback Period	94
10.4	Results	95
10.5	Environmental Performance as compared to Wind Energy	97
10.6	Conclusions and Observations	98
11	Conclusions and Recommendations	101
11.1	Recommendations for Future Research	102
A		111
A.1	Hemweg 9 Operating Pattern (2015)	111
A.2	Software Characteristics and Model Architectures	112
A.3	Gas Turbine and Combined-cycle Simulation Settings	115
A.4	Gas Turbine Performance Literature	117
A.5	Temperature-density Curve for Methane	119
A.6	Grid Convergence Studies for Swept Parameters	119

List of Figures

1.1	Schematic of curtailment utilization in combined-cycle power plants.	18
1.2	Report outline.	19
2.1	Schematic of constrained and curtailed wind.	22
2.2	Schematic of frequency control. Modified from (20).	22
3.1	Curtailment model for the Netherlands at 30% wind penetration, 50% SNSP and 20% RR.	26
3.2	Verification cases.	27
3.3	Influence of SNSP and RR limits on curtailment for various wind penetration levels.	27
4.1	Multi-shaft combined-cycle power plant layout. Modified from (25).	31
4.2	Schematic of gas turbine gas path. Modified from (26).	32
4.3	T-s diagram for the ideal Brayton cycle.	32
4.4	Temperature profile through the superheater, evaporator and economizer for a single-stage HRSG. The orange line represents the hot flue-gases and the blue line the feedwater/steam.	33
4.5	Temperature profile through the superheater, evaporator and economizer for a three-stage pressure HRSG. The orange line represents the hot flue-gases and the blue line the feedwater/steam.	33
4.8	The efficiency of a simple Brayton cycle and a combined-cycle plant as a function of the gas turbine turbine inlet temperature and pressure ratio. Modified from (26).	36
5.1	Normalized operating pattern for the Hemweg 9 for 2015(36).	40
5.2	SGT5-4000F model in THERMOFLEX.	41
5.3	SGT5-4000F model in GSP.	42
5.4	Steam cycle architecture in Cycle-Tempo.	42
5.5	SGT5-4000F model in Cycle-Tempo.	43
5.6	Siemens SGT5-4000F off-design simulation results for THERMOFLEX (TF), GSP and Cycle-Tempo (CT) at ISO conditions.	45
5.7	Combined-cycle model architecture in THERMOFLEX.	46
5.8	Combined-cycle model architecture in Cycle-Tempo.	47
5.9	Combined-cycle off-design simulation results for THERMOFLEX (TF), GSP and Cycle-Tempo (CT) at ISO conditions.	48
5.10	Model validation(26; 8).	49
5.11	Annual gross thermal efficiency and fuel mass flow patterns.	50
5.12	Annual occurrence distribution for the gross thermal efficiency and fuel mass flow.	50
6.1	Time of day distributions for the occurrence of curtailment at 30% wind penetration and the Hemweg 9 operating pattern for 2015.	53
6.2	Energy storage categories and corresponding principles.	54
7.1	Heat transfer coefficient difference between air and methane for turbulent flow over a flat plate.	65
7.2	Heat transfer coefficient difference between air and methane for turbulent flow in a smooth pipe.	66
8.1	Schematic of the storage module. Modified from (87).	69
8.2	Cylindrical module cross-sectional cut-out schematic.	70
8.3	Generic mesh for PCM and HTF temperature field simulation in a hollow cylinder. Modified from (95).	72
8.5	Influence of grid density on the heat transfer fluid exhaust temperature profile (number of nodes in r-direction times number of nodes in z-direction).	79
8.6	Heat transfer fluid exhaust temperature as a function of time. The results are compared to similar simulations(87; 104).	80
8.7	Numerical simulation results for the heat transfer fluid heating for one storage module.	81
8.8	Effects of module dimensions and PCM properties on HTF exhaust profile.	83
9.1	Model integration N2 chart.	87
9.2	Illustrative simulation result.	88

9.3	Annual fuel savings for different wind penetration levels and storage module dimensions.	89
9.4	Annual reduction of CO ₂ emissions for different wind penetration levels and storage module sizes. . .	90
10.1	European natural gas prices for industrial consumers for the year 2015(105).	93
10.2	Payback periods for various module lengths (All penetration levels).	95
10.3	Payback periods for various module inner radii (All penetration levels).	96
10.4	Payback periods for various module lengths.	96
10.5	Payback periods for various module inner radii.	97
A.1	Normalized operating pattern for the Hemweg 9 during the year 2015(36).	111
A.2	Operating pattern occurrences for the Hemweg 9 during the year 2015(36).	111
A.3	Combined-cycle model architecture in THERMOFLEX.	113
A.4	Combined-cycle model architecture in Cycle-Tempo.	114
A.5	Part-load efficiencies for the gas turbine and combined-cycle(26).	117
A.6	Influence of SGT5-4000F development steps. Step one allows a further decrease of minimum compressor air mass flow. Step two includes a modified burner design which enabled a high exhaust gas temperature. Step three lead to a further increase in turbine exhaust temperature(47).	118
A.7	Temperature-density curve for methane at 18.25 bar(82).	119
A.8	Convergence study for the longest module length.	119
A.9	Convergence study for the largest module inner radius.	119

List of Tables

5.1	Reference plant gas turbine, steam turbine, generator and fuel specifications (37; 38; 39; 41; 42)	40
5.2	Design point simulation results for THERMOFLEX, GSP and Cycle-Tempo at ISO conditions.	43
5.3	Combined-cycle design point simulation results at ISO conditions(40).	47
5.4	Annual power plant performance (2015).	51
6.1	Thermal energy storage concept comparison. Based on (61).	55
6.2	Salt compositions characteristics. Modified from (62).	56
6.3	Energy storage techno-economic characteristics. Modified from (10).	57
6.4	Continuation of energy storage techno-economic characteristics. Modified from (10).	57
7.1	Estimated maximum annual fuel savings for Slochteren gas heating.	63
7.2	Estimated maximum annual fuel savings for air heating.	64
7.3	Gas properties of air and natural gas (methane) at several temperatures at 18.25 bar.	65
7.4	Most favourable option per criterion.	67
8.1	Phase changing material candidates.	71
8.2	A164 material properties(91).	71
8.3	Simulation parameters.	77
8.4	Simulation parameters(104).	80
10.1	Annual balance sheet.	94
10.2	$\lambda_{CCPP}/\lambda_{WT}$ ratios for different storage module lengths and inner radii. Red values indicate that $\lambda_{CCPP} > \lambda_{WT}$	98
A.1	Combined-cycle modelling software characteristics.	112
A.2	Gas turbine simulation settings.	115
A.3	Combined-cycle simulation settings.	116

List of Symbols

Latin Symbols

\dot{m}	Mass flow
A	Area
C_p	Specific heat capacity
$C_{maintenance}$	Maintenance costs
$C_{p,air}$	Specific heat capacity of the air
$C_{p,gas}$	Specific heat capacity of the gas
$C_{p,solid}$	Specific heat capacity of the PCM in solid phase
$C_{p,liquid}$	Specific heat capacity of the PCM in liquid phase
C_{total}	Total costs
E	Energy
g	Gravitational acceleration
h	Enthalpy
h_{sl}	Latent heat of fusion
k	Thermal conductivity
k_{eff}	Effective thermal conductivity
k_{liquid}	Thermal conductivity of the PCM in liquid phase
k_{solid}	Thermal conductivity of the PCM in solid phase
L	Length
Nu	Nussel number
P	Power
$P_{Brayton}$	Output power from Brayton cycle
P_{demand}	Demand Power
$P_{Rankine}$	Output power from Rankine cycle
$P_{residual}$	Residual Power
$P_{wind\ production}$	Generated Wind Power
Pr	Prandtl number
Q	Thermal energy heat rate
r_a	Lower r-coordinate of the PCM node control volume element
r_a	Upper r-coordinate of the PCM node control volume element
r_i	Inner radius
r_o	Outer radius
R_{total}	Total thermal resistance
Ra_x	Rayleigh number for length/diameter x

Re_x	Reynolds number for length/diameter x
T	Temperature
T_m	Melting temperature of the PCM
T_∞	Heat transfer fluid temperature where convection takes place
T_{cold}	Temperature of cold side
$T_{exhaust}$	Exhaust temperature
T_{hot}	Temperature of hold side
T_{max}	Maximum temperature
t_o	Time period
$T_{surface}$	Surface temperature where convection takes place
U	Heat transfer coefficient
V	Velocity

Greek Symbols

α	Thermal diffusivity
β	Thermal expansion coefficient of the PCM
ΔE	Energy change
$\Delta E_{boundary}$	Energy transfer through the boundary
ΔE_{HTF}	Energy change of the HTF
ΔE_{PCM}	Energy change of the PCM
Δr	Step size in r-direction
ΔT	Temperature difference
Δt	Time step
Δz	Step size in z-direction
$\eta_{Brayton}$	Brayton cycle efficiency
η_{carnot}	Carnot efficiency
η_{cc}	Combustion efficiency
$\eta_{Rankine}$	Rankine cycle efficiency
$\eta_{th,CCPP}$	Combined-cycle thermal efficiency
η_{th}	Thermal efficiency
λ_{CCPP}	Price per kg reduction in CO ₂ for combined-cycles
λ_{WT}	Price per kg reduction in CO ₂ for wind turbines
μ	Dynamic viscosity
ν	Kinematic viscosity
π	Mathematical constant pi
ρ	Density
τ_{TES}	Lifespan of a thermal storage
τ_{WT}	Lifespan of a wind turbine

Superscripts

t	Index for time
-----	----------------

Subscripts

$Boundary$	Boundary between HTF and PCM
$CCPP$	Combined-cycle power plant

<i>HTF</i>	Heat transfer fluid
<i>i</i>	Index for nodes in r-direction
<i>j</i>	Index for nodes in z-direction
<i>PCM</i>	Phase change material
<i>TES</i>	Thermal energy storage
<i>WT</i>	Wind turbine

Other Symbols

\mathcal{O}	Higher order terms
---------------	--------------------

List of Abbreviations

CAES . Compressed Air Energy Storage	ISO International Organization for Standardization
CC Combined Cycle	LHS ... Latent Heat Storage
CCPP . Combined Cycle Power Plant	LHV ... Lower Heating Value
CES ... Cryogenic Energy Storage	LP Low Pressure
CHP ... Combined Heat and Power	MP Medium Pressure
CO₂ ... Carbon-dioxide	MToe .. Million Tons of Oil Equivalent
CT Cycle-Tempo	MWI .. Modified Wobbe Index
ES Energy Storage	NLR ... Nederlands Lucht- en Ruimtevaartcentrum
ETS ... Emissions Trading System	PBP ... Payback Period
EU European Union	PCM .. Phase Changing Material
EUR ... Euro (Currency)	PHS ... Pumped Hydroelectric Storage
EWEA European Wind Energy Association	PR Pressure Ratio
FDM .. Finite Difference Method	RPM .. Rounds Per Minute
FES Flywheel Energy Storage	RR Regulating and Reserve
GSP ... Gas turbine Simulation Programme	SHS ... Sensible Heat Storage
HP High Pressure	SMES . Superconducting Magnetic Energy Storage
HRSG . Heat Recovery Steam Generator	SNSP .. System Non-Synchronous Penetration
HTC ... Heat Transfer Coefficient	THS ... Thermochemical Heat Storage
HTF ... Heat Transfer Fluid	TF THERMOFLEX
IGV ... Inlet Guide Vanes	TIT Turbine Inlet Temperature
IRES .. Intermittent Renewable Energy Sources	

"Humanity's deepest desire for knowledge is justification enough for our continuing quest. And our goal is nothing less than a complete description of the universe we live in"

Stephen Hawking, A Brief History of Time

Chapter 1

Introduction

This chapter aims to fulfil several goals. The first is to define the problem at hand and to give the reader essential background information regarding the occurrence of this problem. This is succeeded by a short elaboration on the motivation of the research topic and research done previously to solve the problem at hand. Secondly, the research project documented within this report is then described in terms of one central research objective and several key research questions. These questions are answered throughout this report. Finally, a short outline of the thesis report is presented to provide a better overview of which steps are taken to successfully achieve the set research objective.

1.1 Problem Definition and Significance

The world's energy need has drastically increased over the last decades. This resulted from a growth in global population and higher global standards of living. This comes with several environmental challenges to support our way of living for a long period of time. Many of these challenges are dominated by global warming originating from the use of non-renewable energy sources and by releasing their by-products into the atmosphere. This negative consequence has led to extensive research into cleaner and renewable energy sources. Twenty-seven member countries from the European Union (EU) have set targets to achieve 20% of their total energy generation to be delivered solely by renewable sources by 2020. EU targets also include a reduction of greenhouse gases by 20% compared to 1990(1). As a result of these new targets, the share of renewable energy in the generation mix has increased over the recent years(2; 3). The share of intermittent renewable energies has not only increased in the last couple of years but will grow at an even faster pace in the years to come(4; 5; 6). Renewable energy sources consist, amongst others, out of intermittent renewable energy sources (IRES). These provide a fluctuating power output. To account for the output of IRES, thermal generators must reduce their power production, leading to lower electrical efficiencies as they move away from their optimal operating point(7; 8). This is not possible for every generator since wind fluctuations can occur within minutes and not every plant can respond so abruptly such as nuclear and coal power plants. Therefore, combined-cycle power plants (CCPPs) are often used for "load balancing" due to their current flexibility. Due to the fluctuating nature of IRES, there are times when their output is not allowed into the grid due to stability reasons or when there is a mismatch between the power supply and demand. During such times an excess of power is present, and when no use is found for this excess of power, wind turbines are dispatched-down: they are shut-down although they are perfectly capable of producing power. The amount of wind energy which could have been produced if the turbines were running is called constrained wind or curtailment. Under which of these categories the dispatch-down of wind turbines falls is discussed in detail in chapter 2. As the market share of IRES increases and wind is to be dispatched down more often. If more wind turbines are to be dispatched down, the business case for wind parks becomes less profitable and their attractiveness decreases. To continuously harvest the positive effects of wind power and extract their full potential, the growth of renewable energy sources must be encouraged rather than limited. It is therefore important that its corresponding integration challenges regarding the dispatch down of wind turbines must be resolved to achieve a higher share of renewable energy sources within the electricity grid.

1.2 Research Topic Motivation

The presence of unused excess power has been a popular topic of research. To avoid its occurrence, several solutions have been proposed, each trying to solve a different aspect. A promising idea is to use large scale energy storage(9; 10; 11; 12; 13; 14). The proposed concept is rather straightforward: store energy during periods of low demand and release it during periods of high demand. Another method is to adjust the power demand pattern to better match that of power supply. This is already in effect in the Netherlands by having a variable electricity price based on the time of day. A solution for the presence of excess power not often addressed, is the introduction of new

loads into the grid. Currently a power plant is mainly used as a generator and not as a consumer. Allowing the plant to extract power from the grid can lead to a displacement of fossil fuels. Instead of powering the plant solely by burning fossil fuels, one can (partly) power it with the excess power coming from IRES as visualized in Figure 1.1. Therefore, the goal of this research is to assess the technical and financial feasibility of utilizing wind curtailment in a combined-cycle power plant by simulating the annual performance of a such a power plant.

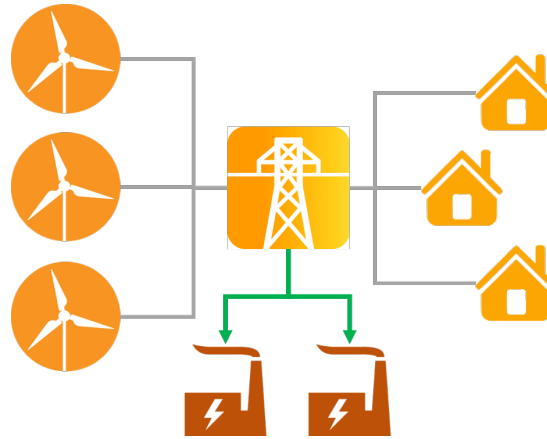


Figure 1.1: Schematic of curtailment utilization in combined-cycle power plants.

A similar idea has been investigated to quantify the impact of using excess power for the heating sector instead of the electricity sector(15). It is therefore that the impact of such a solution for the electricity sector is investigated within this research project. To further limit the scope of the project, the object of observation is chosen to be a combined-cycle power plant. This type of plant was chosen due to its current success and increasing role in the integration of IRES. The main focus of this research lies on the Dutch grid and the performance of Dutch CCPPs. It is therefore that most cases are applied to the Dutch grid.

1.3 Research Objective and Research Questions

This research project starts with the definition of a clear and unambiguous research objective. This objective indicates the aim of the project and how this aim is to be achieved. For this research project the following research objective is established:

The research objective is to assess the technical and financial feasibility of utilizing wind curtailment in a combined-cycle power plant by simulating the annual performance of a such a modified power plant

This research objective is divided into five main research questions. The research objective is achieved once all of these questions have been answered. These questions were identified through the creation of a research framework as described in "Designing a Research Project" (16). The research questions answered throughout this report are as follows:

1. What are the current and future levels of excess power available for combined-cycle power plants coming from the dispatch down of wind turbines?
2. Which combined-cycle architecture modification displays potential to improve existing plants in view of the set assessment criteria?
3. What are the performance scores of the current and modified combined-cycle architectures for each of the assessment criteria?
4. What can one conclude from the performance scores of the simulated plant architectures to access whether using curtailment in combined-cycles is technically and financially feasible?

1.4 Report Structure

This report consists of 11 main chapters. The first is the introduction, which you are reading at this moment. It is followed by chapter 2 which elaborates on the dispatch down of wind turbines and its subtypes: constrained and curtailed wind. The knowledge gained from this chapter is used in chapter 3 to create a curtailment model used to quantify curtailment for a specific electrical grid. This model is the first of three models to be developed to quantify the benefits of using wind curtailment. The subsequent chapter, chapter 4, describes the working principles of a combined-cycle power plant. This knowledge is used in chapter 5 to create the second model, the combined-cycle model which simulates power plant performance during full-load and part-load conditions. Chapter 6 provides an overview of energy storage methods and the principles upon which they are based. Within this chapter, one storage method is chosen to match the curtailment occurrences with the combined-cycle operating pattern. This chapter is followed by chapter 7 which describes and evaluates several possible methods for which curtailment can be utilized in combined-cycle plants. Here the decision is made on how to best use curtailment to displace natural gas. A energy storage system based on the findings from chapter 6 is then designed and simulated in chapter 8. This model is the final of the three models. These three models are integrated together to simulate the annual performance for curtailment utilization. The findings of this simulation are presented in chapter 9. Chapter 10 deals with the financial health of the proposed concept and its financial performance as compared to the installation of wind turbines. The final chapter, chapter 11, concludes the research project and presents recommendations for future work. The complete report outline is visualised in Figure 1.2.

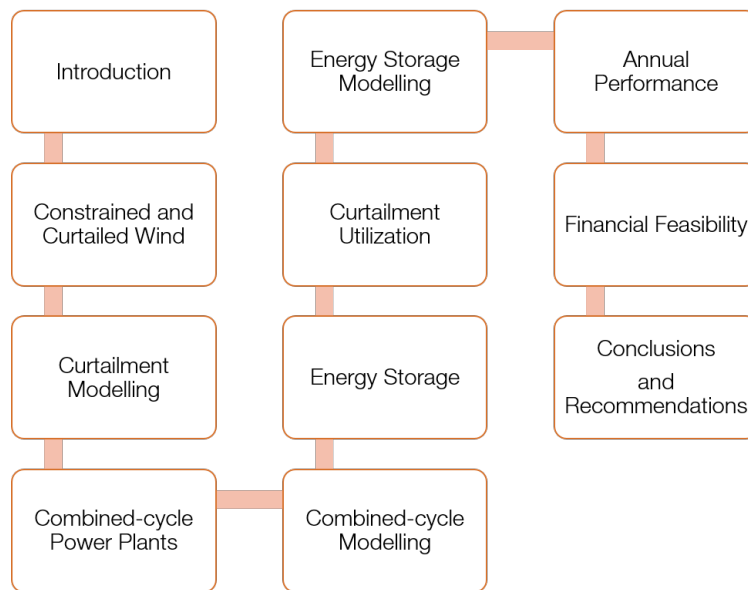


Figure 1.2: Report outline.

Chapter 2

Constrained and Curtailed Wind

This chapter explains the definition of constrained wind and its difference in comparison to curtailed wind. The main causes for curtailed wind, also known as curtailment, are identified and elaborated upon. This knowledge gained forms the basis for the curtailment model developed in chapter 3, capable of simulating the occurrence of curtailment for an electrical grid.

2.1 Constrained Wind versus Curtailed Wind

The dispatch down of a wind turbine can be classified into two types: constrained wind and curtailed wind. Both imply that an excess of wind energy is generated and that a number of wind turbines are to be dispatched down. However, there is a fundamental difference in why this dispatch down occurs. It is this difference which makes it possible whether excess power can be utilized at off-site locations or not.

Constrained Wind

Constrained wind refers to the dispatch down of wind turbines due to local reasons. For example, when a wind park generates more power than transmission lines can handle. In this situation one must dispatch down a specific wind turbine present within the wind park. Therefore, constrained wind can be described as follows: *"Constrained wind is the dispatch-down for local reasons. Only a specific wind generator can alleviate the problem(17)"*. A visual representation of such a situation is displayed in Figure 2.1a. Since constrained wind is caused by the limited capacity of transmission lines the power can not reach thermal power plants even if it was generated. Therefore, constrained wind is not investigated any further within the scope of this thesis.

Curtailed Wind

In contrast to constrained wind, curtailed wind or curtailment, occurs when the amount of wind generated threatens the stability of the grid. Whenever a wind turbine must be dispatched down due to this reason but it is irrelevant where this wind turbine is located geographically, curtailment occurs. Such a situation is shown in Figure 2.1b. Any wind turbine can be dispatched to mitigate the problem of grid stability. Therefore, curtailment can be described as follows: *"Curtailment is the dispatch-down for system-wide reasons. Any wind generator can alleviate the problem(17)"*. This thesis continues with the concept of curtailment since it can be used in existing thermal power plants in contrast to constrained wind.

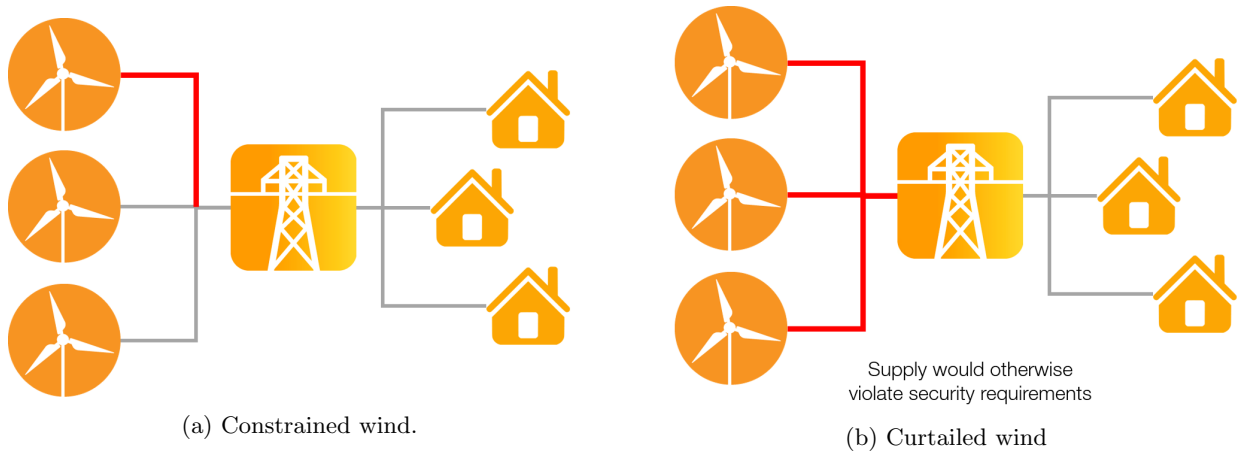


Figure 2.1: Schematic of constrained and curtailed wind.

2.2 Curtailment Causes

Major causes for curtailment often come from requirements imposed on the grid to maintain system security(18; 19). Two of these requirements are shortly discussed and elaborated upon(18; 20; 17; 21).

Synchronous Generators

The operating frequency of the grid depends on the power control. To keep the grid frequency at 50 Hz, the active power supply must equal the demand. Therefore, generation and demand must be kept in equilibrium. A graphical representation of this situation is provided in Figure 2.2. The demand loads pull an inflexible sheet down towards lower frequencies whereas the supply loads pull it up to maintain its frequency at the desired level. Since power consumption varies according to the time of day, season and weather conditions, the frequency has to constantly be controlled. Synchronous generators, such as are present in thermal generators, can more easily maintain a constant frequency due to their rotational inertia. Wind turbines often use non-synchronous generators, or induction generators, whose output frequency does not directly correspond to its RPM, making frequency control more difficult(22). They are used due to the advantage of being able to generate power at different rotor speeds. Introducing a large number of wind power into the generation mix therefore increases the complexity of frequency control. As a result, a certain percentage of the grid's generation has to be fulfilled by synchronous sources such as thermal generators and not all generated wind energy is accepted by the grid operators

Regulating and reserve requirements

Operating reserves are also related to the grid's frequency control. The output of IRES sources can not yet be predicted with a 100% accuracy. Therefore, thermal generators must be active to deliver the required power when needed to avoid temporary blackouts and to solve transmission constraints. These generators are referred to as regulating reserves(21). To maintain a stable and trustworthy grid there is a lower limit of generators that must be active. The amount of generators acting as reserves increases when the IRES penetration increases due to a larger share of intermittent power. By having this set of generators operative at all times there is less "room" for IRES sources. When more wind power is generated than the grid can accommodate, curtailment occurs.

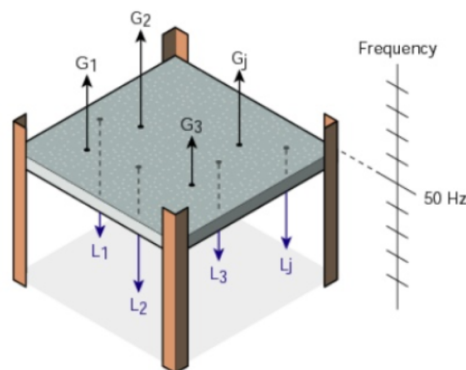


Figure 2.2: Schematic of frequency control. Modified from (20).

2.3 Conclusions and Observations

The dispatch down of wind turbines can be classified into two categories; constrained wind and curtailment. Constrained wind occurs due to local reasons and requires a specific wind turbine to be shut-down. On the contrary, curtailed wind is a system wide problem and any wind turbine, regardless of location, can be shut down to alleviate the problem. Due to the nature of constrained wind, curtailment is the main focus within this research project. Curtailment has, amongst others, two major causes. The first being the limited amount of allowed non-synchronous sources as a result of frequency control. To keep the grid frequency at 50 Hz power generators constantly adjust their. Due to the intermittent nature of wind and the adjustment time of thermal generators curtailment might occur as a result of frequency stabilization. As a result, only a limited amount of wind turbines are allowed to be active to be able to cope with its intermittent nature. Finally, regulating reserve plants are required since wind energy can not be predicted with a 100% accuracy. These plants are on standby to assure an equilibrium between power supply and demand and solve local transmission constraints.

Chapter 3

Curtailment Modelling

For the purpose of this research project it is essential to model curtailment to give an indication of its magnitude and occurrence pattern. Using the causes for curtailment as described in chapter 2, a model is developed for this purpose. The structure of this model and its results are presented in the following three sections.

3.1 Model Structure and Underlying Equations

Wind curtailment on an annual basis is modelled by using the national annual demand and wind production patterns. Figure 3.1 displays an illustrative period throughout the year 2015 to demonstrate how the occurrence pattern for curtailment can be estimated using these inputs. For this example both the 2015 demand and wind production patterns of the United Kingdom have been used since no such annual patterns with small enough time step were found for the Netherlands(23). These patterns are scaled to the national generation data for the Netherlands for the year 2015 to model curtailment for the Netherlands. Finally, the demand and wind power are scaled from a wind penetration of 5.84% (2015 rate) to 30% to improve clarity of the used simulation method for the reader(24). For these data sources, the maximum time step cannot exceed one hour to achieve a detailed model for curtailment(7). In addition, these inputs should span the same period and time-series(7). From the demand and wind production data the residual load can be computed. This represents the load which has to be supplied solely by thermal generators. The residual load can be computed as shown in Equation 3.1.1 and its occurrence is displayed in Figure 3.1b.

$$P_{residual} = P_{demand} - P_{wind\ production} \quad (3.1.1)$$

During periods of high wind production the residual load is low. Grid requirements as described in section 2.2 limit the minimum thermal generation and thereby reduced the room left for wind generation. When the residual load falls below the limits originating from requirements, wind generators are dispatched-down and wind is curtailed. For the purpose of curtailment modelling, two limits are defined. The first limit is referred to as the system non-synchronous penetration (SNSP) limit. The output frequency of a non-synchronous generator such as those used in wind turbines is harder to control than those from synchronous generators running at a constant RPM. The SNSP limit sets a threshold above which non-synchronous sources are not allowed into the grid due to system stability reasons(18; 19). This limit can be computed by means of Equation 3.1.2(18; 19). A limit of 100% means that the complete grid can be operational with solely non-synchronous sources. For the model used within this research no national imports or exports are considered.

$$SNSP = \frac{P_{wind\ production} + Imports}{P_{demand} + Exports} \quad (3.1.2)$$

Ireland currently uses a SNSP limit of approximately 50%(18; 19). This limit might decrease in the future due to a more stable and flexible grid architecture. It must be noted that this limit might be significantly lower due to the fact that Ireland is an island. The second limit is referred to as the regulating and reserve limit (RR)(18; 19). It states that a group of generators must be operative as reserves to adjust their power according to the occurred frequency change. Therefore, there is a minimum number of thermal power plants constantly active. For simplicity, this minimum power generation is taken to be constant throughout the year and is defined as a percentage of the maximum demand. Therefore it can mathematically be represented as shown in Equation 3.1.3. A limit of 100% means that the complete demand has to be delivered by thermal generators at all times.

$$RR = X \cdot P_{max\ demand} \quad (where\ 0 \leq X \leq 1) \quad (3.1.3)$$

These two limits can be compared to the residual load. If the residual load is lower than one of these limits, the difference between the residual load and the limit line is marked as curtailment as shown in Figure 3.1b. By doing so the pattern and magnitude of curtailment contributed to each limit can easily be computed. For the illustrative period this is shown in Figure 3.1c. A major advantage of this model is that the cause of curtailment can easily be associated with the limit it originates from. Using this model an indication can be provided why wind turbines are dispatched more often than solar panels. Wind generation does not change its output as drastically during the night as solar generation does. Solar generation often coincides with high demand levels and therefore results in higher residual loads.

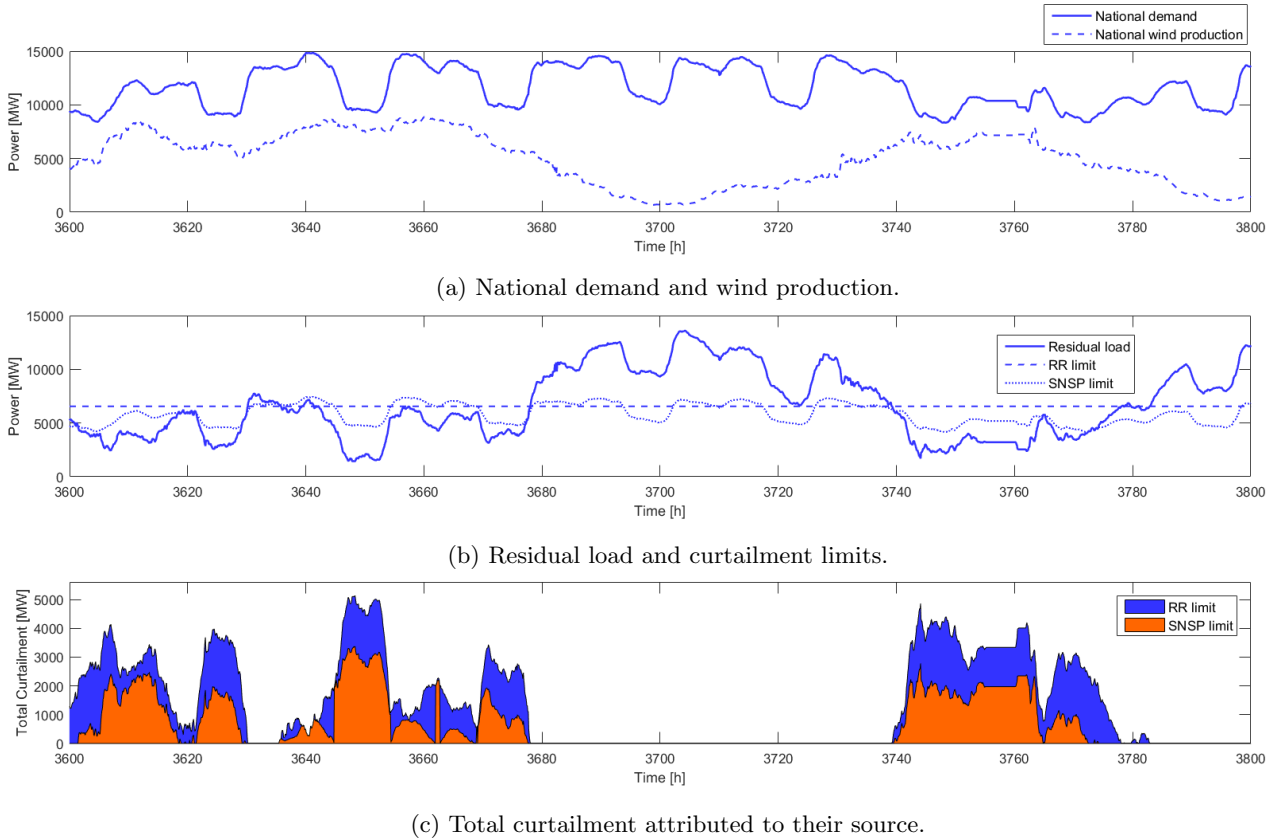


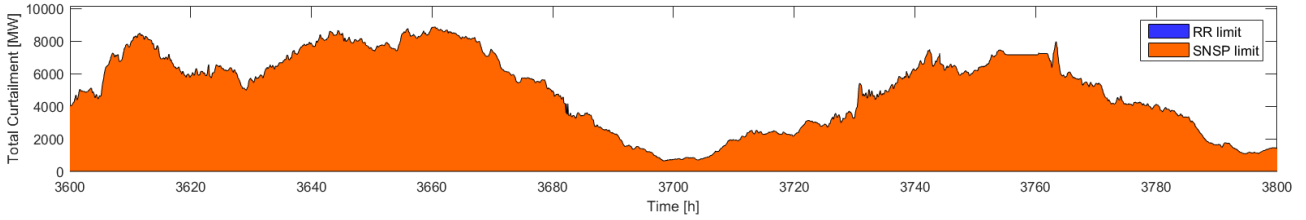
Figure 3.1: Curtailment model for the Netherlands at 30% wind penetration, 50% SNSP and 20% RR.

3.2 Verification

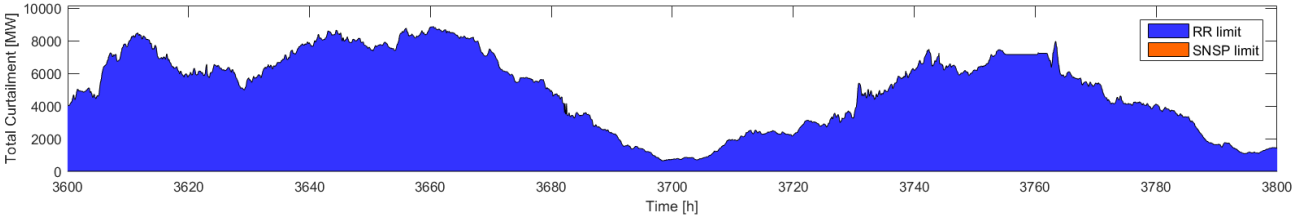
To verify the model three verification cases are evaluated. The first being for a SNSP and RR limit of 0%. For such low limits all the wind power generated directly translates into curtailment since no wind power is allowed into the grid. Using these settings, the curtailment pattern as displayed in Figure 3.2a is obtained. It is clearly visible that all curtailment originates from the SNSP limit for a 0% value. The same test can be performed for the SNSP and RR limits of 100%. All wind power is expected to be curtailed and originating from the RR limit as displayed in Figure 3.2b. Comparing these curtailment patterns to the initial wind production pattern in Figure 3.1a one can see that they are identical. In addition, curtailment should be zero when the SNSP and RR limits are 100% and 0% respectively. This is indeed the case as can be observed in Figure 3.3. In this figure all verification cases can be observed to be true for various SNSP and RR limits.

3.3 Results

Simulating annual curtailment patterns show that curtailment levels are the highest during low demand hours since this results in low residual loads. The curtailment pattern previously displayed was valid for one specific wind penetration, SNSP limit and RR limit. Therefore, to obtain knowledge on how curtailment changes according to a change in grid circumstance, several simulations are performed for different SNSP and RR limits at various wind penetrations. The results of these simulations are displayed in Figure 3.3. Curtailed wind became more prominent for lower SNSP limits and higher RR limits. When the SNSP limit reaches 0% a plateau is reached. For higher wind penetration percentages the RR limit starts contribute more to curtailed wind at lower levels. This trend can easily be identified when comparing Figure 3.3a to Figure 3.3d.

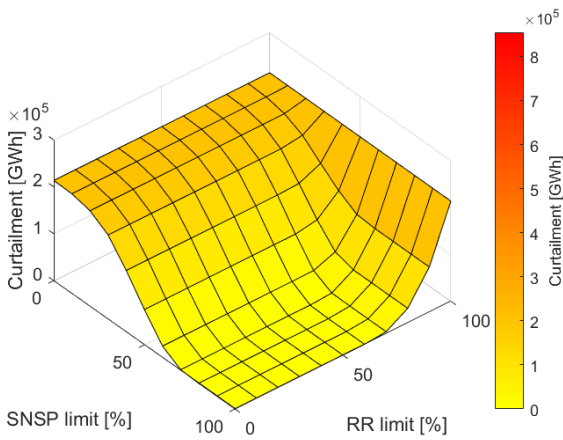


(a) Curtailment at 0% SNSP and 0% RR.

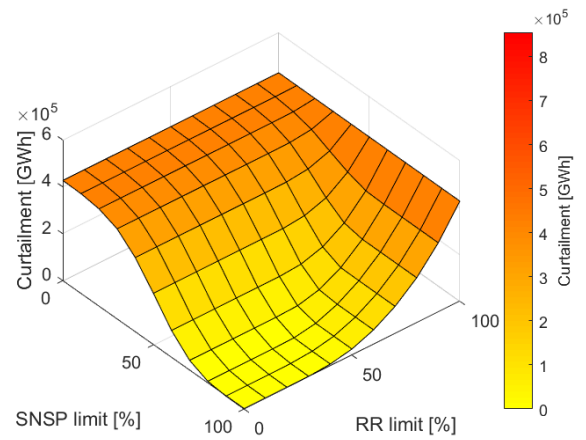


(b) Curtailment at 100% RR and 100% SNSP.

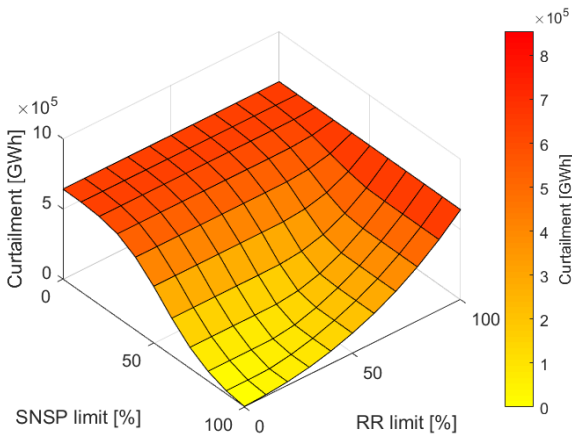
Figure 3.2: Verification cases.



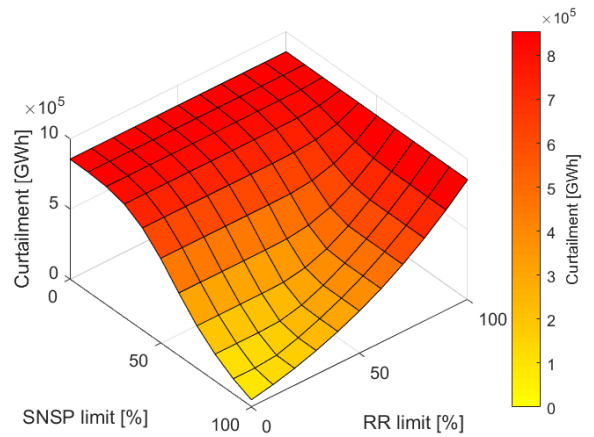
(a) 15% wind penetration



(b) 30% wind penetration



(c) 45% wind penetration



(d) 60% wind penetration

Figure 3.3: Influence of SNSP and RR limits on curtailment for various wind penetration levels.

3.4 Conclusions and Observations

The occurrence of wind curtailment is modelled using two grid requirements. The SNSP limit, which limits the number of non-synchronous generators in the grid to increase frequency control. The second limits is the RR limit. This limit indicates the minimum power supply which constantly has to be active. Using these requirements and the national demand and wind production, wind curtailment can be predicted at the time step of five minutes. This is done by comparisons the residual load to both limits to assess whether any requirements are violated. To verify the model three

extreme situations were simulated. The first being SNSP and RR limits both of 0%, the second being SNSP and RR limits both of 100% and the third a SNSP limit of 100% and RR limit of 0%. All cases demonstrated the expected results, namely a curtailment pattern which matches the national wind production or zero curtailment.

The model was used to simulate various annual curtailment patterns for the complete ranges of the SNSP and RR limits. This was done for several national wind penetration levels to identify the impact of a higher share of IRES on curtailment. As expected, higher SNSP limits and lower RR limits lead to lower curtailment quantities and less occurrences. An increase in the IRES generation mix share increases curtailment. In short, a verified model has been created which can model curtailment at a time step of five minutes for different grid characteristics.

Chapter 4

Combined-Cycle Power Plants

The goal of this chapter is to provide a better insight into CCPP architectures, their components, operating mechanisms and thermodynamic advantages. The first section deals with the operating principle and major components of a combined-cycle power plant. The second section elaborates upon its thermodynamic advantages compared to a single gas or steam turbine.

4.1 Power Plant Architecture

A CCPP architecture consists of four major components; gas turbine, heat recovery steam generator (HRSG), steam turbine and generator. The gas turbine operates according to the Brayton cycle whereas the steam turbine operates according to the Rankine cycle. The CCPP is based on the principle that when both cycles are combined in series, the total work extracted and thermal efficiency are greater than those of solely a Brayton or Rankine cycle. This is due to waste heat recovery of the Brayton cycle in the Rankine cycle. This statement is proven mathematically in section 4.2. A simplified plant architecture is displayed in Figure 4.1.

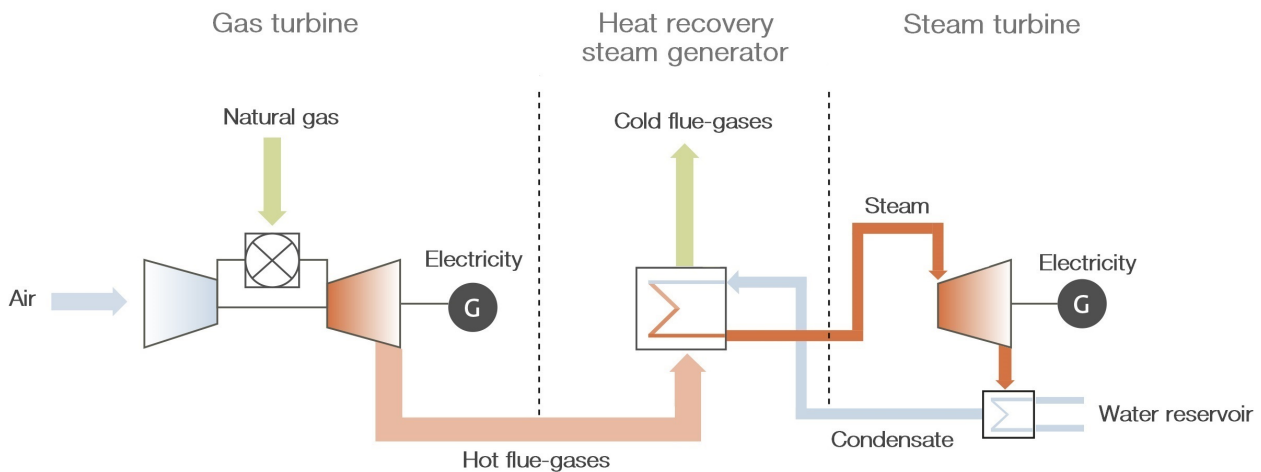


Figure 4.1: Multi-shaft combined-cycle power plant layout. Modified from (25).

Air is fed into the system and compressed by the compressor in the gas turbine. This air is then mixed with natural gas and combusted within the combustion chamber. This combusted air-fuel mixture, also known as flue-gas, is then expanded by a turbine to deliver work. This work is used to drive the compressor, and in some cases, auxiliary units. Excess work is used to drive a generator which generates electricity. Hot exhaust gases leaving the turbine run through the HRSG to evaporate water into superheated steam. This steam is expanded through turbines in the steam cycle to extract work. The steam turbine is connected to the generator to convert its work into electricity. Steam leaving the steam turbine is condensed under a constant pressure by the condenser to dissipate heat from the working fluid. This requires a source which temperature is below that of the exhaust steam, usually a river or sea.

A CCPP can have a single or multi-shaft configuration. When a single shaft configuration is used the gas turbine and steam turbine(s) are connected to one single shaft connected to a generator. This generator may be located

after the steam turbine or in-between the gas and steam turbines. For a configuration where it is located in-between the gas and steam turbines a clutch is often used during power plant start-up procedures. This allows for the gas turbine to be operative during start-up without driving the steam turbine generator. When the gas turbine shaft speed exceeds the required RPM and enough steam has been generated in the HRSG the clutch is engaged connecting steam turbines to the generator(26). For multi-shaft configurations the gas turbines and steam turbines often have their own corresponding generators making a clutch unnecessary.

4.1.1 Gas Turbine

The gas turbine stands at the core of the CCPP. It produces the majority of power and functions as the heat source for the Rankine cycle. Typical thermal efficiencies of a gas turbine range between 38-42% depending on their characteristics(27). Gas turbines used for power generation can be classified into two main categories(26):

Aero-derivative gas turbines

Aero-derivative gas turbines often use multiple shafts and are derived from the aerospace industry. The compressor and the turbine driving the compressor can rotate at various shaft speeds since a separate power turbine is often used. These type of turbines can start-up faster than their industrial counter-parts due to their low inertia(26). Aero-derivative gas turbines are often used for applications below 66 MWe and for CHP power plants due to their lower outlet temperature(26; 27).

Heavy-duty industrial gas turbines

Heavy-duty industrial gas turbines often use a single shaft configuration and can reach up to 340 MWe(26). They are purely designed for operation in static environments and to operate at a fixed shaft speed. Industrial gas turbines can have higher tolerance for low quality fuels at the cost of a slightly lower thermal efficiency than aero-derivative gas turbines, thereby making them more suitable for combined-cycle operation.

Both types operate according to the thermodynamic Brayton cycle. The temperature-entropy diagram explains the ideal Brayton cycle and is displayed in Figure 4.3. The cycle consists of four phases. The first phase is isentropic compression (1-2) where ambient air is compressed and thereby the temperature and pressure of the air is increased under isentropic conditions. The compressed air enters the combustion chamber where it is mixed with fuel under a constant pressure (2-3). The heated, pressurized mixture is expanded through a turbine delivering work under isentropic conditions (3-4). This work is partially used to drive the compressor. Finally, heat is rejected into the atmosphere to complete the cycle (4-1). In reality, the processes to which the air and flue-gases are subjected to are not ideal as depicted here since both compression and expansion are not isentropic. A pressure drop occurs during combustion and both the compressor and turbine experience mechanical losses.

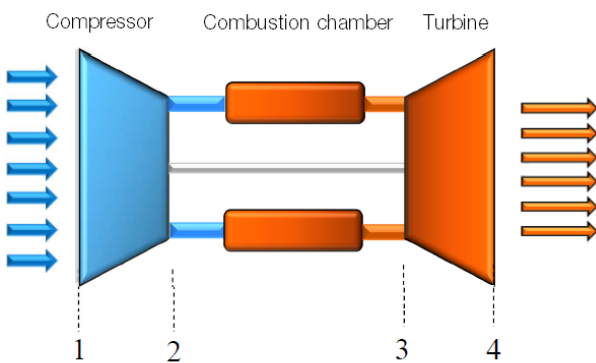


Figure 4.2: Schematic of gas turbine gas path. Modified from (26).

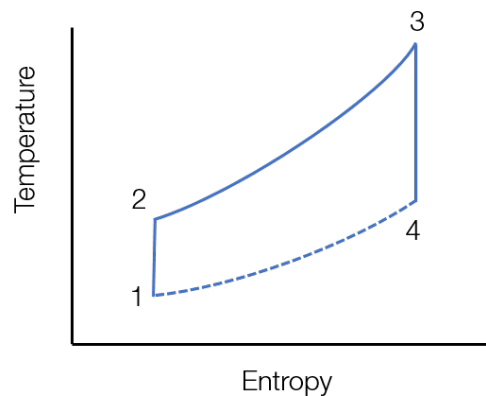


Figure 4.3: T-s diagram for the ideal Brayton cycle.

4.1.2 Heat Recovery Steam Generator

After expansion in the gas turbine the exhaust gases enter the HRSG. The goal of the HRSG is to use the thermal energy present in the flue-gas to produce superheated steam. The HRSG acts as a link between the gas turbine and steam turbine. A HRSG can be supplementary-fired for several reasons: to improve the controllability of thermal conditions, compensate for changing ambient conditions, allow for the gas turbine to run at lower loads or to burn

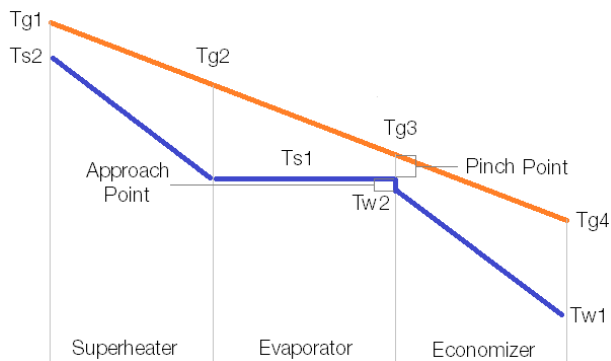


Figure 4.4: Temperature profile through the superheater, evaporator and economizer for a single-stage HRSG. The orange line represents the hot flue-gases and the blue line the feedwater/steam.

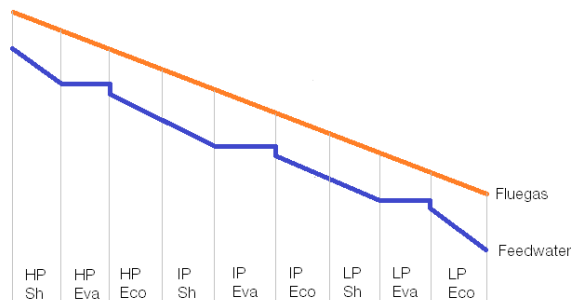


Figure 4.5: Temperature profile through the superheater, evaporator and economizer for a three-stage pressure HRSG. The orange line represents the hot flue-gases and the blue line the feedwater/steam.

fuels not suitable for gas turbines(28). In a single pressure HRSG heat is recovered by means of three steps. A visual representation of these steps is shown in Figure 4.4.

The first step occurs in the economiser, low value heat from the flue-gases is used to heat pressurized feedwater. To avoid evaporation within the economizer the feedwater exit temperature is lower than the saturation temperature of water. The economizer tubes are not designed for two-phase flows and can cause operational problems such as erosion, deposition of salts(29). This water then enters the evaporator and is heated until it reaches its saturation temperature. The feedwater enters the evaporator in liquid phase and exists as steam. High value flue-gases heat the steam to a temperature above its saturation temperature, the steam is then referred to as being superheated. Two important design parameters for the economiser and evaporator are the pinch and approach points. The pinch point is the difference between the flue-gas temperature exiting the evaporator and the saturation temperature. Pinch points always have to have a positive value to ensure heat transfer between the two media. A reduction of the pinch point leads to smaller heat losses since more energy can be transferred from the flue-gas to the water. However, reducing the pinch point is costly since it requires a relatively large HRSG surface. Pinch point magnitudes vary between 5°C to 15°C(26; 30). The approach point represents the difference between the economizer exit temperature and the saturation temperature. It often ranges between 2°C and 12°C and should be kept as small as possible to maximize steam generation(26; 30). The pinch and approach points are often used during the design phase to determine the sizes of the superheater, evaporator and economizer(26; 30).

Multiple Pressure Stages

In Figure 4.4, the difference between the flue-gas and feedwater temperature lines represent the total heat losses. The larger this area, the less heat recovered from the flue-gas(26; 30). For a single-stage HRSG which produces steam at a pressure of 100 bar the saturation temperature equals 311.8°C (31). If the flue-gas leaving the gas turbine is around 600°C the flue-gas temperature leaving the stack will be around 300°C since most heat is absorbed during evaporation. This means that almost half of the total heat present in the HRSG is lost and not used for steam generation. To reduce these losses, multiple pressure stages can be introduced (see Figure 4.5). For a three-stage HRSG three superheaters, evaporators and economizers are present, all operating at different pressures. By introducing different pressure levels, steam is also generated at different saturation temperatures. The selected pressures for each section have to be distinctive, the lowest pressure should be chosen in such a way that steam can be generated with the "cold" flue-gases. The highest pressure should be high enough to maximize turbine power coming from the high pressure turbine. As a result, a multi-stage HRSG generates a higher steam mass flow and therefore has a higher efficiency and steam turbine output when compared to a single-stage HRSG(26; 30).

HRSG Variants

HRSG's for combined-cycle applications can be categorised in two main categories: vertical and horizontal HRSG's. Within the HRSG, one can also make a distinction between steam drum and once-through HRSG configurations. These categories and configurations are shortly elaborated upon in the three upcoming paragraphs.

Vertical HRSG

In vertical HRSG's the heat transfer tubes are located in a horizontal orientation and the flue-gas travels in the vertical direction. Circulation pumps are used to circulate the feedwater through the evaporator tubes(26). Therefore, these

types of HRSG's are also referred to as forced-circulation HRSG's(29). The use of these pumps leads to an increase in operational costs. In addition, the steam bubbles formed during the evaporation process tend to drift towards the top of the tubes, whereas the water occupies the lower parts of the tubes.

Horizontal HRSG

Horizontal HRSG's, also known as natural-circulation HRSG's, make use of a configuration opposite to that of its vertical counterpart. In this configuration, the heat transfer tubes are located in a vertical orientation and the flue-gas travels horizontally. This allows for a natural circulation through the evaporator and therefore no pumps are needed. This circulation occurs due to gravity and the density difference which occurs when a medium is heated or cooled. A disadvantage of this configuration is its relatively large geographic footprint in comparison to its vertical counterpart(26).

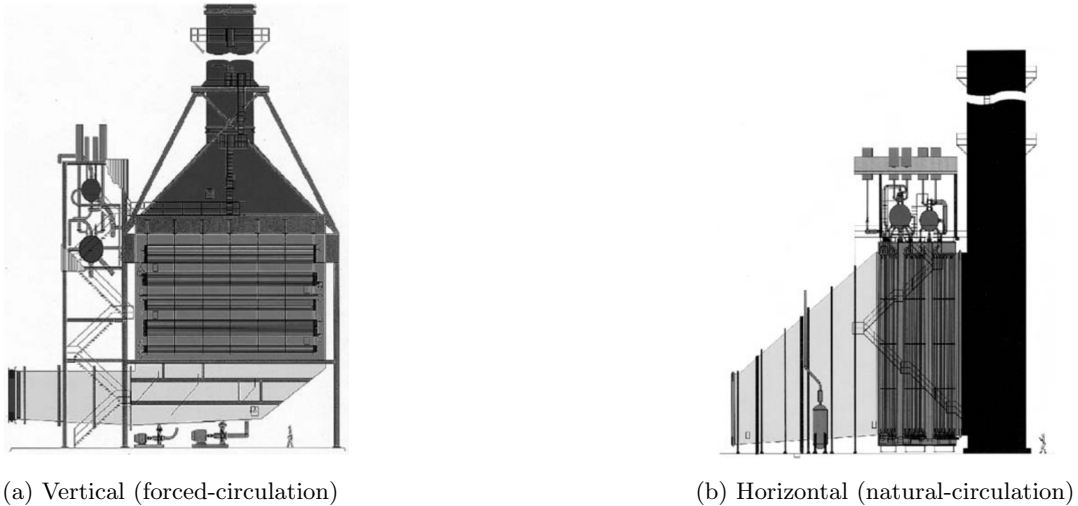


Figure 4.6: Types of heat recovery steam generators: vertical and horizontal generators(26).

Once-trough boiler

A steam drum can be used to separate the steam from the water after it has passed through the evaporator. Due to the differences in density between the saturated steam and the heated water these two are separated from one another. Instead of using a drum, one can also use an once-trough boiler. Here the economizer, evaporator and superheater are a single tube, eliminating the steam drum(26). Feedwater enters the tube before the economizer and eventually comes out as superheated steam.

4.1.3 Steam Turbine

The steam turbine is located directly after the HRSG and expands high enthalpy steam through a single or series of turbines thereby performing work on a connected shaft. Pressurized superheated steam enters the turbine stages and causes the blades to rotate, generating work. At the final turbine, saturated vapour, or a mixture of liquid and vapour, leaves the turbine and enters the condenser. This together with the process of evaporation in the HRSG is referred to as the Rankine cycle. Its thermodynamic cycle is visualized in Figure 4.7a. Note that this figure corresponds to a Mollier diagram for water. At first heat is added to the water in the economizer of the HRSG (1-2). In the evaporator a mixture of water vapour and liquid water arises (2-3). At point three the steam quality is a 100% meaning that the mixture solely consists of steam. This steam is then superheated in the superheater (3-4) to further increase the steam temperature. Finally, the superheated steam is expanded through a turbine and work is generated (4-5). Heat is rejected by means of a condenser which transforms any steam back into liquid water (5-1). Figure 4.7b displays the T-s diagram for an ideal Rankine cycle where the steam is reheated after passing through the turbine (5-6). This leads to more energy being extracted from the generated steam.

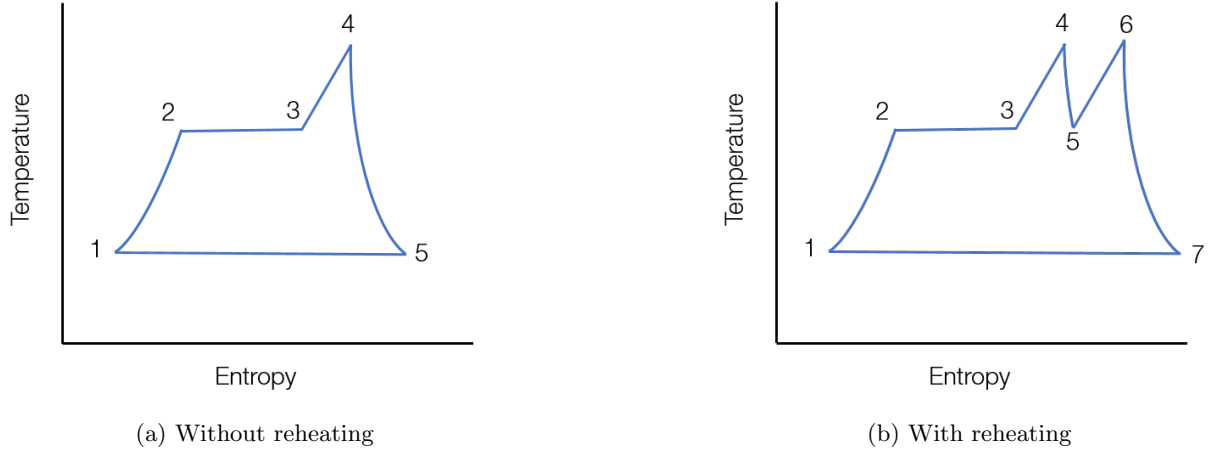


Figure 4.7: T-s diagram for the ideal Rankine cycle without and with steam reheating.

4.2 Thermodynamic Principles of the Combined-Cycle Power Plant

The maximum thermal efficiency of a thermodynamic cycle is limited by the Carnot efficiency. It assumes that isothermal compression, isentropic compression, isothermal expansion and isentropic expansion take place. Since these processes do not occur in reality, the real thermal efficiency of a system can be described as a percentage of the Carnot efficiency. The Carnot efficiency depends on the lowest and highest temperature within the thermodynamic cycle and can be expressed as shown in Equation 4.2.1.

$$\eta_{Carnot} = 1 - \frac{T_{cold}}{T_{hot}} \quad (4.2.1)$$

One can observe from this equation that the Carnot efficiency improves when the maximum cycle temperature increases or the minimum temperature decreases. Combined-cycle power plants are based on this principle and combine two thermodynamic cycles: one with a high temperature, being the gas turbine, and one with a low temperature, being the condenser(26). Although combined-cycle plants only achieve around 75% of their Carnot efficiency whereas a simple steam turbine can achieve around 80%, the real thermal efficiency of a combined-cycle is still significantly higher(26). This means that the Carnot efficiency is higher for a CCPP than for solely a simply stream cycle. The total thermal efficiency for a CCPP can be described as the ratio between the useful work delivered by the system and the work delivered to the system. This leads to the following definition for the total thermal efficiency of a CCPP as shown in Equation 4.2.2(26).

$$\eta_{th,CCPP} = \frac{P_{Brayton} + P_{Rankine}}{Q_{Brayton} + Q_{Rankine}} \quad (4.2.2)$$

The thermal efficiencies for the Brayton cycle and Rankine cycle in a combined-cycle configuration are described in Equation 4.2.3 and Equation 4.2.4 respectively (26). Where $Q_{exh,Brayton}$ represents the rate of heat coming from the Brayton cycle after power generation and $Q_{Rankine}$ represents any heat added by means of supplementary firing in the HRSG.

$$\eta_{th,Brayton} = \frac{P_{Brayton}}{Q_{Brayton}} \quad (4.2.3)$$

$$\eta_{th,Rankine} = \frac{P_{Rankine}}{Q_{exh,Brayton} + Q_{Rankine}} \quad (4.2.4)$$

$$Q_{exh,Brayton} = Q_{Brayton}(1 - \eta_{th,Brayton}) \quad (4.2.5)$$

Combining equations 4.2.4 and 4.2.5 leads to the following equation for the Rankine cycle efficiency as shown in Equation 4.2.6. If fuel is only added to the system in the combustion chamber then $Q_{Rankine}$ equals zero (no supplementary firing in the HRSG). By using the previous equations, the total combined-cycle plant efficiency can be written as shown in Equation 4.2.7 and simplified to Equation 4.2.8.

$$\eta_{th,Rankine} = \frac{P_{Rankine}}{Q_{Brayton}(1 - \eta_{Brayton}) + Q_{Rankine}} \quad (4.2.6)$$

$$\eta_{th,CCPP} = \frac{\eta_{th,Brayton}Q_{Brayton} + \eta_{th,Rankine}Q_{Brayton}(1 - \eta_{th,Brayton})}{Q_{Brayton}} \quad (4.2.7)$$

$$\eta_{th,CCPP} = \eta_{th,Brayton} + \eta_{th,Rankine}(1 - \eta_{th,Brayton}) \quad (4.2.8)$$

Current state of the art combined-cycle plant systems can achieve a thermal efficiency of 61.5% whereas solely its gas turbine efficiency is 40%(32; 33). Such a value is currently not achievable by either a gas or steam turbine as can be proved using Equation 4.2.1. Just as for a simple cycle gas turbine power plant, the gas turbine inlet temperature (TIT) is a dominant factor when it comes to thermal efficiency. Compressor pressure ratio (PR) still plays an important role, but no longer has a simple positive effect since an optimum PR is present for CCPPs. This comparison is visualized in Figure 4.8. The explanation for this behaviour lies in the fact that flue-gases are used for steam generation in the Rankine cycle. Therefore, the higher the temperature of the flue-gases the more power can be generated by the steam turbine. Power generation is no longer reliant on one turbine for electricity generation.

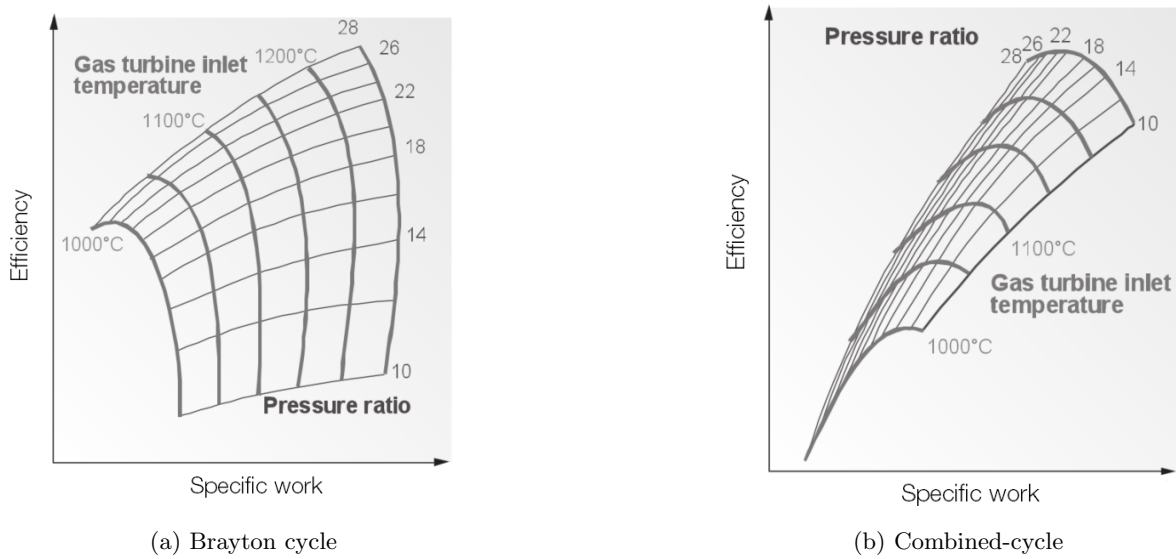


Figure 4.8: The efficiency of a simple Brayton cycle and a combined-cycle plant as a function of the gas turbine inlet temperature and pressure ratio. Modified from (26).

4.3 Conclusions and Observations

The working principle of the CCPP is based on using hot exhaust gases from the gas turbine to generate steam in the HRSG. This steam is expanded through a turbine to generate electricity. Gas turbines were distinguished in two categories; aero-derivative and heavy-duty industrial gas turbines. Both categories were shortly elaborated upon and discussed. Within a CCPP the exhaust gasses from the gas turbine pass through a HRSG to transfer flue-gases thermal energy to water to create superheated steam. Several types of HRSG's and their components have been elaborated upon. The advantages of using a multiple pressure stage HRSG to reduce heat losses has been explained. After superheated steam is created in the HRSG, it passes through the steam turbine(s). For multiple pressure stages HRSG's multiple turbines can be used for each stage. The effect of steam reheating on power output was demonstrated using the T-s diagram for the Rankine cycle.

The thermal efficiency for a CCPP power plant has been mathematically expressed in terms of its gas and steam turbine thermal efficiencies. It was shown that CCPPs operate more efficiently than solely a Brayton or Rankine cycle when used for electricity generation. Current state of the art combined-cycles can achieve a thermal efficiency of 61.5%. TIT still plays an important role in CCPPs as it does in a single Brayton cycle. However, compared to simple-cycles, the PR now has an optimum value rather than a simple positive effect.

Chapter 5

Combined-cycle Power Plant Modelling

This chapter consists of four sections. The first section deals with the selection of an appropriate power plant to model. This plant is used as a reference plant to assess the effect of curtailment utilization. Its components are described together with its annual operating pattern. In the second section the CCPP's gas turbine is modelled using three different simulation programs: THERMOFLEX, gas turbine simulation program (GSP) and Cycle-Tempo. The methodology behind these programmes is explained and its results presented. The third section deals with the complete combined-cycle simulation using both THERMOFLEX and Cycle-Tempo. Within this section the results are presented and their validity quantified and discussed. In the final section, the results are used to quantify the annual performance of the simulated power plant in terms of power generation, fuel consumption and carbon-dioxide emissions.

5.1 Power Plant Selection

Before the combined-cycle power plant is selected various requirements are identified. These assure that the selected plant serves the final goal and that the research project results are realistic and applicable to real-life cases. The first of these requirements is that the plant is solely to be used for electricity generation. This excludes combined heat and power (CHP) plants as suitable candidates. To give a good indication when the project outcome is applicable to other plants, the power plant has to be representable for the currently operative CCPP within the Dutch grid. It has to represent a state of the art combined-cycle with a typical maximum electrical power output. In addition, the power plant should not have long periods of low or zero activity resulting from imposed policies throughout the observed time-frame. Finally, to successfully model the chosen plant, one requires its operating pattern for a specific year and general component data to be available. In short, the following five requirements are to be met:

- Solely a generator of electricity
- Represents a state of the art combined-cycle power plant
- Typical maximum electrical power output
- No major policies imposed during the simulation time-frame
- Availability of operating pattern and component data

The Hemweg 9 power plant in Amsterdam fulfils these criteria. It became operative in 2012 and has been in operation ever since(34; 35). It currently acts solely as an electricity producer although it can be run as an CHP in the future. It has a maximum power output of 435 MWe which is representative for CCPPs in the Netherlands. During the writing of this thesis, no known major policies were in effect restricting the operation of the Hemweg 9, making its operating pattern a good benchmark. Its corresponding operating pattern for the year 2015 is visible in Figure 5.1. A larger version and its occurrence distribution can be found in Appendix A, Figure A.1 and Figure A.2 respectively.

5.1.1 Technical Data

Because the Hemweg 9 power plant fulfils the previously mentioned criteria the modelled power plant is based on the Hemweg 9. It consists out of a single shaft configuration and uses a three pressure stage HRSG. The gas turbine, steam turbine and generator are all supplied by Siemens(35). A single SGT5-4000F gas turbine is used with a maximum power output of 292 MWe and a gross efficiency of 39.8% (37). Siemens has supplied their SST-5000 steam turbine whose output ranges between 120-500 MWe depending on the gas turbine and combined-cycle configuration(38). The

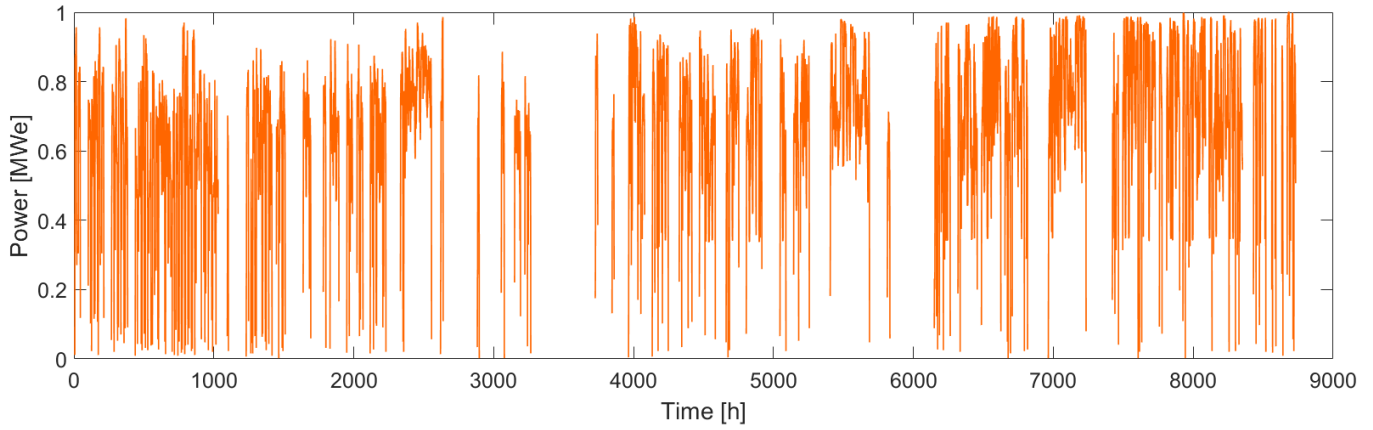


Figure 5.1: Normalized operating pattern for the Hemweg 9 for 2015(36).

Table 5.1: Reference plant gas turbine, steam turbine, generator and fuel specifications (37; 38; 39; 41; 42)

SGT5-4000F			SST-5000		
Parameter	Value	Unit	Parameter	Value	Unit
Gross output	292	[MW]	Gross output	120-500	[MW]
Gross efficiency	39.8	[%]	Main steam temperature	up to:	[°C]
Net heat rate	9,038	[kJ/kWh]	Main steam pressure	up to: 190	[bar]
Exhaust temperature	577	[°C]	Reheat steam temperature	up to:600	[°C]
Air mass flow	692	[kg/s]			
Generator type	Air cooled	[-]			

SGen5-2000h			Chemical formula		Mole percentage	
Parameter	Value	Unit				
Frequency	50	[Hz]	CH ₄			81.29
Gross efficiency	99	[%]	N ₂			14.32
Power factor	0.8	[-]	C ₂ H ₆			2.87
Apparent power	350-600	[MVA]	CO ₂			0.89
Terminal voltage	16.5-22	[kV]	C ₃ H ₈			0.38
Excitation	Static	[-]	C ₄ H ₁₀			0.15
			C ₆ H ₁₄			0.05
			C ₅ H ₁₂			0.04
			O ₂			0.01

generator is a SGen5-2000h hydrogen cooled generator with a conversion efficiency of 99%(39). More detailed data on the gas turbine, steam turbine and generator is provided in Table 5.1. The inlet pressures of all three steam turbines have been taken from a reference plant with the same configuration but a slightly lower maximum power(40). These are displayed in Appendix A, Table A.3. Slochteren natural gas is selected as fuel due to its commonality in the Netherlands. Several power plants operate on gas with a higher methane percentage and therefore this composition might differ per plant. The exact chemical composition of Slochteren gas can be found in Table 5.1. Using this data a power plant based on that of the Hemweg 9 with a gross design power output of 427 MWe can be modelled. It uses the Siemens SGT-4000F gas turbine, SST-5000 steam turbine and SGen5-2000h generator. The operating pattern for the Hemweg 9 during the year 2015 as shown in Figure 5.1 is scaled to 427 MWe and used as the annual operating pattern for the respective plant.

5.2 Gas Turbine Modelling

Before successfully modelling complete CCGP performance, a gas turbine model is first created. The rationale behind this procedure is that the gas turbine runs at off-design conditions during CCGP operation and must therefore be modelled separately. For the steady-state analysis of the Siemens SGT5-4000F at design and off-design conditions three software tools are used: THERMOFLEX, GSP and Cycle-Tempo(43; 44; 45). For each of these software, their working principle is shortly elaborated upon and summarized in Appendix A, Table A.1. The respective gas turbine model architectures are displayed and discussed in the second part of this section. Finally, the results of each model are presented, compared and discussed.

5.2.1 THERMOFLEX

THERMOFLEX is developed in 1995 and is part of the company Thermoflow. It can be used for both design and off-design simulations of power systems(44). It uses a graphical interface which allows the user to link components to each other. THERMOFLEX uses a large database of existing gas turbine models making gas turbine simulations require very little effort. Once the desired model has been chosen its main architecture and components performance parameters are loaded. In case of the SGT5-4000F, this includes parameters such as pressure ratio, maximum turbine inlet temperature and the inlet guide vane (IGV) control scheme. THERMOFLEX creates a simulation by means of three steps: the creation of the desired architecture, the addition of input parameters and the stage of finding a converged solution for the model's output parameters. During the first step only sinks and sources are to be added manually at the correct locations. These are required at every location where a medium enters or leaves the system. The simulation of the Siemens SGT5-4000F resulted in the model as displayed in Figure 5.2. Since the turbine is loaded from a database one can continue to step two after the addition of sinks and sources. If the modelled gas turbine deviates from the standard model, corrections can be implemented during this step. Although this is a very convenient and fast process, one can only change a limited amount of internal parameters within the system without using GTPRO. Therefore a less detailed analysis is possible and no modifications can be made throughout the gas path with solely a license for THERMOFLEX. Finally, the architecture and input parameters are used to compute the gas turbine performance. An overview of all relevant simulation parameters is available in Appendix A, Table A.2.

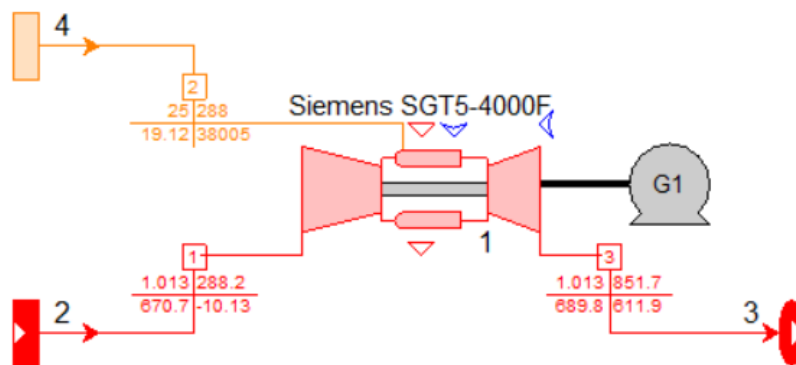


Figure 5.2: SGT5-4000F model in THERMOFLEX.

5.2.2 GSP

GSP is developed at Delft University of Technology in 1986 and is currently improved by Nederlands Lucht- en Ruimtevaartcentrum (NLR)(45). It is based on object-oriented achitecture creation through a drag and drop interface. The gas turbine is simulated by stacking components with relation to each other. Components exist for most prominent parts such as inlets, compressors, combustion chambers and turbines. The exit conditions of a component then forms the inlet conditions for the next. Non-dimensional modelling of processes is used in each component meaning that gas properties are averaged over a cross-section at both the inlet and exit(46). Internal component processes are dependent on a range of parameters and are defined by performance maps or thermodynamic relations(46). Two main simulation types are used within the GSP environment: design and off-design simulations. The design simulation fixes the gas turbine configuration and sizes all components according the gas turbine design point. At this stage, components performance maps are not yet used but are scaled. After the design point simulation has been performed one can proceed to the steady-state or transient off-design simulations. The sized gas turbine components, performance maps and configuration from the design point are then used to simulate off-design performance. The modelled gas turbine architecture is shown in Figure 5.3. To control the turbine exhaust temperature such as is done for industrial gas turbines, an equation component is implemented. To simulate the inlet guide vanes (IGV) the default compressor apparatus is adjusted to facilitate IGV's. For GSP to compute the state of the IGV during off-design conditions it must be a free state. This is achieved by implementing an IGV controller with free state characteristics. Another required free state is the fuel mass flow. Its corresponding controller is therefore also required to be set as a free state. Finally, a shaft power controller is required to run off-design calculations at a user-specified gross power output. This controller is then combined with a loop case controller to automatically perform simulation series. An overview of all relevant simulation parameters is available in Appendix A, Table A.2.

5.2.3 Cycle-Tempo

Cycle-Tempo has been developed by Delft University of Technology in collaboration with the non-profit organisation Nederlandse Organisatie voor toegepast-natuurwetenschappelijk onderzoek. It is currently supported and improved

6. Check whether all pipes meet the break-off criterion for fluid compositions and mass flows
7. Recompute all fluid compositions based on the mass flows
8. Compute final temperatures, pressures and enthalpies

The simulation of a gas turbine by means of Cycle-Tempo is very similar to that of GSP. A visual representation of the SGT5-4000F model within the Cycle-Tempo environment is shown in Figure 5.5. In contrast to GSP no controllers can be implemented within its environment leading to several changes to input parameters depending on the simulation case. Similar to THERMOFLEX, sources and sink are used to represent fluid steams. Due to the required input parameters, the exhaust temperature and mass flow of the turbine are easily fixed during both design and off-design simulations. Therefore the simulation of the IGV's is rather simple. However, when the IGV's have reached their maximum rotational angle, the model inputs have to be adjusted to accurately represent the new situation. An overview of all relevant simulation parameters is available in Appendix A, Table A.2.

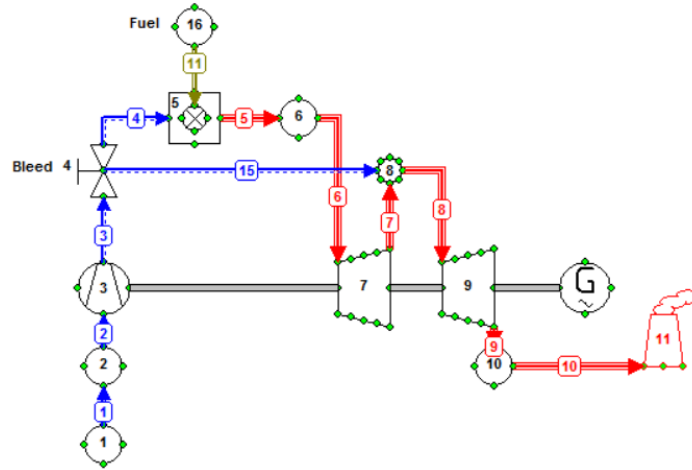


Figure 5.5: SGT5-4000F model in Cycle-Tempo.

5.2.4 Results

Before the results are presented, the simulation process is addressed shortly. This is of importance since not every model requires the same user inputs. THERMOFLEX's model is for a large portion a 'black box'. It is therefore that this simulation was performed first and its mass flows and gross power output at design point were used for the GSP simulation as inputs. This simulation was followed by that of GSP since it uses performance maps and Cycle-Tempo does not. The isentropic efficiency for the compressor calculated by GSP are then used in Cycle-Tempo depending on gas turbine output power. This approach was selected to be able to compare the results for similar configurations.

Design Point Performance

The results for the gas turbine design point for each simulation software is presented in Table 5.2. It can be concluded that all three simulations yield similar results with a maximum deviation of 2.005%.

Table 5.2: Design point simulation results for THERMOFLEX, GSP and Cycle-Tempo at ISO conditions.

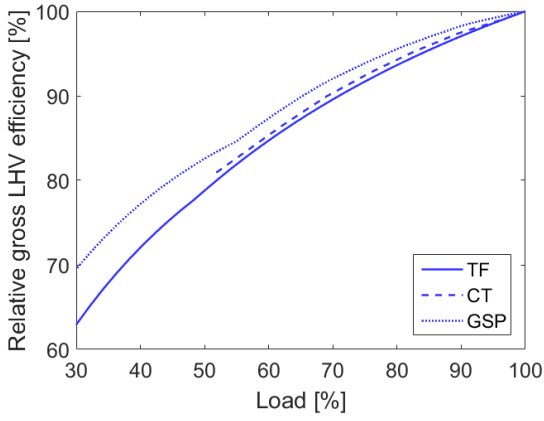
Parameter	THERMOFLEX	GSP	Cycle-Tempo	Maximum difference	Unit
Gross power	289.97	289.88	289.97	0.031%	[MW]
Gross efficiency	39.88	39.90	39.10	2.005%	[%]
Inlet mass flow	670.70	670.70	670.68	0.003%	[kg/s]
Fuel mass flow	19.12	19.12	19.12	0.00%	[kg/s]
Exhaust temperature	578.51	578.10	578.55	0.078%	[°C]
Exhaust mass flow	689.80	689.82	689.20	0.090%	[kg/s]

Off-design Performance

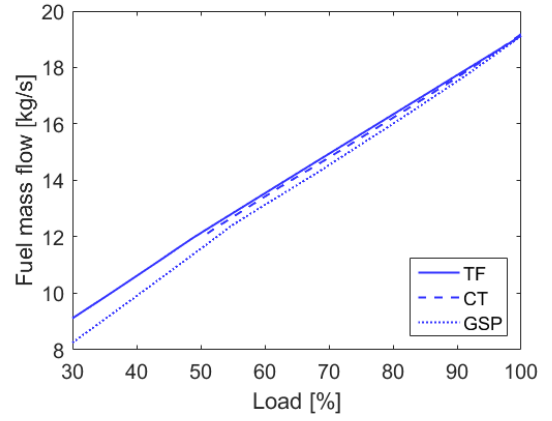
To simulate the off-design performance using Cycle-Tempo two different models were developed. The first makes use of Cycle-Tempo's standard method, namely by using a constant compressor isentropic efficiency. The second uses a generic compressor map from GSP to correct the compressor isentropic efficiency. This correction has been

performed by investigating which compressor efficiency GSP calculates at a specific load. This value is then used in all Cycle-Tempo simulations.

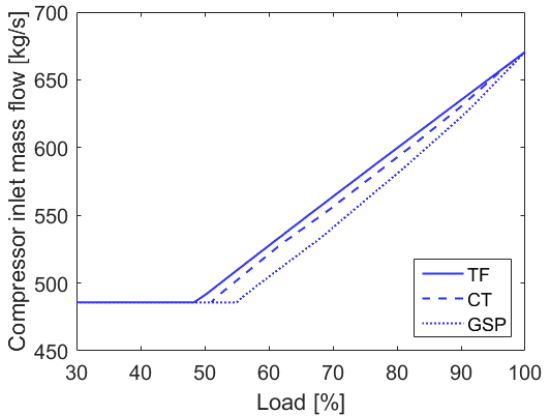
The simulation results are displayed in Figure 5.6. Within these figures the corrected Cycle-Tempo model is used. The relative gross LHV efficiency is displayed in Figure 5.6a. THERMOFLEX estimates lower efficiencies than Cycle-Tempo and GSP, resulting in higher mass flows at part load even though it simulates higher compressor isentropic efficiencies (Figure 5.6g). When observing gross LHV efficiencies a difference is present between GSP and Cycle-Tempo. This resulted from the fact that Cycle-Tempo uses a constant turbine isentropic efficiency whereas GSP does not as shown in Figure 5.6h. In addition, the exact turbine bleed cooling characteristics used by THERMOFLEX are unknown. This directly influences the percentage of the bleed that contributes for the expansion power of the turbine. Furthermore it was found that all three software computed different LHVs for the exact same fuel composition, leading to different fuel mass flows and efficiencies. Finally, the final results were limited by the maximum iteration accuracy of each software. Although this is not expected to have a significant influence on the final results.



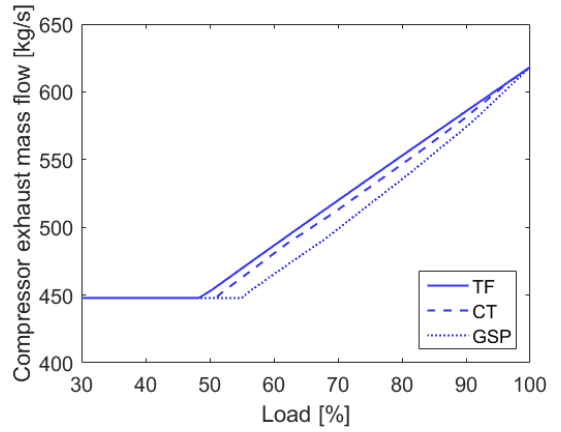
(a) Gross efficiency



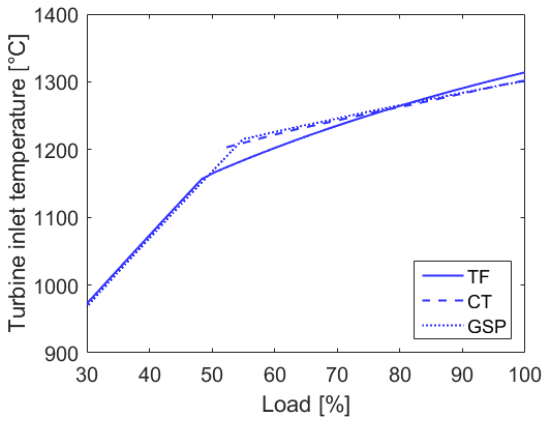
(b) Fuel mass flow



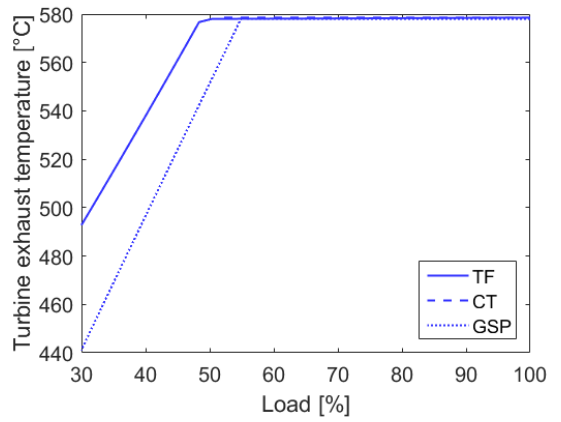
(c) Compressor inlet mass flow



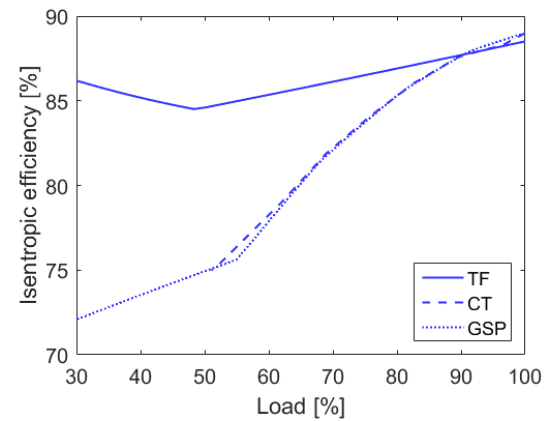
(d) Compressor exhaust mass flow



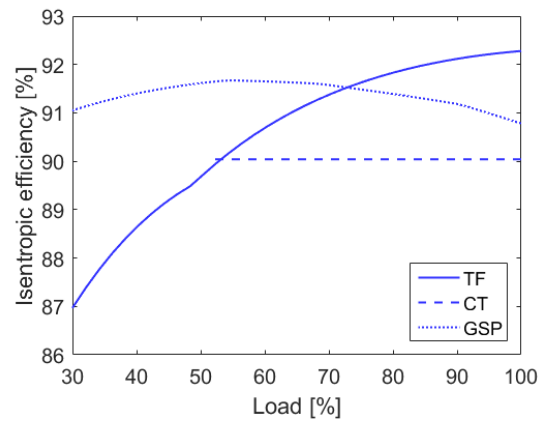
(e) Turbine inlet temperature



(f) Turbine exhaust temperature



(g) Compressor isentropic efficiency



(h) Turbine isentropic efficiency

Figure 5.6: Siemens SGT5-4000F off-design simulation results for THERMOFLEX (TF), GSP and Cycle-Tempo (CT) at ISO conditions.

5.3 Combined-cycle Modelling

The simulation models for the SGT5-4000F gas turbine can be extended to combined-cycle models. Since GSP cannot easily model the HRSG and steam turbine, only THERMOFLEX and Cycle-Tempo are used for this purpose. Once again, GSP has been used to correct the compressor isentropic efficiency in Cycle-Tempo. The resulting models and their corresponding results are presented in the next paragraphs.

5.3.1 THERMOFLEX

Modelling a CCPP in THERMOFLEX is rather easy since it automatically accounts for the gas turbines off-design performance at plant full-load due to the HRSG backpressure. Gas turbine flue-gases are divided into two streams of which one enters the high pressure (HP) superheater where the steam is superheated. The other stream passes through the reheater. After partial expansion through the HP turbine the steam is reheated before entering the medium pressure (MP) turbine. After the steam is expanded through the MP turbine it is mixed with steam coming from the LP superheater before it enters the low pressure (LP) turbine. The LP turbine can provide steam to the deaerator in off-design conditions when the deaerator evaporator can not provide enough steam itself. Exhaust steam from the LP is condensed by means of a cold water reservoir to complete the Rankine cycle. Using the data specified in Table 5.1 the gas turbine, steam turbine and generator are modelled as accurately as possible. Economisers, evaporators, superheaters and reheaters are modelled as heat exchangers. The exact model specifications can be found in Appendix A, Table A.3. The THERMOFLEX model architecture is presented in Figure 5.7 (a larger version is available in Appendix A, Figure A.3). Red streams represent hot flue-gases and blue streams represent water or steam.

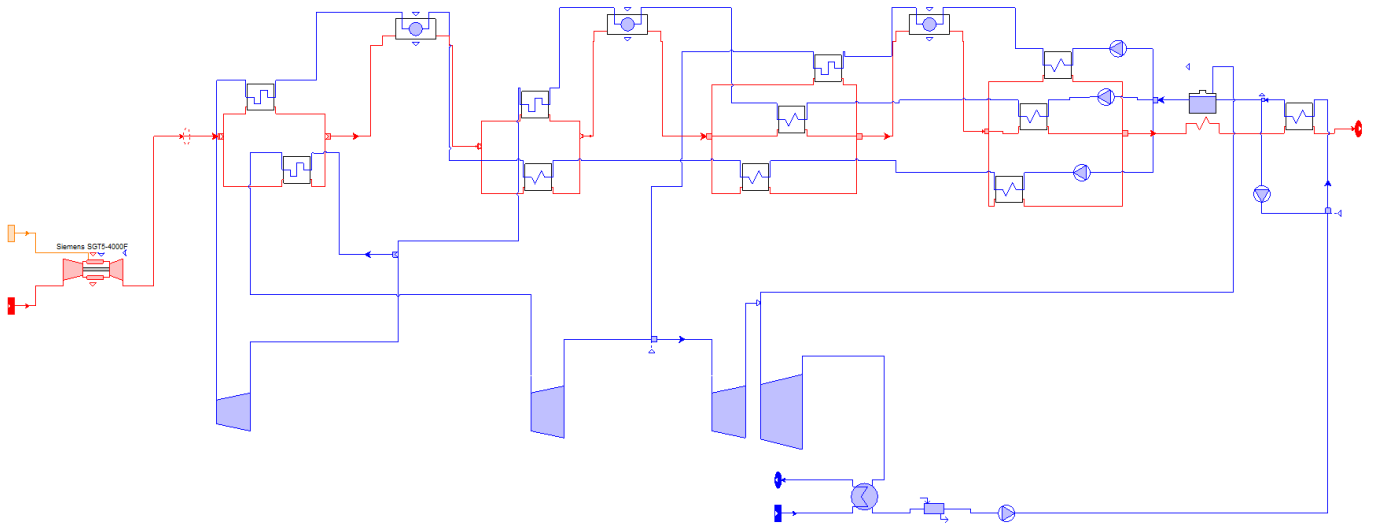


Figure 5.7: Combined-cycle model architecture in THERMOFLEX.

5.3.2 Cycle-Tempo

The Cycle-Tempo model is based on that of THERMOFLEX and therefore has the exact same layout and parameter settings. Using the available apparatus in Cycle-Tempo the architecture as displayed in Figure 5.8 was created (a larger version is available in Appendix A, Figure A.4). Purple streams represent flue-gases, red streams represent steam and blue streams represent water. The heat loss per heat exchanger was not set to equal that of THERMOFLEX but set to zero due to simplicity.

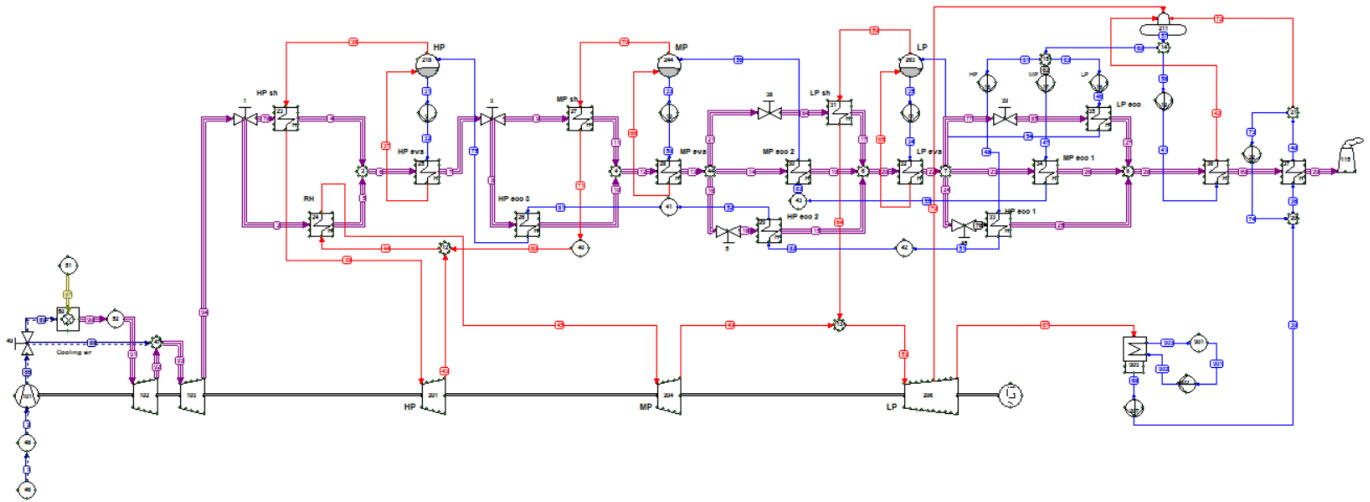


Figure 5.8: Combined-cycle model architecture in Cycle-Tempo.

5.4 Results

After having performed the simulations using both software minor differences were discovered. These differences and their probable causes are presented in this section. First the design point results are presented and discussed followed by the off-design results.

Design Point Performance

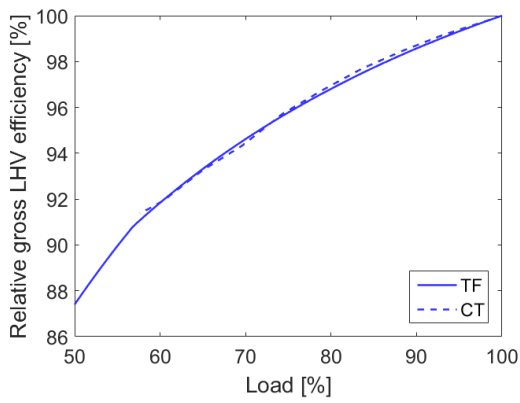
The design point simulation results are presented in Table 5.3. A major difference can be found in the power ratios between the gas and steam turbines. The addition of a HRSG decreased gas turbine output power more than it does in THERMOFLEX. As a direct result, Cycle-Tempo's steam turbine's power output has to increase to meet the exact same total gross power. The combination of the lower gas turbine efficiency and modelled HRSG heat losses leads to a lower estimated design point efficiency.

Table 5.3: Combined-cycle design point simulation results at ISO conditions(40).

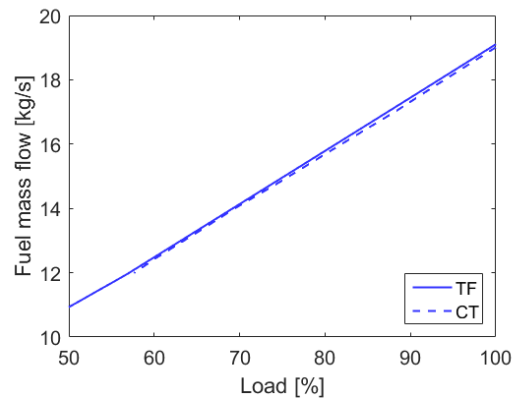
Parameter	Cycle-Tempo	THERMOFLEX	Difference	Unit
Gross power output	430.80	430.80	0%	[MW]
Gross gas turbine output	284.69	287.02	-0.82%	[MW]
Gross steam turbines output	146.11	143.78	1.59%	[MW]
Gross LHV efficiency	59.68	59.30	0.64%	[%]
Fuel mass flow	18.99	19.11	-0.66%	[kg/s]
HP steam temperature	565	565	0%	[°C]
HP steam pressure	125	125	0%	[bar]
MP steam temperature	565	565	0%	[°C]
MP steam pressure	30	30	0%	[bar]
LP steam temperature	305	305	0%	[°C]
LP steam pressure	5	5	0%	[bar]

Off-design Performance

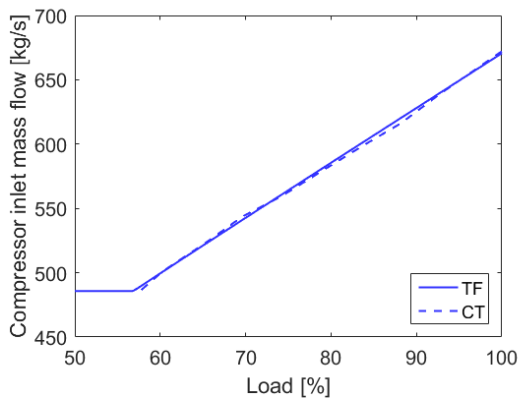
The change of plant performance with a change in load is displayed in Figure 5.9. Off-design behaviour is modelled for constant turbine outlet temperature. The most important curve is that which displays the relative LHV efficiency visible in Figure 5.9a. This curve together with the design point results allow its annual performance to be computed. At high loads Cycle-Tempo estimates higher efficiencies than THERMOFLEX. However, around the 75% mark the opposite is true. Most curves are nearly identical except for those in Figure 5.9d. Unfortunately Cycle-Tempo was unsuccessful in computing the plants performance for off-design conditions when the IGV had reached its maximum angle. It is therefore that its results do not span the same relative power range as that of THERMOFLEX.



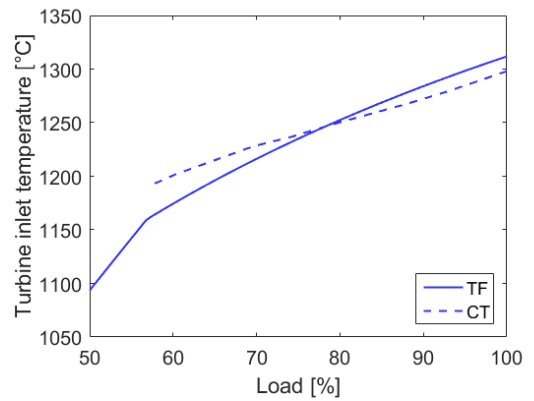
(a) Gross efficiency (26)



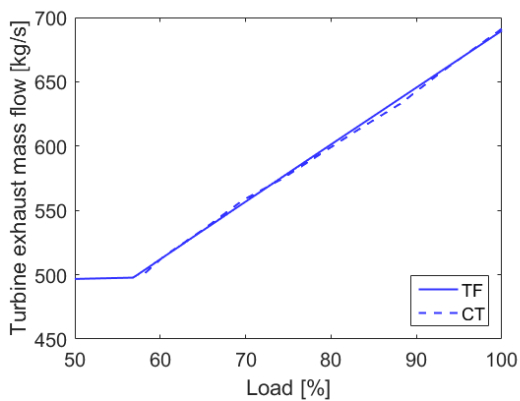
(b) Fuel mass flow



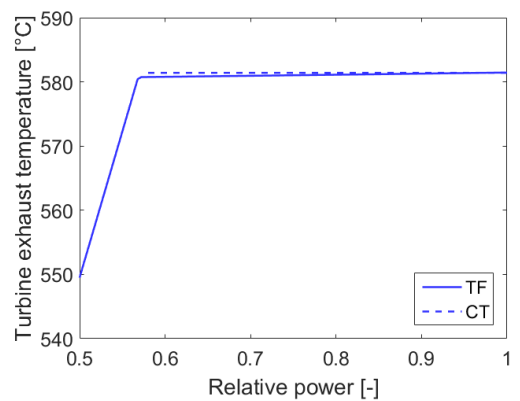
(c) Compressor inlet mass flow



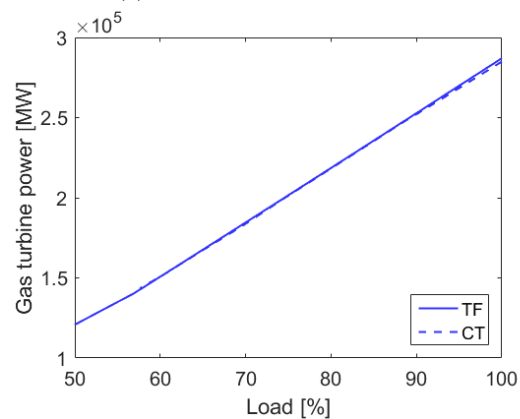
(d) Turbine inlet temperature



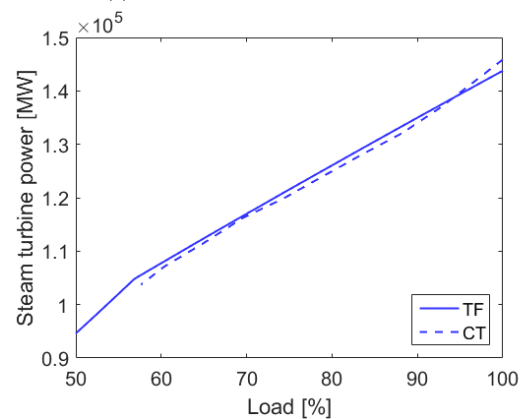
(e) Turbine exhaust mass flow



(f) Turbine exhaust temperature



(g) Gas turbine power generation



(h) Steam turbine power generation

Figure 5.9: Combined-cycle off-design simulation results for THERMOFLEX (TF), GSP and Cycle-Tempo (CT) at ISO conditions.

5.5 Validation

To validate the found gross efficiency, the simulation results are compared to literature. It must be noted here that it is unknown which exact gas turbines and combined-cycle architectures were evaluated in literature. However, these curves still give an indication on the validity of the simulation results. The comparisons for the SGT5-4000F and combined-cycle are presented in Figure 5.10a and Figure 5.10b respectively.

5.5.1 Gas Turbine Validation

To provide an indication of the gas turbine simulation accuracy its trajectory is compared to literature (see Appendix A, Figure A.5(26)). One can say that all curves except those of GSP are in agreement for loads above 55%. The general trends for the compressor mass flow and turbine exhaust temperature also match those found in literature for the SGT-4000F (see Appendix A, Figure A.6(47)). Therefore it can be concluded that the gas turbine model produces plausible results to represent the Siemens SGT5-4000F gas turbine.

5.5.2 Combined-Cycle Validation

Compared to literature, both THERMOFLEX and Cycle-Tempo underestimate plant performance. At deep part load both software have a larger deviation from the performance curves presented in literature. The reference data shows a deviation in comparison to the simulations. A possible cause is the different simulated combined-cycle architecture. The combined-cycle model results do not match literature as well as those from the gas turbine model. Therefore, it can be concluded that the accuracy of the combined-cycle model must be taken into account when a conclusion is made upon the simulated results.

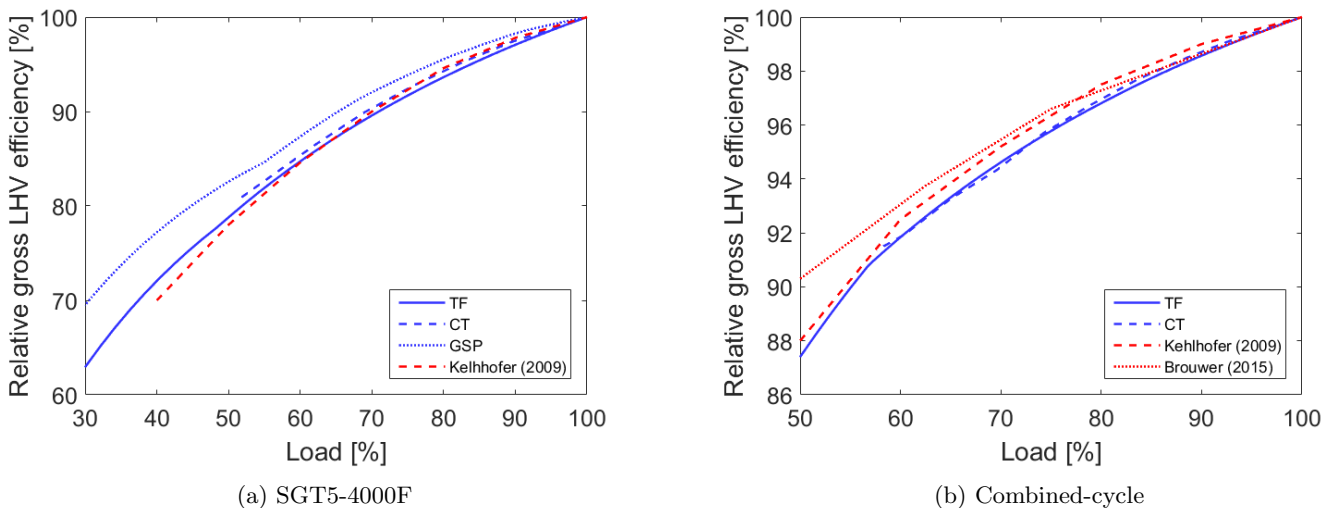


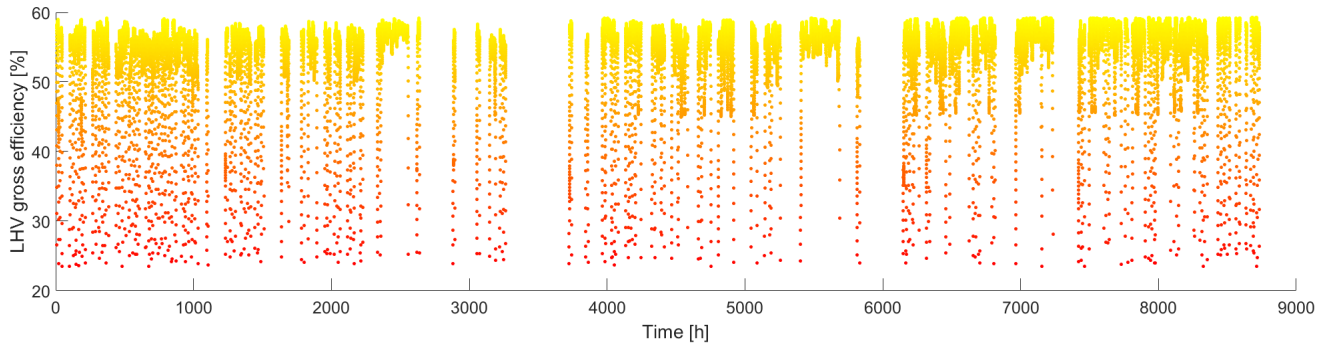
Figure 5.10: Model validation(26; 8).

5.5.3 Annual Performance

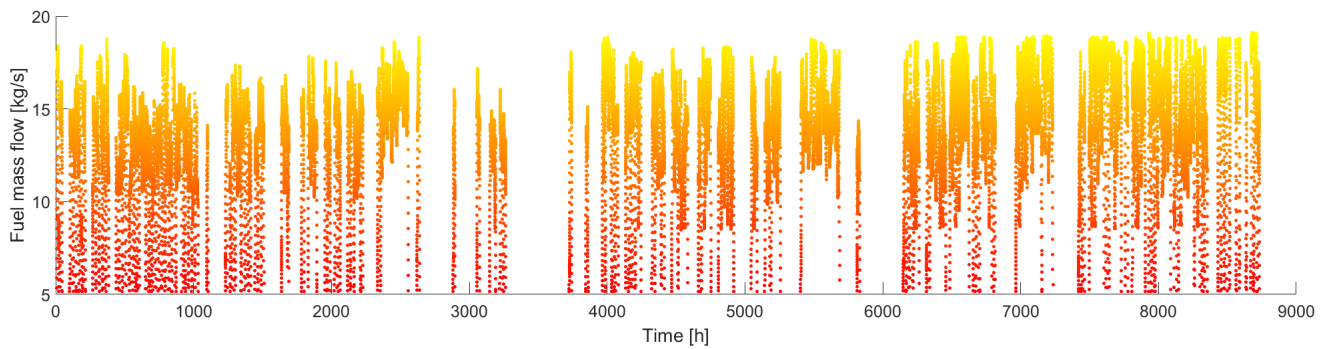
Annual plant performance is computed using the simulation results from THERMOFLEX since Cycle-Tempo could not successfully simulate off-design conditions when the IGV had reached its maximum angle. The plants annual performance based on the steady-state simulation data and the annual operating pattern is presented in Table 5.4. It must be noted that start-up and shut-down procedures have not been modelled since a steady-state model was used. Since the operating pattern has a minimum time step of one hour the accuracy can be increased by interpolating between data points to match the curtailment model time step. A linear interpolation is used to create data points with a time step of 5 minutes. Using these data points, the annual power generation, fuel consumption, air consumption and carbon-dioxide (CO_2) emitted is computed. The amount of carbon-dioxide emitted is computed via the emission factor for natural gas(48). This factor is computed from the composition of Slochteren natural gas, as displayed in Table 5.1 and was found to be 56 kt/PJ(48).

Combing the performance curves presented in Figure 5.9a and Figure 5.9b with the plants annual operating pattern leads to the patterns presented in Figure 5.11. A quick inspection indicates that the plant often operates at off-design conditions and therefore at lower thermal efficiencies. Plotting the number of occurrences for both parameters leads

to Figure 5.12. The plant more often operates at off-design points but does seem to operate in the high efficiency region. The average gross thermal efficiency for 2015 was 55.11%.

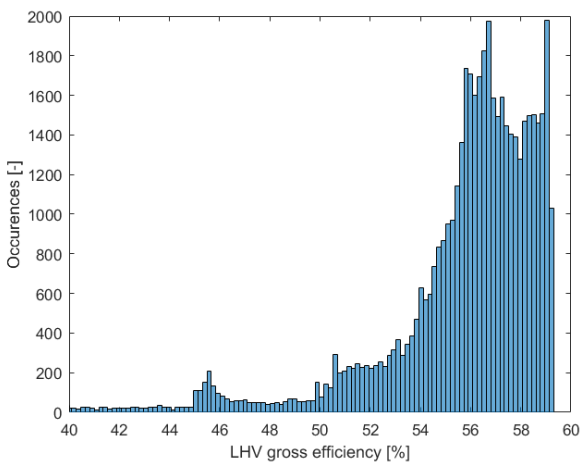


(a) Gross thermal efficiency (LHV)

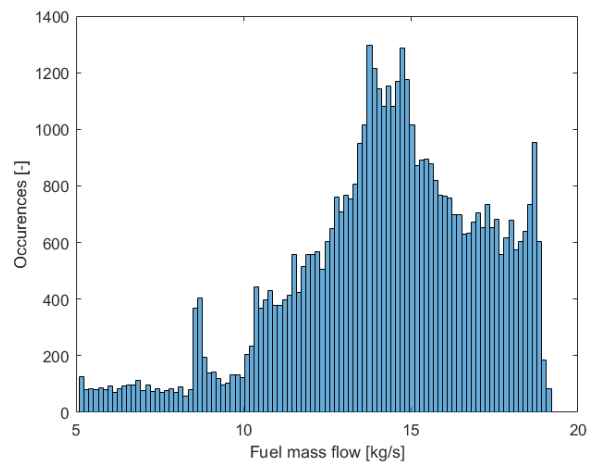


(b) Fuel mass flow

Figure 5.11: Annual gross thermal efficiency and fuel mass flow patterns.



(a) Gross thermal efficiency (LHV)



(b) Fuel mass flow

Figure 5.12: Annual occurrence distribution for the gross thermal efficiency and fuel mass flow.

Table 5.4: Annual power plant performance (2015).

Parameter	Value	Unit
Energy generated	1,257,234	[MWh]
Operating hours	4220	[hour]
Average gross efficiency	55.11	[%]
Natural gas consumption	212,030	[tonne]
Air consumption	8,278,198	[tonne]
CO ₂ emitted	451,191	[tonne]

5.6 Conclusions and Observations

In the beginning of this chapter requirements were established to select a proper CCPP to use as reference plant. Five major requirements led to the Hemweg 9 power plant to be taken as a suitable reference. Its operating pattern and technical data were used as a baseline for the case study plant. The Hemweg 9 uses a Siemens SGT5-4000F gas turbine, a Siemens SST-5000 steam turbine and a Siemens SGen5-2000h hydrogen cooled generator. It uses a three-pressure stage HRSG and represents a state of the art CCPP for the Dutch generation mix.

To successfully model the power plants performance the Siemens SGT5-4000F gas turbine was modelled separately by means of three different simulation software; THERMOFLEX, GSP and Cycle-Tempo. For the design point simulation all three software yielded similar results and can therefore all be used for gas turbine design point simulation. For off-design simulations results differed to a greater extent. THERMOFLEX and Cycle-Tempo yielded similar simulation results in contrast to GSP. This can partly be accredited to the detailed modelling of the isentropic efficiency of the compressor and turbine by GSP.

The developed off-design gas turbine models were used to create the CCPP model. Since GSP was unable to model a complete CCPP plant (without models developed by the user) only THERMOFLEX and Cycle-Tempo were used for this purpose. For both models the exact same architecture was simulated under both design point and off-design points. To aid in developing the model Siemens data reports and reference plants with the same output power were used. Design point simulations results matched well for both software. Off-design performance simulation results from both software also showed similar results for all parameters of interest except for the TIT.

Finally, the CCPP results from THERMOFLEX were used together with the Hemweg 9 operating pattern for 2015 to simulate the power plants annual performance. Its annual power energy output, fuel consumption and greenhouse emissions were calculated and presented. In conclusion, a successful CCPP model has been created by using THERMOFLEX and Cycle-Tempo using the Hemweg 9 as a reference. The annual performance of the simulated plant can act as a baseline case to assess the effects of curtailment utilization.

Chapter 6

Energy Storage

Chapter 3 showed that curtailment is often present during low demand hours. During these periods, CCPPs are often inoperative leading to a mismatch between when the occurrence of curtailment and CCPP operation. The presence of this mismatch is proven in the first section of this chapter. As a solution, temporary energy storage can be used. The second section aims to give the reader an overview of various electrical energy storage methods and their working principles. A techno-economic characteristic performance overview for each of these methods is provided for comparison. Finally, observations are presented and a storage method is chosen that best suits the application of curtailment utilization.

6.1 Curtailment and CCPP Operation

The model described in chapter 3 predicts curtailment to occur more often during times of low residual loads due to the constant RR limit. From Figure 6.1, it can be seen that curtailment mainly occurs between 0:00 and 10:00 o'clock. On the contrary, the Hemweg 9 CCPP is often not operative between 0:00 and 7:00 as displayed in Figure 6.1. To assure that curtailment can be collected during the morning and used at a later time of day, an energy storage can be implemented between wind farms and the CCPP.

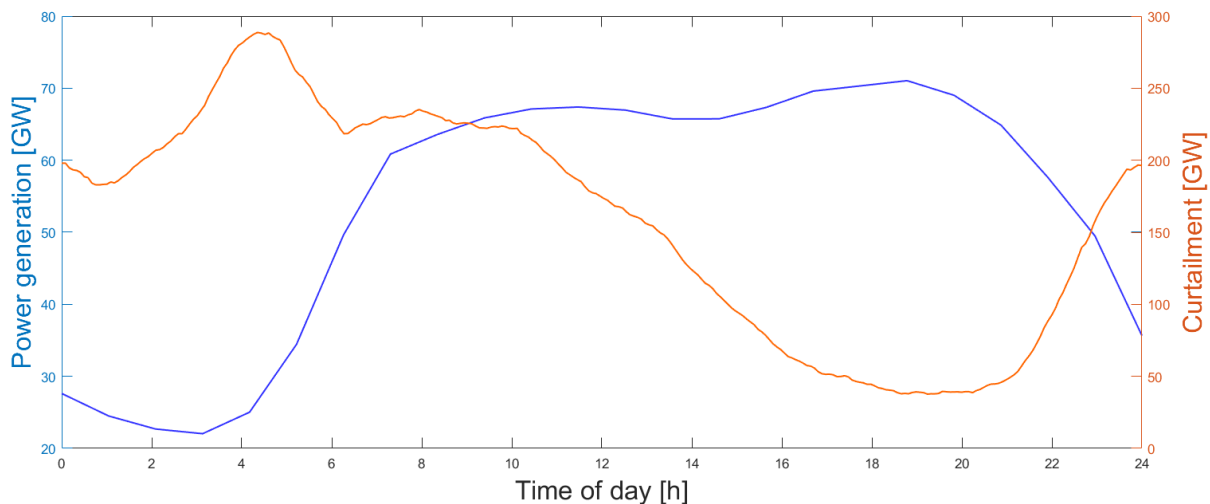


Figure 6.1: Time of day distributions for the occurrence of curtailment at 30% wind penetration and the Hemweg 9 operating pattern for 2015.

6.2 Energy Storage Methods

Energy storage (ES) has been given a lot of attention by the power sector in recent years(49; 10; 50). This interest originated from the growing share of IRES within the power sector. ES has shown to be an effective way of reducing curtailment(51). It is also an efficient way to reduce the magnitude of fluctuations in the power output by storing energy during peak production and by releasing it during low production periods. Within this project, ES will be used for this exact purpose. ES can be divided into four main categories: electrical, mechanical, thermal and chemical

storage. Using Figure 6.2 as a guideline, ES methods are categorised and their working principle is explained in each corresponding paragraph.

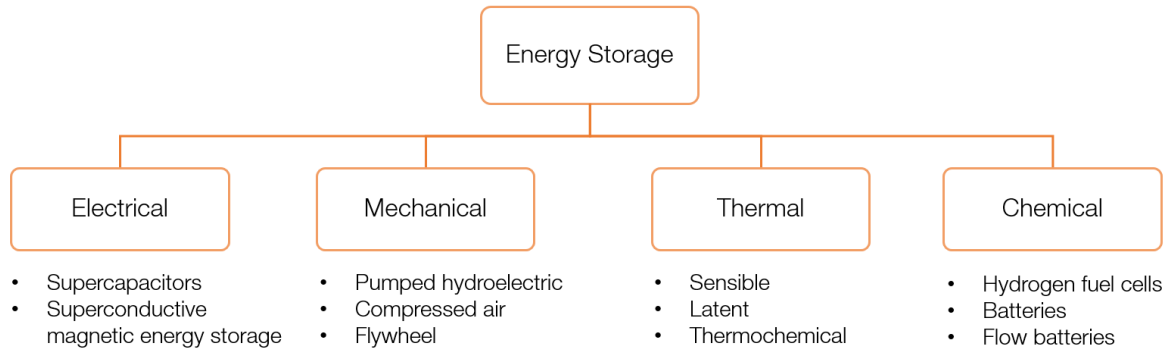


Figure 6.2: Energy storage categories and corresponding principles.

6.2.1 Electrical Storage

Electrical storage makes use of storing magnetic or electrostatic energy(52). Supercapacitors store electrostatic energy, and superconducting magnetic energy storage stores magnetic energy. The working principles of these two examples are discussed in more detail in the next two paragraphs.

Supercapacitors Supercapacitors store energy by placing an electrolyte solution between two electrodes(53). When an electric current is applied, the electrodes obtain either a positive or negative polarity. Layers of opposite polarity to the electrode’s polarity are formed and create an electric field between them. This electrical current can be discharged in order to extract electrical energy from the system(49). Supercapacitors are mainly characterised by their high parasitic loss and are therefore often used for short-term energy storage(53).

Superconducting Magnetic Energy Storage (SMES) SMES stores electrical energy by means of passing an electrical current through an inductor consisting out of superconducting material. Energy is stored in the magnetic field created by running a current through the inductor(49). The amount of energy stored is dependent on the self-inductance of the coil and proportional to the square of the electrical current(53).

6.2.2 Mechanical Storage

This type of storage stores energy in the form of potential, elastic potential or kinetic energy(52). The upcoming three paragraphs elaborate upon pumped hydroelectric, compressed air and flywheel energy storage.

Pumped Hydroelectric Storage (PHS) PHS is a large scale energy storage method where energy is stored in the form of potential energy by pumping water from a low level reservoir to a higher one(54). The amount of energy stored is proportional to the height difference of the two reservoirs and the total water mass. In times of high electricity demand, the water is released from the higher level reservoir through a hydro turbine present on a lower level to produce electric power. In periods of curtailment, water is pumped back to the higher level reservoir(55). PHS is one of the most common large scale energy storage methods. It represented 99% of the worlds total energy storage capacity in 2012(12).

Compressed Air Energy Storage (CAES) CAES makes use of storing gases at pressures above ambient pressure in order to release the gas at a later stage in time. To extract work from the high pressure air, it is expanded through a turbine. Large amounts of compressed air can be stored in empty oil fields, gas fields or salt caverns(49). Similar to PHS, CAES can be used for large scale energy storage. It also displays a strong dependency on geographical location due to its required storage volume. It does however have less negative impacts on its environment since the storage volume is often located underground(10).

Flywheel Energy Storage (FES) FES makes use of storing energy in the form of angular momentum. Energy can be added and removed by means of adding or removing torque to a rotating mass. The amount of energy stored within the flywheel is dependent on its inertia and the square of its rotational velocity(53). The rotating inertia of the flywheel can compensate for power fluctuations such as those present with wind and solar power sources(56). One of

the major drawbacks of using flywheels is its high self-discharge rate (55-100% per day) due to viscous and frictional losses(49). Therefore, this method is mainly effective for short-term storage applications.

6.2.3 Thermal Storage

Thermal storage can be based on three principles: sensible, latent and thermochemical heat storage. These three principles are shortly elaborated upon in the following three sections, followed by examples of common thermal storage methods which operate according to one of the three previously mentioned principles.

Sensible Heat Storage (SHS) In SHS, energy is stored in the form of a temperature change of a medium. Heat is added to increase the temperature and released at a later stage without a phase change. Such a process, which solely causes a change in temperature is called sensible heat(57; 58; 59). Both liquids and solids can be used as storage media. In the case of solids, mainly high temperature concrete or ceramics are used in combination with a heat transfer fluid to exchange heat(59). For liquid media, molten salts and oils are popular due to their thermal stratification properties and melting points(59).

Latent Heat Storage (LHS) in LHS heat is stored as the energy required to change the phase of a medium, for example from solid to liquid. During a phase change, heat is added or removed from the substance but no temperature change can be observed(57; 58). The most often used are solid-solid and solid-liquid transitions(59; 60). Solid-solid transitions can occur when the internal crystalline structure of a material changes. Transitions to gas phase are not common due to their negative storage properties (large volumes and high pressures). A substance specifically used for this purpose is called a phase change material (PCM)(59). PCMs allow for large amounts of energy to be stored in relatively low volumes, leading to low storage costs(59).

Thermochemical Heat Storage (THS) THS makes use of reversible chemical reactions in order to store and release heat. Heat is added during an endothermic chemical reaction process and is released during an exothermic chemical reaction. A major benefit of this method is that energy can be stored indefinitely and high energy densities can be obtained(59).

Each of the three previously explained methods is based on a different principle and therefore their performances differ. Table 6.1 displays their characteristics and relative performance on a conceptual level.

Table 6.1: Thermal energy storage concept comparison. Based on (61).

Characteristic	Sensible	Latent	Thermochemical
Capacity	weak	weak	large
Recovery temperature	variable	constant	variable
Insulation required	yes	yes	no
Long term losses	high	fair	low
Life	long	limited	high
Environmental impact	none	none	can be hazardous
Technology	simple	simple	complex

Two examples of commonly used thermal energy storage methods are given in the following two paragraphs. These examples can be categorised under the previously mentioned principles based on whether a temperature change, phase change or chemical reaction occurs.

Cryogenic Energy Storage (CES) CES uses low temperature liquids such as air or nitrogen as energy storage media. These liquids require a very small volume in comparison to their gaseous counterparts. When energy is to be extracted, the liquids are heated by the surrounding environment(49). This heating process greatly increases the volume and pressure of the medium. This trait is used to drive a cryogenic heat engine which produces electricity(49). It is considered to be a thermal storage in the low temperature region.

Salts Popular media for heat storage are various compositions of salts(62). These salts make use of sensible, latent and thermochemical types of heat storage. For most applications, the lower and upper limits of heat storage play a significant role. This characteristic, amongst others, is dependent on the salt composition. Table 6.2 provides an overview of various salt compositions, their operating temperature range and the thermal storage category under

which they can be classified. It can be observed that the temperature range and storage principle differs based on the composition of the exact mixture.

Table 6.2: Salt compositions characteristics. Modified from (62).

Salt	Water-salt mixtures	Melting of salt hydrates	Absorption in salt	Dehydration of salt hydrates
Temperature range [°C]	< 0	0-100	40-150	40-300
Storage principle	Latent	Latent	Thermochemical	Thermochemical
Salt	Solid-liquid anhydrous	Anhydrous solid	Anhydrous molten	Solid-solid anhydrous
Temperature range [°C]	120-500	100-800	100-800	100-800
Storage type	Latent	Sensible	Sensible	Latent

6.2.4 Chemical Storage

Chemical storage mainly stores energy in the form of chemical and electrochemical energy(52). This can be done in the form of hydrogen, batteries and flow batteries. These are discussed in detail in the upcoming three paragraphs.

Hydrogen Hydrogen can be produced by several methods. The two main methods are electrolysis and solar conversion(63; 64; 65). Electrolysis uses electricity to split water into hydrogen and oxygen. Solar conversion allows an endothermic reaction to take place in order to split water into hydrogen and oxygen. Other methods use chemical reactions to split fuel into hydrogen and secondary products.

Batteries Batteries consist of a negative terminal and positive terminal. When a battery is connected to an electric grid ions (particles with a positive charge) and electrons (particles with a negative charge) flow in opposite directions. This change in electric loads creates an electric flow through the battery and the grid. Several examples of such batteries are lithium-ion, sodium-sulfur, nickel-cadmium and zinc bromide batteries(52).

Flow Batteries Flow batteries pump electrolytes through two half-cells present in the main reaction cell. When the battery is discharged, chemical energy present in the electrolytes is released and can be extracted by the electrodes. When charging, an electrical current passes through the system, allowing for a redox reaction to take place. A reduction reaction takes place in one of the electrolytes and an oxidation reaction in the other. A membrane allows for ions to pass through it, creating an electrical current. Various types of flow batteries make use of bromine with several variants such as zinc, sodium and vanadium(66).

6.3 Techno-economic Performance Overview

To compare various ES methods with one another, their individual performance is summarized and presented in Table 6.3 and Table 6.4. The following criteria are included within these overviews: costs per kilowatt-hour, discharge at rated capacity, rated capacity, efficiency, technology maturity, lifetime, environmental impact, discharge duration and storage duration. Due to the large spread of numerical values found in literature, only the most extreme values have been displayed. Sources which fall within this range are displayed in the final column. These results are analysed in the next section.

Table 6.3: Energy storage techno-economic characteristics. Modified from (10).

Storage Method	Cost [\$/kWh]	Discharge at Rated Capacity [h]	Rated Capacity [MW]	Efficiency [%]	Sources [-]
Electrical Storage					
Capacitors	500 - 1000	$2.7 \cdot 10^{-7} - 1$	0 - 0.05	60 - 70	(49)
Supercapacitors	300 - 2000	$2.7 \cdot 10^{-3}$	0.10	84 - 98	(49; 67; 68; 69; 70)
SMES	1000 - 10,000	$2.7 \cdot 10^{-7} - 0.0022$	0 - 100	21 - 97	(49; 67; 68)
Mechanical Storage					
PHS	5 - 100	1 - 24	1 - 5000	71 - 85	(49; 67; 68)
CAES	2 - 50	1 - 24	5 - 3000	70 - 89	(49; 67; 68; 69)
FES	1000 - 5000	0 - 0.25	0 - 10	80 - 95	(49; 67; 68; 69; 70)
Thermal Storage					
CES	3 - 30	1 - 8	100 - 300	40 - 50	(49)
Other	20 - 60	-	0 - 300	5 - 40	(14; 49)
Chemical Storage					
Lead-acid	200 - 400	0.0027 - 8	0 - 20	63 - 90	(49; 67; 11; 71; 70)
Nickel-cadmium	800 - 1500	0.0027 - 10	0 - 40	60 - 83	(49)
Sodium-sulfur	-	0.0027 - 8	0 - 34	75 - 90	(49; 67; 11)
Lithium-ion	600 - 2500	0.0170 - 2	0 - 0.01	85 - 99	(49)
Vanadium redox	150 - 1000	0.0027 - 12	0.03 - 3	75 - 85	(49; 11)
Zinc-bromide	150 - 1000	0.0027 - 10	0.05 - 2	66 - 80	(49; 67)
Hydrogen fuel cell	-	0.0027 - 24	0.20 - 50	20 - 66	(49; 67; 11; 68; 10; 53; 66; 72; 12)

Table 6.4: Continuation of energy storage techno-economic characteristics. Modified from (10).

Storage Method	Technology Maturity [-]	Lifetime [years]	Discharge Duration [-]	Storage Duration [-]	Sources [-]
Electrical Storage					
Capacitors	Currently used	5	Milliseconds - 60 min	Seconds - hours	(49)
Supercapacitors	Under development	8 - 12	Milliseconds - 60 min	Seconds - hours	(49; 67; 68; 69; 11; 70; 66; 73)
SMES	Developed	20 - 30	Milliseconds - 8 sec	Minutes - hours	(49; 67; 68; 11; 73)
Mechanical Storage					
PHS	Currently used	30 - 60	1 - 24 hours	Hours - months	(49; 67; 74; 75; 76)
CAES	Currently used	20 - 40	1 - 24 hours	Hours - months	(49; 67; 76; 75; 68)
FES	Currently used	15	Milliseconds - 15 min	Seconds - minutes	(49; 67; 68; 69; 70; 73; 74)
Thermal Storage					
Cryogenic	Under development	20 - 40	1 - 8 hours	Minutes - days	(49)
Other	Developed	5 - 40	1 - 24 hours	Minutes - months	(14; 49)
Chemical Storage					
Lead-acid	Under development	5 - 15	Seconds - hours	Minutes - days	(49; 11; 71; 70)
Nickel-cadmium	Under development	10 - 20	Seconds - hours	Minutes - days	(49; 70)
Sodium-sulfur	Commercializing	10 - 15	Seconds - hours	Seconds - hours	(49; 67; 73; 76; 70; 13)
Lithium-ion	Commercializing	5 - 15	Minutes - hours	Minutes - days	(49; 76; 70)
Vanadium redox	Developed	5 - 10	Seconds - 10 hours	Hours - months	(49; 11; 76; 13)
Zinc-bromide	Developed	5 - 30	Seconds - 10 hours	Hours - months	(49; 67; 11; 76; 13; 69)
Hydrogen fuel cell	Under development	5 - 20	Seconds - 24 hours	Hours - months	(49; 67; 11; 76; 68; 69; 10; 53; 66; 72)

6.4 Conclusions and Observations

Table 6.3 and Table 6.4 illustrate that each ES method has different techno-economic performance characteristics. No single ES system has an excellent performance regarding all criteria. Therefore, suitable candidates have to be identified according to their strengths, weaknesses and their compatibility with gas turbines. By observing the characteristics illustrated in Table 6.3 and Table 6.4, the following observations can be made:

- The cost per kWh of electricity stored is the highest for electrical storage. It is the lowest for PHS and CAES, followed by thermal storage.
- Although thermal storage has a relatively low electricity cost per kWh, its conversion efficiency is amongst the lowest. Top performers in terms of efficiency are supercapacitors, flywheels and lithium-ion batteries.
- No single ES method has both a small discharge duration and a long storage duration. Combining multiple storage methods can allow for these operational limits to improve. More beneficial discharge/storage durations can be achieved by using a combination of ES methods.
- The use of PHS, CAES and flywheels requires several energy conversion steps (electrical energy \rightarrow mechanical energy \rightarrow potential/rotational energy \rightarrow mechanical energy \rightarrow heat). PHS and CAES are less suitable candidates due to their large scale operation, geographic dependency and energy conversion process. For flywheels, its high daily self-discharge rate is rather high, leading to ineffective long term storage.
- Judging from the optimal energy conversion process (electrical energy \rightarrow heat) two major locations for energy storage can be identified: before and after energy conversion. This means that energy has to either be stored as electricity or as heat. This indicates that electrical and thermal storage as possible options.

Based on these observations, it has been concluded that thermal energy storage is a suitable candidate for the temporary storage of curtailment. The main factors which influenced this decision were its beneficial energy conversion process and relatively low costs. The low conversion efficiency associated with thermal storage has not been deemed extremely important due to the fact that curtailment is available in large quantities compared to the required curtailment and it is practically "free" since it is currently not used for any other purpose. Within thermal energy storage, latent heat storage seems promising due to its constant recovery temperature and simple technology. Its simplicity is matched by sensible heat storage which is almost always a part of a latent heat storage during a lengthy discharge below the PCM's melting point. Therefore, it is decided that a combination of latent and sensible heat storage shall therefore be used for the storage of curtailment.

Chapter 7

Curtailment Utilization

The goal of this chapter is to identify the most beneficial method of using curtailment in CCPs to displace natural gas. Based on the previous chapter where thermal storage was identified as a suitable candidate for energy storage, two major methods are evaluated which successfully serve this purpose. The first is to increase the compressor outlet temperature before it enters the combustion chamber. By doing so, the temperature gap which has to be overcome in the combustion chamber decreases and the required fuel mass flow decreases. The second method involves increasing the temperature of natural gas before it enters the combustion chamber. This increases its energy content and results in a lower fuel mass flow required to achieve the same energy input into the gas turbine cycle. These two methods, the heating of compressor exhaust air and the heating of natural gas, are compared regarding four different fields of interest to reveal their respective benefits and drawbacks. The first comparison is made by identifying at which location in the gas turbine it is more efficient to add energy: at the fuel lines or after the compressor. This is done by an energy analysis of the combustion chamber. Secondly, each method is evaluated in terms of the maximum amount of energy it can add to the system. The characteristics of the existing system put limits on energy content and influence its overall impact. The third criterion reveals which gas, air or natural gas, can absorb energy more easily by means of convection. This is done by identifying the heat transfer coefficient for both gases for two generic types of heat exchangers. Finally, practical considerations which have not been taken into account in the previous three criteria are presented and elaborated upon. To summarize, each method will be evaluated on the following criteria:

- Most beneficial location of energy addition
- Maximum transferable energy
- Ease of energy transfer to gas via convection
- Practical considerations

7.1 Most Beneficial Location of Energy Addition

To gain a better insight on the most beneficial location of energy addition an energy analysis for the gas turbine combustion chamber is performed. The method is considered to be the most beneficial when its required fuel mass flow is the lowest. The energy analysis allows the required fuel mass flow to be related to the combustion chamber air inlet temperature (T_{inlet}) and fuel enthalpy. This analysis used the expression for the fuel mass flow as presented in Equation 7.1.1.

$$\dot{m}_f = \frac{\dot{m}_{air} C_{p,air} (TIT - T_{inlet})}{\eta_{cc} LHV} \quad (7.1.1)$$

Using this equation the impact of heating compressor exhaust air from T_{inlet} to T_{new} can be quantified. The temperature increase depends on the amount of energy added to the gas, its mass flow and specific heat capacity. This relation, displayed in Equation 7.1.2, can be rewritten to an expression for the heated compressor exhaust temperature as shown in Equation 7.1.3.

$$Q = \dot{m}_{air} C_{p,gas} (T_{new} - T_{inlet}) \quad (7.1.2)$$

$$T_{new} = T_{inlet} + \frac{Q}{\dot{m}_{air} C_{p,gas}} \quad (7.1.3)$$

Substituting Equation 7.1.3 into Equation 7.1.1 leads to Equation 7.1.4. This equation directly relates the effect of a higher combustion inlet temperature to the required fuel mass flow.

$$\dot{m}_{f,air\ heating} = \frac{\dot{m}_{air}C_{p,gas}(TIT - T_{inlet} - \frac{Q}{\dot{m}_{air}C_{p,gas}})}{\eta_{cc}LHV} \quad (7.1.4)$$

The same expression can be obtained for the heating of natural gas. In this case, the change in gas temperature relates to a change in the fuel's enthalpy. Its enthalpy consists out of two parts: chemical enthalpy and thermal enthalpy(77). This relation is presented in Equation 7.1.5. Equation 7.1.2, which relates the heat added to a temperature increase, also holds for natural gas. Using this knowledge, Equation 7.1.5 can be rewritten to Equation 7.1.6.

$$h_{final} = h_{initial} + C_{p,gas}(T_{final} - T_{initial}) \quad (7.1.5)$$

$$h_{final} = h_{initial} + \frac{Q}{\dot{m}_{f,fuel\ heating}} \quad (7.1.6)$$

Substituting Equation 7.1.6 into Equation 7.1.1 leads to an expression for the required fuel mass flow as a function of the amount of heat added to the natural gas. This expression is as shown in Equation 7.1.7. Rewriting this equation to isolate the fuel mass flow leads to Equation 7.1.8.

$$\dot{m}_{f,fuel\ heating} = \frac{\dot{m}_{air}C_{p,gas}(TIT - T_{inlet})}{\eta_{cc}(LHV + \frac{Q}{\dot{m}_{f,fuel\ heating}})} \quad (7.1.7)$$

$$\dot{m}_{f,fuel\ heating} = \frac{\dot{m}_{air}C_{p,gas}(TIT - T_{inlet}) - Q\eta_{cc}}{\eta_{cc}LHV} \quad (7.1.8)$$

Two expressions for the fuel mass flow have been derived for both compressor exhaust air and natural gas heating. They can be compared to one another for the same amount of added energy, Q. This is done by evaluating the ratio between these two expressions as is visible in Equation 7.1.9. A ratio larger than one indicates that it is more beneficial to heat natural gas. For ratio's smaller than one, heating compressor exhaust air is more beneficial.

$$\frac{\dot{m}_{f,air\ heating}}{\dot{m}_{f,fuel\ heating}} = \frac{\frac{\dot{m}_{air}C_{p,gas}(TIT - T_{inlet} - \frac{Q}{\dot{m}_{air}C_{p,gas}})}{\eta_{cc}LHV}}{\frac{\dot{m}_{air}C_{p,gas}(TIT - T_{inlet}) - Q\eta_{cc}}{\eta_{cc}LHV}} \quad (7.1.9)$$

Equation 7.1.9 can be rewritten for convenience according to the intermediate steps as shown below.

$$\frac{\dot{m}_{f,air\ heating}}{\dot{m}_{f,fuel\ heating}} = \frac{\dot{m}_{air}C_{p,gas}(TIT - T_{inlet} - \frac{Q}{\dot{m}_{air}C_{p,gas}})}{\dot{m}_{air}C_{p,gas}(TIT - T_{inlet}) - Q\eta_{cc}} \quad (7.1.10)$$

$$\frac{\dot{m}_{f,air\ heating}}{\dot{m}_{f,fuel\ heating}} = \frac{\dot{m}_{air}C_{p,gas}(TIT - T_{inlet}) - Q}{\dot{m}_{air}C_{p,gas}(TIT - T_{inlet}) - Q\eta_{cc}} \quad (7.1.11)$$

If the temperature gap which has to be overcome in the combustion chamber is set to X, the ratio can be simplified and its value computed. Performing this substitution leads to the final expression as shown below.

$$\frac{\dot{m}_{f,air\ heating}}{\dot{m}_{f,fuel\ heating}} = \frac{X - Q}{X - Q\eta_{cc}} \quad (7.1.12)$$

If $X \gg Q$, this ratio is always smaller than one for a combustion efficiency (η_{cc}) smaller than one. Therefore, it can be concluded that from an energy efficiency point of view, it is less beneficial to add energy to natural gas rather than to compressor exhaust air. It must be noted that the assumption was made that the difference in temperature for both gases does not influence the combustion efficiency. Therefore η_{cc} is assumed to be a constant smaller than one for both cases.

7.2 Maximum Transferable Energy

Before a method can be successfully chosen, one must consider the maximum energy that can be added to the system. This section aims to quantify this for both heating concepts. It does so by using the yearly simulation data presented in chapter 5 to compute the maximum amount of air and fuel available for heating. This analysis assumes that all air and fuel is heated to their respective maximum temperature throughout a complete year. This might not be the case for an actual power plant and therefore the numbers displayed in this section are rather optimistic. However, they do give a reasonable estimation on how much there is to gain by both methods in terms of fuel consumption and CO₂ emission reduction.

7.2.1 Natural Gas Heating

For the heating of fuels, the Modified Wobbe-Index (MWI) must be taken into account. This index is of great importance when it comes to fuel versatility. It imposes a limitation on the maximum temperature which a fuel can obtain while remaining compatible with an existing combustion chamber design. The MWI is a calculated measurement for volumetric energy content of a fuel and depends on the LHV, specific gravity of the gas compared to air at ISO conditions and its absolute temperature (78). Its mathematical expression is shown in Equation 7.2.1.

$$MWI = \frac{LHV}{\sqrt{T_{gas} \frac{\rho_{gas}}{\rho_{air}}}} \quad (7.2.1)$$

To ensure that the fuel nozzle pressure ratios remain within their required limits, the MWI has to remain within +/- 5% of its target value(78). When the fuel composition and its corresponding LHV are consistent, the MWI only changes with a change in temperature. For Slochteren gas, the maximum temperature difference can be derived the acceptable 5% deviation and the MWI at 15°C. To perform this successfully, the density change with a change in fuel temperature has to be taken into account. By using THERMOFLEX, the maximum allowable temperature difference can be determined when the reference temperature of the fuel is set to 15°C. This temperature difference is found to be approximately 31 degrees leading to a final temperature of 46 °C. One can exceed this value in two ways. Firstly, by adjusting the burner to allow for larger MWI deviations from the target value. Secondly, by replacing the combustion chamber completely and thereby increasing the MWI target value. However, the MWI deviation limits still holds but the target value has changed. When such a modification is performed, it means that the gas has to be heated constantly in order to remain within the new MWI target limit. Using the results from the annual power plant simulations one can compute the energy required to increase the temperature of natural gas by 31 degrees. The result indicates the amount of energy added to the system coming from curtailment and thereby, the amount of energy which does not have to be supplied by fossil fuels. Aside from the temperature difference imposed by the MWI, it was found that a combined-cycle power plant in the Netherlands using a similar SGT5-4000F gas turbine can achieve a natural gas temperature of approximately 160°C without experiencing problems. Therefore, the annual results for a temperature difference of a 145 degrees are also included in this analysis. The heat capacity for the computations are all taken at the mean temperature: $(T_{final} - T_{initial})/2$. The results are presented in Table 7.1.

Table 7.1: Estimated maximum annual fuel savings for Slochteren gas heating.

Fuel consumption [tonne/year]	Energy consumption [GJ/year]	Fuel temperature increase [°C]	Energy added [GJ/year]	Fuel consumption reduction [%/year]
A	B	C	D = A · C · C _p	E = D/B · 100
212,030	8,056,927	31	13,420	0.1648
212,030	8,056,927	145	67,955	0.8500

7.2.2 Air Heating

The gas turbine also imposes a limit when it comes to air heating. At the design point the compressor exhaust temperature is the highest, being 455°C. This temperature only decreases in the off-design regime. It is therefore that the design point temperature indicates the maximum allowable temperature change for air. Table 7.2 displays the fuel savings that can be achieved by air heating. As can be observed, these annual savings greatly exceed that of fuel heating. However, it must be noted that this analysis does not account for a few factors. The first is the pressure drop caused by bypassing and heating the air. As a result, the overall power plant efficiency might decrease and the total fuel savings decline. In addition, the energy required to heat the fuel requires curtailment to be present in large quantities which might not always be the case. To conclude, it can be observed that more energy can be added to the Brayton cycle by preheating air rather than natural gas. The main reasons for this include the larger mass flow of air and its higher allowable temperature increase.

Table 7.2: Estimated maximum annual fuel savings for air heating.

Energy consumption [GJ/year] A	Air consumption [tonne/year] B	Fuel temperature increase [°C] C	Energy added [GJ/year] D = B · C · C _p	Fuel consumption reduction [%/year] E = D/A · 100
8,056,927	8,278,198	50	451,596	5.61
8,056,927	8,278,198	100	907,918	11.27
8,056,927	8,278,198	200	1,834,194	22.77
8,056,927	8,278,198	300	2,778,556	34.49

7.3 Ease of Energy Transfer to Gas

The third evaluation aims to identify which gas is heated easier by means of convection. This analysis is performed by investigating two generic heat exchanger geometries. Since both air and natural gas are gases, heat transfer mainly takes place by means of convection. However, conduction does play a role in the boundary layer since the gas is stationary at close to the surface(79). It is therefore that the thermal conductivity is included within analysis. The energy transferred by means of convection between two elements can be expressed by Newton's law of cooling as displayed in Equation 7.3.1.

$$\dot{Q}_{conv} = U A_s (T_{surface} - T_{\infty}) \quad (7.3.1)$$

By means of this equation the heat rate, temperature difference and required hot surface area can be related to one another. Before this is possible, the heat transfer coefficient (HTC) must be obtained. For this purpose, its relation with the Nusselt number is used(79). This relation is shown in Equation 7.3.2.

$$U = \frac{Nu k}{L} \quad (7.3.2)$$

The Nusselt number can be expressed in terms of the dimensionless Reynolds and Prandtl numbers(79). The relation between these numbers depends on whether the flow is laminar or turbulent. The configuration at which heat transfer takes place also plays an important role. To account for this, the HTC is investigated for two different configurations: flow over a flat surface and through a smooth pipe. The HTC is evaluated for both air and methane for these two configurations. Methane was chosen to replace Slochteren gas due to simplicity. Only turbulent flows for these two configurations are considered. For these configurations, the Nusselt number can be expressed as shown in Equation 7.3.3 and Equation 7.3.5(80).

Turbulent flow over a flat surface:

$$Nu_{flat\ surface} = (0.037 Re_L^{4/5} - A) Pr^{1/3} \quad (7.3.3)$$

Where A is expressed as:

$$A = 0.037 Re_L^{4/5} - 0.664 Re_L^{1/2} \quad (7.3.4)$$

It must be noted that this equation is only valid when the Prandtl number exceeds 0.6 but is smaller than 60. The Reynolds number may not exceed $1 \cdot 10^8$ (80).

Turbulent flow through a smooth pipe:

$$Nu_{pipe} = 0.023 Re_L^{4/5} Pr^{0.4} \quad (7.3.5)$$

This relation, known as the Dittus-Boelter relation, also comes with certain restrictions. To be valid, the Prandtl number must exceed 0.5 and the Reynolds number must exceed $1 \cdot 10^4$ (79). To be able to compute the Nusselt number from these relations one must first compute the Reynolds and Prandtl numbers using Equation 7.3.6 and Equation 7.3.7 respectively. For the Reynolds number, the length L corresponds to the plate length or pipe diameter.

$$Re_L = \frac{\rho V L}{\mu} \quad (7.3.6)$$

$$Pr = \frac{\mu C_p}{k} \quad (7.3.7)$$

To create a representative case, the temperatures at which the performance of air is evaluated are taken to be 427°C and 727°C. For the natural gas, these temperatures are 15°C and 160°C. The HTC of air at 427°C is compared to the HTC of natural gas at 15°C and the 727°C values are compared to the 160°C values. Multiple temperatures are evaluated for both cases to make sure that the outcome is not just valid for one specific entry temperature. It also gives an indication of the HTC trend over a temperature range. In addition, since the compressor exhaust air is at a pressure of 18.25 bar at the design point, both gases have been evaluated at this pressure. The methane pressure has also been evaluated at this pressure although the real pressure might be higher. The characteristics of both gases at their respective temperatures are displayed in Table 7.3. The values for natural gas have been created from the properties of methane. For the composition of Slochteren natural gas please refer to Table 5.1.

Table 7.3: Gas properties of air and natural gas (methane) at several temperatures at 18.25 bar.

Parameter	Air		Natural gas		Unit	Sources
	427°C	727°C	15°C	160°C		
Density	9.05	6.33	12.68	8.11	[kg/m ³]	(81; 82)
Heat capacity	1.79	1.14	2.33	2.65	[kJ/kg K]	(81; 82)
Dynamic viscosity	34.32	43.48	11.11	15.37	[Pa/s · 1 · 10 ⁻⁶]	(81; 82)
Thermal conductivity	51.50	68.70	34.15	56.70	[W/m k · 1 · 10 ⁻³]	(83; 84)

Using Table 7.3 and Equation 7.3.2 to Equation 7.3.7, the HTC for each gas at their corresponding pressures and temperatures can be computed for different surface lengths, pipe diameters and flow velocities. To quickly observe which gas has a higher HTC, the final results are subtracted from one another. The results are shown in Figure 7.1 and Figure 7.2 for the flat surface and smooth pipe configurations respectively. As can be observed from both figures, all values represented are positive. This means that the HTC of air is smaller than that of methane at their corresponding pressures and temperatures. Therefore, a larger energy transfer is present for methane than air when using an identical heat exchanger is used.

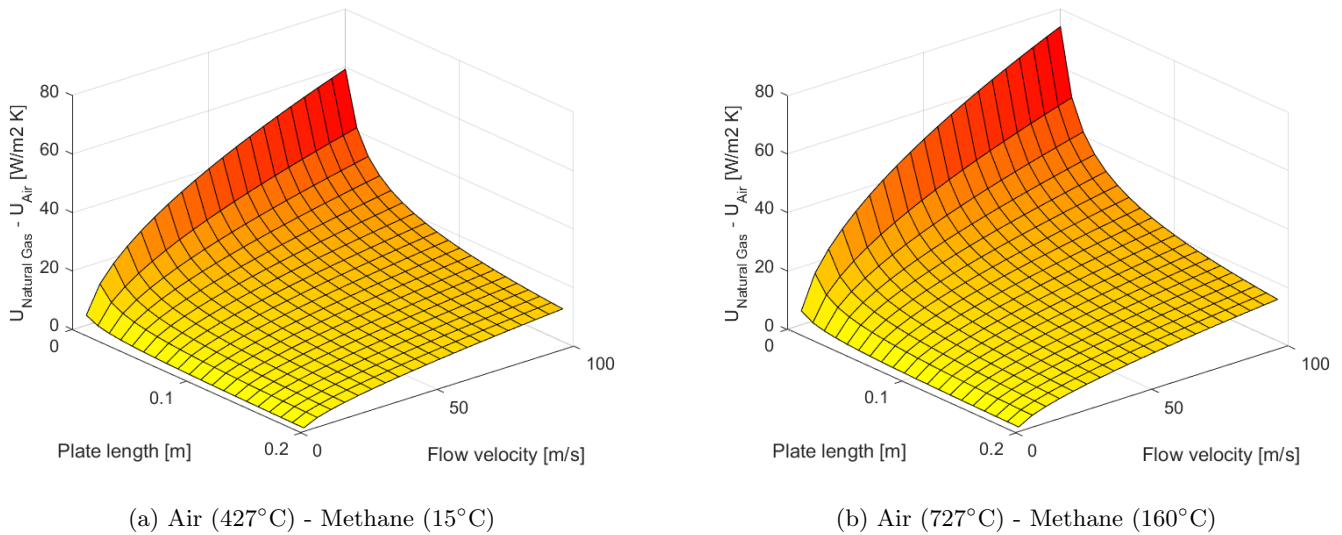
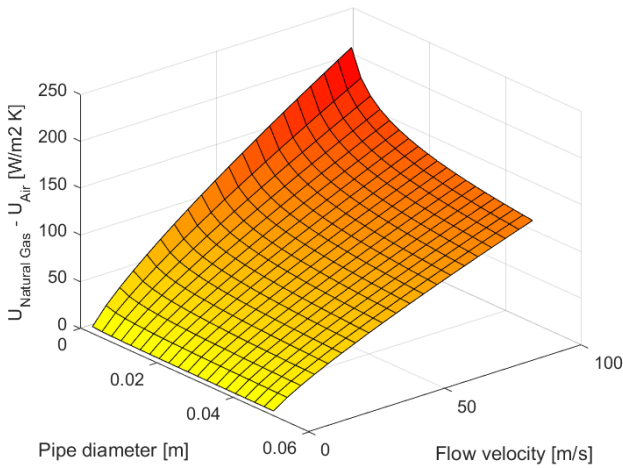
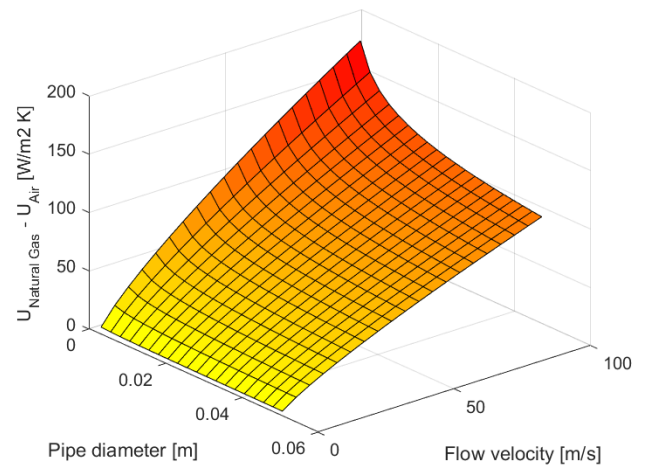


Figure 7.1: Heat transfer coefficient difference between air and methane for turbulent flow over a flat plate.



(a) Air (427°C) - Methane (15°C)



(b) Air (727°C) - Methane (160°C)

Figure 7.2: Heat transfer coefficient difference between air and methane for turbulent flow in a smooth pipe.

7.4 Practical Considerations

The final criterion concerns practical considerations to identify benefits or drawbacks not covered by the previous three criteria. This section is divided into two paragraphs. The first summarizes arguments in favour of natural gas heating. The second summarizes arguments in favour of compressor exhaust air heating.

7.4.1 In favour of natural gas heating

Since Slochteren gas can be heated before it enters the combustor there is minimal interference with the existing infrastructure. Current fuel lines can remain as they are and only a bypass has to be created to run the gas through a heater. This is not the case for compressor exhaust air heating. No matter the final design, existing gas turbines have to be modified to allow for the bypass of air through a heater. This bypass and the heat exchanger size required to heat up an airflow in the order of 420 kg/s drastically increases plant size and costs. In addition, air heating causes a pressure drop before the combustion chamber, leading to inefficient operation compared to the baseline configuration.

Currently, natural gas heaters are already in use at pressure regulation stations. The goal of these stations is to avoid condensation due to the Joule-Thomson effect and increase overall plant efficiency. Before the gas enters the combustion chamber, its pressure is reduced. With this reduction of pressure comes a significant drop in temperature which can, if not accounted for, cause condensation and the formation of hydrates. Several electrical gas heaters suitable for power plants are already commercially available (85; 86). One can use an existing and proven technology as power plant modifications.

7.4.2 In favour of compressor exhaust heating

When heating natural gas, one has to pay close attention to the auto-ignition point of the gas mixture. Auto-ignition can occur when oxygen is present within the mixture at very high temperatures. For Slochteren gas, only 0.01% of the total mixture consists of oxygen (by mole percentage). Therefore, this is not a big concern for this fuel type. However, if the auto-ignition temperature is reached and a leak occurs ignition can occur. It is therefore that strict regulations on tubing and overall plant safety must be imposed.

7.5 Conclusions and Observations

Compressor exhaust heating and Slochteren natural gas heating have been evaluated on four different criteria. The first being the most beneficial location of energy addition to the Brayton cycle. Due to the influence of the combustion efficiency on the required fuel mass flow, it was found that heating compressor exhaust air is the most beneficial. However, the combustion efficiency is often very close to one and therefore, no real conclusion can be made solely

based on this criterion. Secondly, the influence of the low Slochteren gas mass flow and allowable temperature difference in comparison to that of air significantly limits the maximum transferable energy. From this point of view, it is more beneficial to heat compressor exhaust air. To improve the performance of fuel heating, one can adjust or replace the combustion chamber to achieve a larger range of allowable gas temperature. The third analysis included an investigation of the heat transfer coefficient for both gases for two specific heat exchanger configurations: a flat surface and smooth pipe. From this analyses, it was concluded that methane heating offers benefits over heating compressor air from a heat exchanger size point of view. Finally, it was shown that heating natural gas offers significant benefits in terms of installation costs and power plant size. A summary of the outcome per criterion is presented in Table 7.4.

Table 7.4: Most favourable option per criterion.

Criterion	Compressor exhaust heating	Natural gas heating
Most beneficial location of energy addition	X	
Maximum transferable energy	X	
Ease of energy transfer to gas		X
Practical considerations		X

Based on these four criteria it has been decided to investigate curtailment utilization by means of heating Slochteren natural gas to approximately 160°C. Although two criteria were in favour of air heating and two in favour of Slochteren gas heating, the ease of implementation was crucial when it came to final decision.

Chapter 8

Energy Storage Design and Modelling

In chapter 6 it was concluded that thermal storage is to be used and more specifically, both latent and sensible heat storage. This chapter deals with the complete design and modelling of this storage system. It starts off by elaborating on the storage layout and PCM selection process. It continues by describing how the storage system is modelled and on what assumptions the model is based. This section is followed by a discussion on model accuracy, grid convergence, model verification and validation. Finally, the performance of the storage system is presented and the influence of module dimensions and PCM properties on performance is quantified and presented.

8.1 Storage Layout

The storage consists out of a number of identical modules. Therefore it is sufficient to design one module and to place these either in parallel to match the required capacity. The natural gas entering the combustion chamber is pressurized making a cylindrical module layout beneficial from a structural point of view. Based on this observation, the module layout as displayed in Figure 8.1 is chosen.

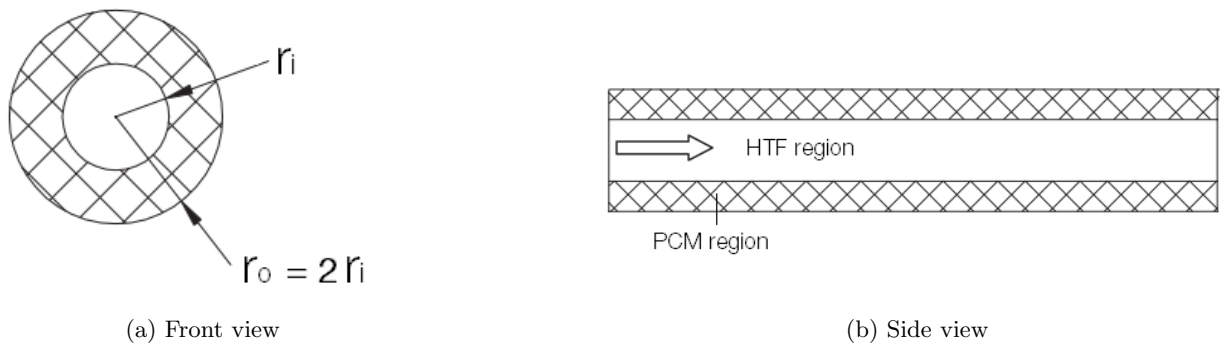


Figure 8.1: Schematic of the storage module. Modified from (87).

Each module consists out of a hollow cylinder where the natural gas is surrounded by the PCM. Within the cylinder, heat is exchanged between the PCM and the natural gas, also known as the heat transfer fluid (HTF). The HTF enters the cylinder at $z = 0$ at its initial temperature $T_{initial}$ and leaves the cylinder at $z = L$ at its heated temperature $T_{exhaust}$. If no cylinders are placed in series, this is also the temperature at which the gas enters the combustion chamber (transport losses neglected). To charge the storage, two heating elements are used. The elements consist of electrical wires making use of Joule heating to convert all electrical energy to heat. The heat storage has three separate modes: one charging mode, one discharging mode and a combination of both. During charging the outer heating element is used to heat the PCM when the plant is not in use and natural gas is stationary. During discharging, no heating element is active and heat is extracted from the storage. Finally, the storage can be charged and discharged simultaneously. When this happens, the inner heating elements are activated rather than the outer ones to directly heat the HTF rather than dissipating heat to the PCM. All three modes are displayed in Figure 8.2 to provide a better understanding of the heating elements and their modes of operation. The exact dimensions for the inner radius, outer radius and length are determined at a later stage by means of modelling a single storage module. These parameters depend on the heat transfer performance of the PCM in both phases and the obtainable exhaust temperature. Throughout the whole simulation, the outer radius r_o is twice the size of the inner radius r_i . The exact method of simulation is further explained in section 8.3.

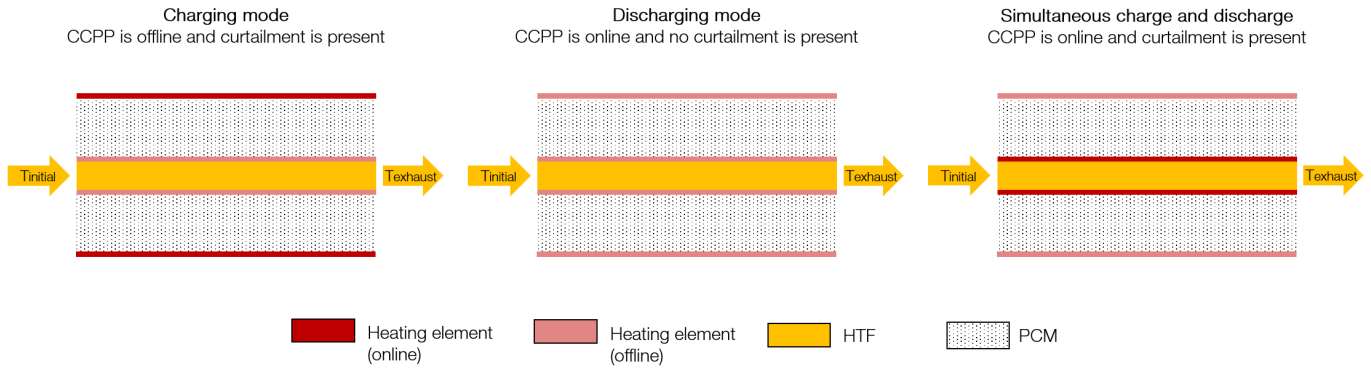


Figure 8.2: Cylindrical module cross-sectional cut-out schematic.

8.2 Phase Change Material Selection

The selection of a PCM is dependent on several material characteristics. These characteristics can be divided into three major categories: thermal, physical and chemical properties. Using this division, an overview of desirable PCM properties is provided in the upcoming paragraph (88; 89; 90). Note that these are not displayed in order of importance and that this list is not exclusive.

Thermal properties

- The PCM shall have a phase change temperature suitable for the required application to ensure that the energy release occurs when desired and to minimize heat losses to its surroundings.
- The PCM shall possess high latent heat of fusion. The latent heat of fusion is a measure of the heat release/absorption during a phase change. The higher the latent heat of fusion, the smaller the required amount of material to store the required quantity of thermal energy.
- The PCM shall possess a high specific heat to effectively charge and discharge sensible heat since the thermal storage does not solely operate in the melting region of the PCM.
- The PCM shall have high thermal conductivity in both the solid and liquid phase. This enhances heat transfer within the PCM to reduce internal temperature gradients.

Physical properties

- The PCM shall possess a high density to maintain a small storage volume.
- The PCM shall display a small volume change during phase transition to allow for simple heat exchanger designs.
- The PCM shall display little to no subcooling to ensure that the PCM melts and solidifies at the same temperature during its cycles.

Chemical properties

- The PCM shall melt and solidify completely to obtain homogeneous liquid and solid phases.
- The PCM shall display a reversible phase transition cycle with little to no hysteresis
- The PCM shall be chemically stable, inflammable and non-toxic.

Within the scope of this thesis, three of these requirements are used to evaluate a suitable PCM. These three requirements are the phase change temperature, latent heat of fusion and density. Unfortunately other parameters such as thermal conductivity could not be included in the trade-off due to limited available information on PCM properties for many materials. A list of suitable candidates is displayed in Table 8.1. Based on these three parameters, several PCMs show promise based on their phase change temperature. Since the goal is to preheat natural gas to approximately 160°C, the perfect PCM has a phase change temperature slightly above this temperature. If the phase change temperature is much higher, the heat losses to the ambient increase. Therefore, one should aim to stay as close to its desired gas temperature as possible. In addition, the ambient temperature in relatively hot environments must be accounted for. The phase change temperature cannot be below high ambient temperatures since this leads to undesired phase transitions. Since no ambient condition reaches a temperature of 160°C, this is not a problem for this application. The second selection criterion is the latent of heat fusion. It is beneficial to obtain a maximum latent heat of fusion to maximize the latent heat released and stored during operation. The final criterion is the PCMs density. A high density leads to a small required volume when a certain amount of PCM mass is required. By evaluating these three

criteria, it can be concluded that the PCM "A164" has the most suitable properties for the considered application. A164 is a commercial organic PCM solution produced by the company Phase Change Material Products Limited(91). Its material properties assumed for throughout the performed simulations are presented in Table 8.2.

Table 8.1: Phase changing material candidates.

Name	Phase change temperature [°C]	Latent heat of fusion [kJ/kg]	Density [kg/m ³]	Sources [-]
Salicylic acid	159	199	1443	(92)
Benzanilide	161	162	-	(92)
A164	164	306	1500	(59; 93; 94)
O-mannitol	166	294	1489	(92)
Hydroquinome	172	258	1358	(92)
Pentaerythritol	187	255	-	(59)
LiNO ₃ -NaNO ₃	195	252	-	(59)

Table 8.2: A164 material properties(91).

Parameter	Value	Unit
Melting temperature	164	[°C]
Density (liquid phase)	1500	[kg/m ³]
Density (solid phase)	1710	[kg/m ³]
Thermal conductivity (liquid phase)	0.53	[W/m K]
Thermal conductivity (solid phase)	1.09	[W/m K]
Specific heat (liquid phase)	1800	[J/kg K]
Specific heat (solid phase)	2400	[J/kg K]

8.3 Thermal Storage Modelling

This section explains the rationale and methods used for the transient numerical model to simulate the thermal performance of one single module. In the beginning of this section the assumptions made are outlined. The section continues by outlining which equations are used and discretized by means of the finite difference method (FDM). Once the underlying methods and equations are established, the model is extended by including the movement and heating of the HTF, the inclusion of the heat transfer coefficient and natural convection within the PCM during its liquid phase. Finally, the numerical model was tested for grid convergence, verified and validated.

8.3.1 Underlying Assumptions

The assumptions used during modelling can be classified into three categories: assumptions related to the general system, related to the heat transfer fluid and the phase changing material. These categories and their corresponding assumptions are as follows:

System

- Radiation heat transfer is negligible
- Heat losses to the ambient are negligible
- Internal heat generation is zero
- No wall is present between the PCM and HTF
- The system is axis-symmetric

Heat transfer fluid

- The heat transfer between HTF and PCM is controlled by convection
- The HTF's velocity and inlet temperature are constant
- The HTF's thermophysical properties are independent of temperature
- The HTF flow is fully developed within the cylinder
- The HTC is constant throughout the whole cylinder

Phase changing material

- The heat transfer within the PCM is controlled by conduction
- The PCM is assumed to have a definite melting point
- The PCM behaves ideally, i.e. supercooling and hysteresis are not accounted for
- The PCM is homogeneous and isotropic
- The PCM's thermophysical properties are different for solid and liquid phases but are independent of temperature
- The PCM's volume change during phase change is negligible

8.3.2 Governing Equations and the Finite Difference Method

As stated in the previous section, heat transfer within the PCM is mainly controlled by conduction and heat transfer to the HTF by convection. As a result, equations 8.3.1 and 8.3.2 are applicable to heat transfer within the PCM and to the HTF respectively(87). Equation 8.3.1 is referred to as the three-dimensional diffusion equation in cylindrical coordinates.

$$\rho C_p \frac{\partial T}{\partial t} = \frac{1}{r} \frac{\partial}{\partial r} \left(kr \frac{\partial T}{\partial r} \right) + \frac{1}{r^2} \frac{\partial}{\partial \phi} \left(k \frac{\partial T}{\partial \phi} \right) + \frac{\partial}{\partial z} \left(k \frac{\partial T}{\partial z} \right) \tag{8.3.1}$$

$$\frac{\partial T}{\partial t} = -\frac{2U}{\rho C_p r_i} (T_{HTF} - T_{surface}) \tag{8.3.2}$$

Based on the assumption that the problem is axis-symmetric, the three-dimensional diffusion equation can be simplified to a two-dimensional problem. By doing so, Equation 8.3.1 can be rewritten to:

$$\rho C_p \frac{\partial T}{\partial t} = \frac{1}{r} \frac{\partial}{\partial r} \left(kr \frac{\partial T}{\partial r} \right) + \frac{\partial}{\partial z} \left(k \frac{\partial T}{\partial z} \right) \tag{8.3.3}$$

$$\frac{\partial T}{\partial t} = \frac{\alpha}{r} \frac{\partial}{\partial r} \left(r \frac{\partial T}{\partial r} \right) + \alpha \frac{\partial}{\partial z} \left(\frac{\partial T}{\partial z} \right) \tag{8.3.4}$$

To solve this equation for each time step, the finite difference method is used. This technique replaces partial derivatives by suitable approximations on a finite difference grid. The grid consists of a number of nodes and for each of these nodes their temperature is computed at a certain time. To illustrate this, a generic grid is introduced in Figure 8.3 to show how a temperature field can be simulated by using a nodal network. This model is then used to size the module until the desired characteristics are obtained.

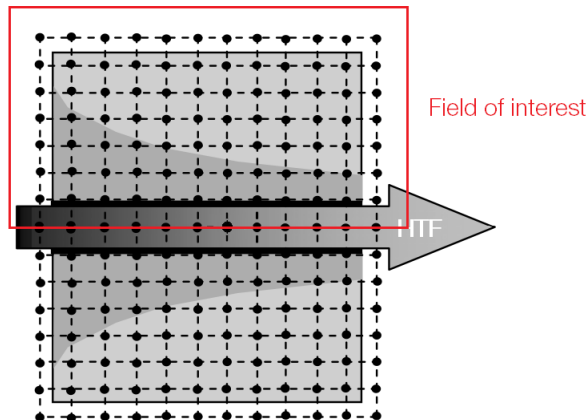


Figure 8.3: Generic mesh for PCM and HTF temperature field simulation in a hollow cylinder. Modified from (95).

Within the nodal network, ten different types of nodes can be distinguished. The type of node depends on its location within the grid. When a node is surrounded by four similar nodes it is referred to as an interior node. If this is not the case, it is called a boundary node or HTF node. Using Equation 8.3.4 and the finite difference method, the equation to compute the temperature at each node at a certain time step can be computed depending on its temperature at the previous time step and the temperature of its surroundings nodes. Since the storage module

is axis-symmetric, one can compute the complete solution by simulating half of the nodal network. Within this research, the temperatures for the top half of the network are computed as displayed by the field on interest in Figure 8.3.

The first step is to discretize the diffusion equation. To do so one must first be familiar with the Taylor series expansion. The Taylor series expansion of a function $u(x)$ around point x is as presented in Equation 8.3.5.

$$u(x) = \sum_{n=0}^{\infty} \frac{(x - x_i)^n}{n!} \left(\frac{\partial^n u}{\partial x^n} \right)_i \quad (8.3.5)$$

Using the Taylor series expansion, three finite difference approximations can be derived to approximate a partial derivative. These are the forward, backward and central difference approximations. Each of them involve a Taylor series expansion around point i and an isolation of the derivative term. The forward, backward and central difference derivations and approximations for first order derivatives are given in Equation 8.3.6 to Equation 8.3.12 respectively.

Forward difference

$$u_{i+1} = u_i + \Delta x \left(\frac{\partial u}{\partial x} \right)_i + \frac{(\Delta x)^2}{2} \left(\frac{\partial^2 u}{\partial x^2} \right)_i + \frac{(\Delta x)^3}{6} \left(\frac{\partial^3 u}{\partial x^3} \right)_i + \mathcal{O}(\Delta x)^3 \quad (8.3.6)$$

$$T_1 : \quad \left(\frac{\partial u}{\partial x} \right)_i = \frac{u_{i+1} - u_i}{\Delta x} - \frac{(\Delta x)}{2} \left(\frac{\partial^2 u}{\partial x^2} \right)_i - \frac{(\Delta x)^2}{6} \left(\frac{\partial^3 u}{\partial x^3} \right)_i + \mathcal{O}(\Delta x)^3 \quad (8.3.7)$$

$$T_1 : \quad \left(\frac{\partial u}{\partial x} \right)_i = \frac{u_{i+1} - u_i}{\Delta x} + \mathcal{O}(\Delta x) \quad (8.3.8)$$

Backward difference

$$u_{i-1} = u_i - \Delta x \left(\frac{\partial u}{\partial x} \right)_i + \frac{(\Delta x)^2}{2} \left(\frac{\partial^2 u}{\partial x^2} \right)_i - \frac{(\Delta x)^3}{6} \left(\frac{\partial^3 u}{\partial x^3} \right)_i + \mathcal{O}(\Delta x)^3 \quad (8.3.9)$$

$$T_2 : \quad \left(\frac{\partial u}{\partial x} \right)_i = \frac{u_i - u_{i-1}}{\Delta x} + \frac{(\Delta x)}{2} \left(\frac{\partial^2 u}{\partial x^2} \right)_i - \frac{(\Delta x)^2}{6} \left(\frac{\partial^3 u}{\partial x^3} \right)_i + \mathcal{O}(\Delta x)^3 \quad (8.3.10)$$

$$T_2 : \quad \left(\frac{\partial u}{\partial x} \right)_i = \frac{u_i - u_{i-1}}{\Delta x} + \mathcal{O}(\Delta x) \quad (8.3.11)$$

Central difference

$$T_1 - T_2 : \quad \left(\frac{\partial u}{\partial x} \right)_i = \frac{u_{i+1} - u_{i-1}}{2\Delta x} - \frac{(\Delta x)^2}{6} \left(\frac{\partial^3 u}{\partial x^3} \right)_i + \mathcal{O}(\Delta x)^3 \quad (8.3.12)$$

$$T_1 - T_2 : \quad \left(\frac{\partial u}{\partial x} \right)_i = \frac{u_{i+1} - u_{i-1}}{2\Delta x} + \mathcal{O}(\Delta x)^2 \quad (8.3.13)$$

For second order derivatives the central difference scheme becomes:

$$T_1 + T_2 : \quad \left(\frac{\partial^2 u}{\partial x^2} \right)_i = \frac{u_{i+1} - 2u_i + u_{i-1}}{(\Delta x)^2} + \mathcal{O}(\Delta x)^2 \quad (8.3.14)$$

Since the Taylor series can be expanded indefinitely, high order terms are displayed using the $\mathcal{O}(\Delta x)^n$ notation. Within the scope of this research, the derivatives are approximated by using Equation 8.3.8, Equation 8.3.11 or Equation 8.3.13. Therefore, there is an error term for each approximation containing all higher order terms from the Taylor series expansion. These terms are referred to as the truncation error. The truncation error is of the first order for the forward and backward difference schemes and second order for the central difference scheme. Due to this smaller truncation error, the central difference scheme is used to discretize in space. As it is not practical to discretize time with this scheme, the forward scheme is used to discretize in time. Therefore the discretization of the diffusion equation as shown in Equation 8.3.4 using the explicit scheme is said to be forward in time and central in space. Using this scheme the discretized diffusion equation can be used for nine out of ten different node types. To obtain these

equations the interior node equation was derived first and used as a baseline for boundary nodes. The boundary nodes equations are derived using the ghost node approach as explained later in this chapter.

Interior nodes

Using the forward difference scheme on the left side of Equation 8.3.4 leads to the following expression:

$$\left(\frac{\partial T}{\partial t}\right)_{i,j} = \frac{T_{i,j}^{t+1} - T_{i,j}^t}{\Delta t} \quad (8.3.15)$$

Using the central difference scheme on the right side of Equation 8.3.4 leads to the following expression:

$$\frac{\alpha}{r} \frac{\partial}{\partial r} \left(r \frac{\partial T}{\partial r} \right) + \alpha \frac{\partial}{\partial z} \left(\frac{\partial T}{\partial z} \right) = \frac{\alpha}{r_i \Delta r^2} (r_{i+\frac{1}{2}} T_{i-1,j}^t - 2r_i T_{i,j}^t + r_{i-\frac{1}{2}} T_{i+1,j}^t) + \frac{\alpha}{\Delta z^2} (T_{i,j+1}^t - 2T_{i,j}^t + T_{i,j-1}^t) \quad (8.3.16)$$

Where α represents the thermal diffusivity which can be computed via Equation 8.3.17.

$$\alpha = \frac{k}{\rho C_p} \quad (8.3.17)$$

Combining both sides and rewriting the equation for $T_{i,j}^{t+1}$ leads to the following expression for the temperature at the proceeding time step for interior nodes such as node five displayed in Figure 8.4a.

$$T_5^{t+1} = \left[\frac{\alpha}{r_i \Delta r^2} (r_{i+\frac{1}{2}} T_2^t - 2r_i T_5^t + r_{i-\frac{1}{2}} T_8^t) + \frac{\alpha}{\Delta z^2} (T_6^t - 2T_5^t + T_4^t) \right] \Delta t + T_5^t \quad (8.3.18)$$

When the explicit scheme is used to derive these expressions a limit is imposed on the maximum time step which can be used to ensure stability of the computation. That is, so the error present at one time step do not magnify as the computation continues. For cylindrical coordinates, the Neumann stability criterion can be expressed as displayed in Equation 8.3.19(96).

$$\Delta t_{max} = \frac{1}{2 \frac{\alpha}{\Delta r^2} + \frac{\alpha}{\Delta z^2}} \quad (8.3.19)$$

Boundary nodes

As briefly mentioned, the expressions for the boundary nodes require a slightly different approach. A ghost node is created to simulate the conditions of an interior node. The boundary condition(s) acting on the boundary node are used to derive an expression for one of the four surrounding nodes. This expression is then substituted in the interior node equation to obtain the boundary node expression. The active boundary conditions are as follows:

at $r = r_o$

$$k \frac{\partial T}{\partial r} = 0 \quad (8.3.20)$$

at $r = r_i$

$$-k \frac{\partial T}{\partial r} = U(T_{surface} - T_\infty) \quad (8.3.21)$$

at $z = 0$ and $z = L$

$$k \frac{\partial T}{\partial z} = 0 \quad (8.3.22)$$

To demonstrate this method, the expression for the middle left boundary node displayed in Figure 8.4b which is subjected to insulation in the z direction, is derived. The same procedure can be applied to all other corner nodes using the above stated boundary conditions. For this node one ghost node is created since a boundary condition is active. This is the result of its insulated boundary and can be expressed as follows:

$$k \frac{\partial T}{\partial z} = 0 \quad (8.3.23)$$

Using the finite difference method the expressions as shown in Equation 8.3.23 are obtained in terms of the grid and ghost nodes. The results are displayed in Equation 8.3.24. From this equation it follows that $T_5^t = T_{-5}^t$. Using the expression for the interior nodes and substituting this node temperature into this expression yields Equation 8.3.25:

$$k \frac{\partial T}{\partial z} = k \frac{(T_5^t - T_{-5}^t)}{2\Delta z} = 0 \quad (8.3.24)$$

$$T_4^{t+1} = \left[\frac{\alpha}{r_1 \Delta r^2} (r_{1+\frac{1}{2}} T_1^t - 2r_i T_4^t + r_{1-\frac{1}{2}} T_7^t) + \frac{2\alpha}{\Delta z^2} (T_5^t - T_4^t) \right] \Delta t + T_4^t \quad (8.3.25)$$



Figure 8.4: Interior and left boundary nodes.

8.3.3 Enthalpy method

As the PCM undergoes a phase change during charge and discharge one can not directly compute the new temperature as done previously. The derived equations still hold but the temperature has to be computed via the PCM's enthalpy to account for the latent heat of fusion(95). Doing so is called the enthalpy method. Several other methods are known such as the heat capacity method(95). However, the enthalpy method is considered to be the most efficient when using a fixed-grid(97). It uses that the enthalpy is a temperature-dependent variable and computes the latent heat flow through enthalpy of the PCM. To account for this in the FDM scheme, the previous equations must be rewritten to include the enthalpy at the relevant point rather than temperature. For the interior nodes, the expression then becomes as displayed in Equation 8.3.26. Using the ghost node approach as explained earlier, the same expressions can be derived for each of the boundary nodes.

$$h_{i,j}^{t+1} = \left[\frac{k}{r_i \Delta r^2} (r_{i+\frac{1}{2}} T_{i-1,j}^t - 2r_i T_{i,i}^t + r_{i-\frac{1}{2}} T_{i+1,i}^t) + \frac{k}{\Delta z^2} (T_{i,j+1}^t - 2T_{i,j}^t + T_{i,j-1}^t) \right] \frac{\Delta t}{\rho_{i,j}^t} + h_{i,j}^t \quad (8.3.26)$$

The new enthalpy at a time $t+1$ can be related to a temperature by means of the temperature-enthalpy relation given by the following expressions. In these expressions, C_p represents the specific heat, h_{sl} represents the latent heat of fusion and T_m the melting temperature of the PCM.

$$h(T) = \begin{cases} C_{p,solid} (T - T_m) & \text{for } T < T_m \\ C_{p,solid} T_m + h_{sl} & \text{for } T = T_m \\ C_{p,liquid} (T - T_m) + h_{sl} & \text{for } T > T_m \end{cases} \quad (8.3.27)$$

8.3.4 Heat Transfer Fluid Heating and Movement

Heat transfer to the HTF is governed by Equation 8.3.2. Using the same finite difference method as used for interior nodes, this expression can be rewritten to Equation 8.3.28.

$$T^{t+1} = -\frac{2U\Delta t}{\rho C_p r_i} (T^t - T_{surface}^t) + T^t \quad (8.3.28)$$

To simulate the movement of the HTF at each specific time step, the value of temperature of each node is transferred to its neighbouring node after each iteration. This is allowed since forced rather than natural convection is present(95). To make sure that one time step corresponds to the distance Δz travelled by a gas particle it is expressed as shown in Equation 8.3.29.

$$\Delta t = \frac{\rho \pi r_i^2 \Delta z}{\dot{m}} \quad (8.3.29)$$

This is the value for time step which must be used throughout the simulation. If this value exceeds that determined by the Neumann stability criterion the simulation can not be performed successfully due to stability issues.

8.3.5 Heat Transfer Coefficient

Convection is simulated by means of the heat transfer coefficient. The approach used is based on the Reynolds number, Prandtl number and Nusselt number as explained in chapter 7(98). First, the Reynolds number is computed using Equation 8.3.30 and based on its value, one can determine whether the flow is turbulent or laminar.

$$Re_{d_i} = \frac{\rho V d_i}{\mu} \quad (8.3.30)$$

$$Pr = \frac{\mu C_p}{k} \quad (8.3.31)$$

For Reynolds numbers smaller than 2300 the flow is considered to be laminar(98). For Reynolds numbers exceeding 10,000 the flow can be considered to be turbulent(98). All intermediate values indicate that the flow is transitioning from laminar to turbulent. Once the flow condition is known, the Prandtl number is computed by using Equation 8.3.31 and used in either the laminar or turbulent equation for the Nusselt number as shown in Equation 8.3.32 and Equation 8.3.33 respectively(98; 79).

$$Nu_{laminar} = 3.66 + \frac{0.65 Re_{d_i} Pr \frac{d_i}{L}}{1 + 0.04 (Re_{d_i} Pr \frac{d_i}{L})^{(\frac{2}{3})}} \quad (8.3.32)$$

$$Nu_{turbulent} = \frac{(\zeta/8) Re_{d_i} Pr}{1 + 12.7 \sqrt{\zeta/8} (Pr^{\frac{2}{3}} - 1)} \left[1 + (d_i/L)^{\frac{2}{3}} \right] \quad (8.3.33)$$

Where:

$$\zeta = (1.8 \log_{10} Re_{d_i} - 1.5)^{-2} \quad (8.3.34)$$

Equation 8.3.33, known as the Gnielinski correlation, does come with certain restrictions. For this relation to be valid, the Prandtl number must be larger than 0.1 but smaller than 1000 and the Reynolds number must be larger than 10,000 but smaller than 1,000,000(98). Finally, the heat transfer coefficient can be computed from the Nusselt number by means of Equation 8.3.35. In reality the HTC is a variable due to the change in pressure, density and velocity when a gas is heated. To give an indication of the density change with temperature, this trend is illustrated for methane in Appendix A, Figure A.7.

$$U = \frac{Nu k}{d_i} \quad (8.3.35)$$

8.3.6 Natural Convection in the PCM

When a part of the PCM is in liquid phase and a temperature difference is applied over the PCM's enclosure, natural convection might occur. For this simulation this effect has not been taken into account due to a lack of accurate information on the PCM's properties to successfully compute the Rayleigh number. However, to account for this effect the thermal conductivity of the PCM in its liquid phase can be corrected to obtain an effective thermal conductivity(99; 96; 100). For hollow cylinders, this correction is as follows(100).

$$k_{eff} = \left[0.386 \left(\frac{Pr}{0.861 + Pr} \right)^{\frac{1}{4}} (F_{cyl} Ra_L)^{\frac{1}{4}} \right] k_{liquid} \quad (8.3.36)$$

Where:

$$F_{cyl} = \frac{\ln\left(\frac{r_e}{r_i}\right)^4}{L^3\left(r_i^{-\frac{3}{5}} + r_o^{-\frac{3}{5}}\right)^5} \quad (8.3.37)$$

$$Ra_L = \frac{g\beta(T_1 - T_2)L^3}{\nu\alpha} Pr \quad (8.3.38)$$

Alternatively, the effective thermal conductivity can be expressed as a function of the thermal conductivity in liquid phase times the Nusselt number of the fluid within the enclosure(99; 96; 101). The Nusselt number can then be segmented into a constant and the Rayleigh number as shown in Equation 8.3.39. Based on experimental results, the constants C_L and n equal 0.099 and 0.25 respectively for cylindrical geometries(101).

$$k_{eff} = k_{liquid} Nu = k_{liquid} C_L Ra_L^n \quad (8.3.39)$$

8.3.7 Impact of Wall Presence

Within this model, no wall is present between the PCM and HTF. To identify the effects of this simplification, the effect of the walls thermal resistance on the total resistance is quantified. The total thermal resistance consists of three elements: conduction through the PCM, conduction through the wall and convection between the wall and HTF. This can be described in terms of thermal resistances as follows(102):

$$R_{total} = R_{conduction,wall} + R_{conduction,PCM} + R_{convection,HTF} \quad (8.3.40)$$

$$R_{total} = \frac{\ln(r_{wall}/r_i)}{(2\pi L)k_{wall}} + \frac{\ln(r_o/r_{wall})}{(2\pi L)k_{PCM}} + \frac{1}{(2\pi r_i L)U} \quad (8.3.41)$$

Using Equation 8.3.41, the total resistance can be computed together with the fraction each element contributes to the total resistance. For this analysis the parameters as displayed in Table 8.3 were taken into account. Using these settings, the total contribution of $R_{conduction,wall}$ to the total resistance is computed to 0.17%. By doubling the wall thickness to 0.02 meter leads to double the percentage of 0.34%. This indicates that absence of a separation wall has little influence on the final results for various wall thicknesses.

Table 8.3: Simulation parameters.

Parameter	Value	Unit
Phase change material		
Thickness	0.05	[m]
Thermal conductivity (liquid phase)	0.53	[W/m K]
Wall		
Thickness	0.01	[m]
Thermal conductivity (iron)	80.13	[W/m K]
Heat transfer fluid		
Thickness	0.05	[m]
Heat transfer coefficient	100	[W/(m ² K)]
General module parameter		
Inner radius (r_i)	0.05	[m]
Wall radius (r_{wall})	0.06	[m]
Outer radius (r_o)	0.11	[m]
Length	20	[m]

8.4 Numerical Errors

The numerical error consists of two major sources. The first is the discretization error coming from the truncation error as previously touched upon. The second is the round-off error coming from the limited number of digits used by the computational program (in this case MATLAB).

Discretization error

As a result of the Taylor series expansion, an error is created since not all terms coming from the Taylor series expansion were incorporated into the expression for the derivative. This truncation error is found to be proportional to Δt for the forward in time discretization and $(\Delta x)^2$ for the central in space scheme. Applying this knowledge to the case in question using cylindrical coordinates, the following local error is quantified as shown in Equation 8.4.1. This is the maximum error induced at a single time step due to the discretization process. As expected, smaller time and grid steps lead to a more accurate approximation of the original differential equation.

$$\text{Local error} = \mathcal{O}(\Delta t) + \mathcal{O}(\Delta r)^2 + \mathcal{O}(\Delta z)^2 \quad (8.4.1)$$

The total error after i time steps during a time period t_0 is referred to as the global discretization error. Using the local discretization error for each time step and the performed number of time steps during period t_0 , the global error can be computed as follows:

$$\text{Global error} = (t_0/\Delta t) \left(\mathcal{O}(\Delta t) + \mathcal{O}(\Delta r)^2 + \mathcal{O}(\Delta z)^2 \right) \quad (8.4.2)$$

Round-off error

The round-off error is caused by the fact that a computer can only hold a limited amount of digits during calculations. MATLAB by default uses double precision which allows the user to perform calculations with 15 significant digits instead of the seven used in single precision. If the number of digits is exceeded, the number is rounded and thereby an error is introduced. It is therefore that the round-off error increases when the time and grid step sizes reach smaller numbers with more significant digits. For the discretization error the opposite is true, the finer the time and grid step sizes the smaller the discretization error.

8.5 Grid Convergence

To obtain a solution independent of the grid density, different grid sizes were tested until the grid density did not have a significant influence on the final solution. For this test, the initial temperature of the PCM was set to be 166°C and that of the HTF to 15°C. The simulated time period was set to 100,000 seconds. For the different grid densities, the HTF exhaust temperature is plotted in Figure 8.5 for the simulation duration. All cases were evaluated for a length of 20 meter, an inner radius of 0.05 meter and a mass flow of 0.007 kg/s. It can be observed that the temperature profiles converge when the grid density increases (larger number of nodes in r and z-direction). The grid density at which convergence takes place is dependent on the module's dimensions and mass flow. In addition, the time step used for each simulation differs due to the HTF flow movement simulation method. It can be concluded that the solution converged at a grid size of 101x21 since its temperature profile does not differ significantly from the 161x61 grid temperature profile. To quantify the deviation acquired of simulating with a 101x21 density instead of 161x61, the final temperature after 100,000 seconds is used as a metric. For this temperature a deviation of 0.02% was found. This deviation is deemed as acceptable and further computations are to be performed with a 101x21 grid density. It must be noted that the grid can be refined further. However, this greatly increased the computational time since a higher number of nodes needs to be evaluated and the simulation time step decreases for more nodes in the z-direction. When storage module dimensions change a new grid convergence study must be performed due to coupling between grid density and time step.

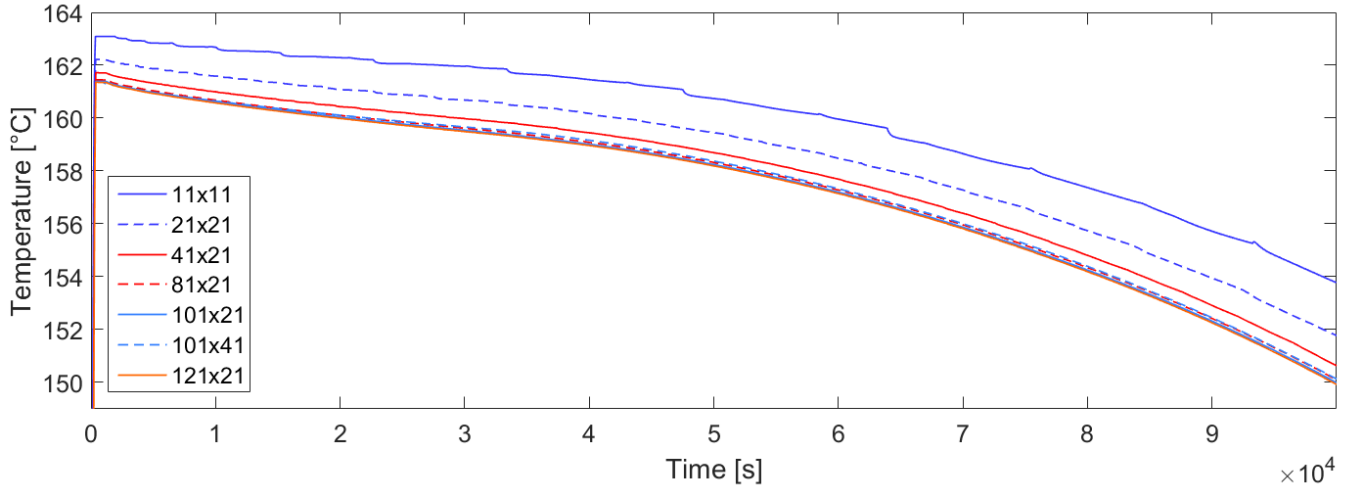


Figure 8.5: Influence of grid density on the heat transfer fluid exhaust temperature profile (number of nodes in r-direction times number of nodes in z-direction).

8.6 Verification and Validation

As verification of the model, the energy balance at each time step is computed. If the model is programmed correctly the energy gained by the HTF should equal the energy lost in the PCM at all times. In addition, these two quantities of energy also have to equal the energy passing through the boundary between HTF and PCM. In mathematical terms, this can be represented as documented in Equation 8.6.1 to Equation 8.6.3.

$$\Delta E_{HTF} = \rho C_p \pi r_i^2 \Delta z \int_0^t \sum_{j=1}^M (T_{HTF}^{t+1} - T_{HTF}^t) dt \quad (8.6.1)$$

$$\Delta E_{Boundary} = 2\pi r_i \Delta z \int_0^t \sum_{j=1}^M U (T_{surface}^t - T_{HTF}^t) dt \quad (8.6.2)$$

$$\Delta E_{PCM} = \rho \Delta z \pi (r_a^2 - r_b^2) \int_0^t \sum_{i=1}^N \sum_{j=1}^M (h_{i,j}^{t+1} - h_{i,j}^t) dt \quad (8.6.3)$$

Where r_a and r_b are the upper and lower r-coordinates for the particular PCM node control volume element. As a criterion, the energy balance deviation between each of the three energy terms can not differ more than 1% from one another during each time step and over the total time period(101; 103). This discrepancy comes from the non-linearity of Equation 8.3.1 and its coupling with Equation 8.3.2 at the boundary conditions. For a simulation period of 100,000 seconds at a grid density of 101x21, the maximum absolute deviation was found to be 0.045%. This illustrates that the model functions properly with regards to the energy balances.

To validate the model, a specific case simulation is performed and its correspondence with literature is evaluated. For this purpose two articles are used as reference material which modelled a shell-and-tube thermal heat storage module(87; 104). One single storage module is simulated when it is heated by a HTF with a higher temperature than the PCM which starts in its solid state. The exact details of the simulation are displayed in Table 8.4. The only difference between both simulations was the used time step. In literature a time step of 2.00 seconds was used whereas a time step of 0.001 seconds was computed from the HTF movement coupling. After performing this simulation, the HTF exhaust temperature is visualized and compared to the results found in literature as presented in Figure 8.6. Since the results from both articles are similar they are visualised using the same trend line. It can be observed that both temperature profiles are well in accordance with one another. This implies that the developed model is reliable and gives results which are in agreement with other models.

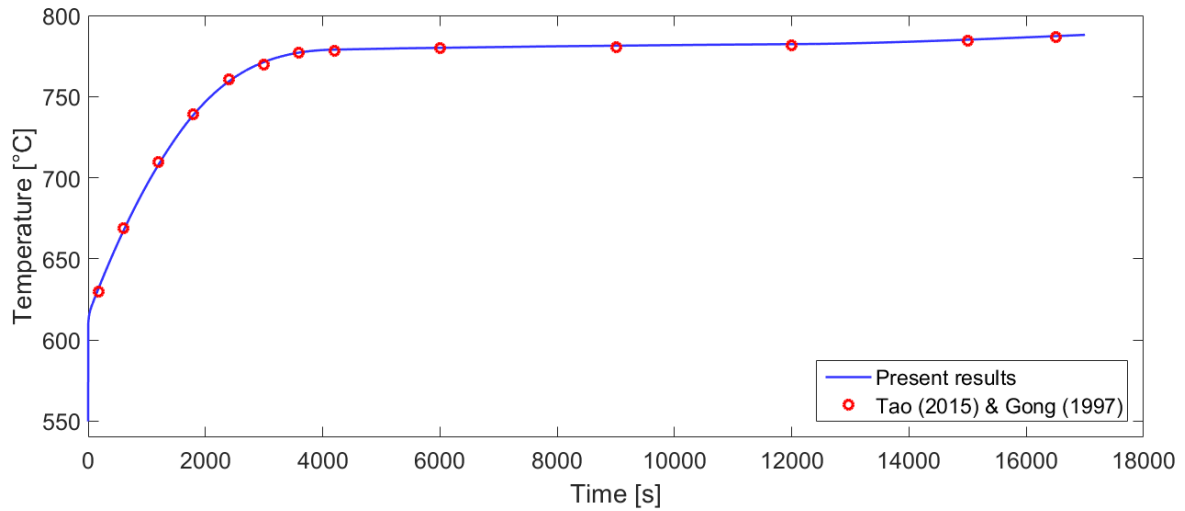


Figure 8.6: Heat transfer fluid exhaust temperature as a function of time. The results are compared to similar simulations(87; 104).

Table 8.4: Simulation parameters(104).

Parameter	Value	Unit
General		
Length	1.5	[m]
Inner radius	12.5	[mm]
Outer radius	25.0	[mm]
Simulation time	17,000	[s]
Phase change material		
Initial temperature	550	[°C]
Melting temperature	767	[°C]
Latent heat of fusion	816	[kJ/kg]
Density	2390	[kg/m ³]
Heat capacity	1770	[J/kg K]
Thermal conductivity (solid phase)	3.8	[W/m K]
Thermal conductivity (liquid phase)	1.7	[W/m K]
Heat transfer fluid		
Initial temperature	550	[°C]
Hot gas temperature	817	[°C]
Velocity	15	[m/s]
Density	1.862	[kg/m ³]
Heat capacity	502.2	[J/kg K]
Thermal conductivity	0.133	[W/m K]
Prandtl number	0.24	[-]
Heat transfer coefficient	89.16	[-]

8.7 Results

For the converged grid density with a length of 20 meter, an inner radius of 0.05 meter and a mass flow of 0.007 kg/s a transient numerical simulation is performed. The used time step equals $\Delta t = 3.9484$ seconds. From this analysis it becomes clear at which locations and at which rate heat is transferred to the HTF. These results are presented in the first part of this section. The second and third part deal with how the module dimensions and PCM properties affect these results.

For this particular simulation, the PCM is at an initial temperature of 166°C and the HTF temperature 15°C. The results for a simulation period of 100,000 seconds are presented in Figure 8.7 at various times. As expected, the temperature of the PCM drops more rapidly at the location where the HTF enters than where it exists. The same is true for the PCM closer to r_i due to the colder inner radius. It can be seen that the temperature drop of the PCM

is delayed at 164°C since this corresponds to the melting temperature of the PCM. At this temperature heat is still transferred from the PCM to the HTF but no temperature drop occurs until all latent heat of fusion is extracted. Once this occurs, the PCM temperature drops until it would reach the HTF inlet temperature of 15°C . It is this combination of heat transfer mechanics which classifies this storage as both a sensible and latent heat storage.

When observing the exhaust temperature profile visualised in Figure 8.8a three major sections can be identified within this curve. The first section covers a short time span and has a constant temperature. During this period, the PCM's temperature is high enough to keep exhaust temperature constant although the PCM is cooling down. The reason that the maximum exhaust temperature (T_{max}) is not reached can be attributed to the cylinder's length, it is not long enough to get the gas to equal the T_{max} of the PCM (see Figure 8.8b). In the second section, the PCM is partially below its melting temperature leading to a convex HTF temperature profile. The PCM's temperature near r_o is still equal to its melting temperature. The third section of the curve occurs when the PCM's temperature near r_o also dropped below the melting temperature. At locations close to $z = 0$ the temperature of all nodes in the r-direction decreases leading to a concave HTF temperature profile.

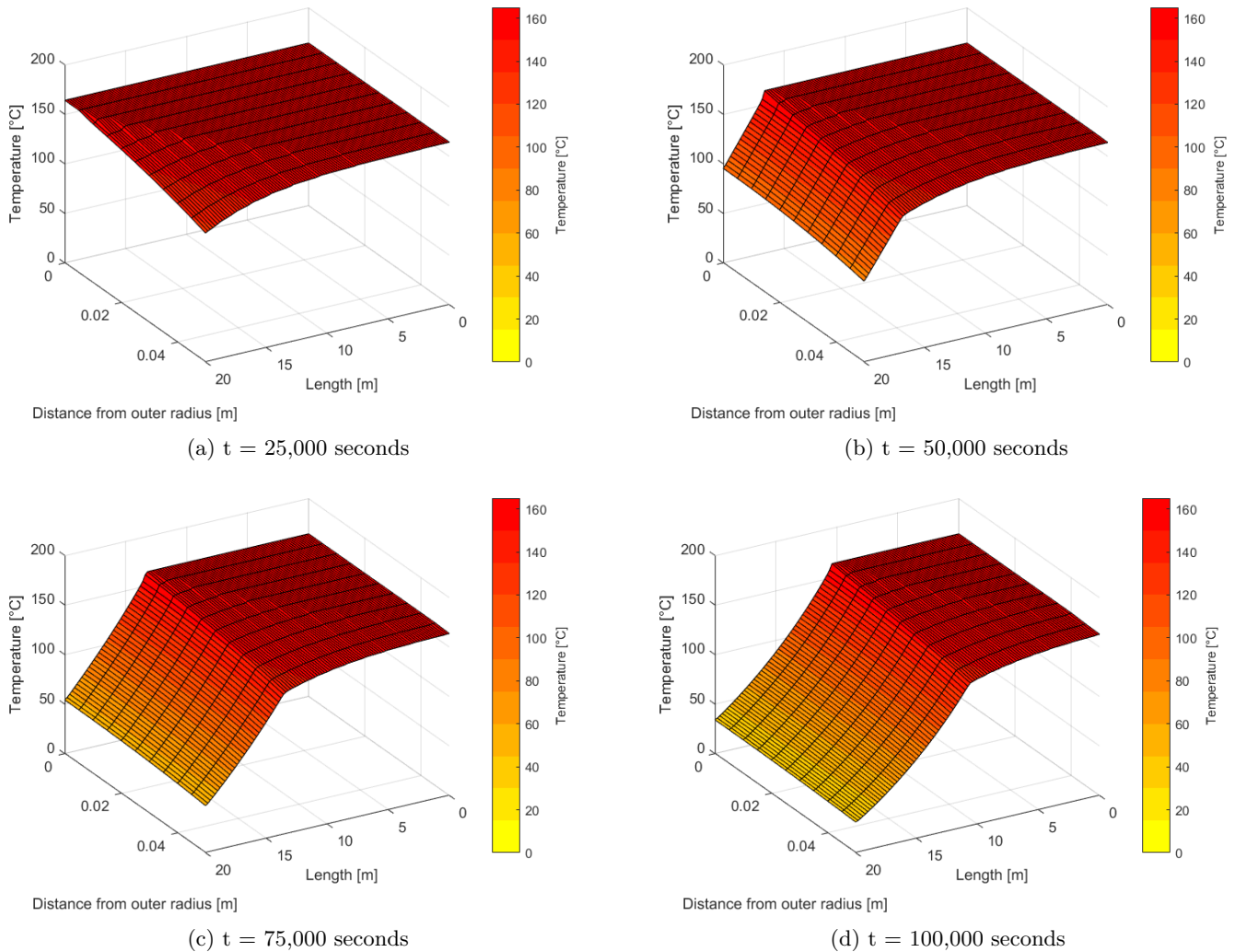


Figure 8.7: Numerical simulation results for the heat transfer fluid heating for one storage module.

8.8 Sensitivity Study

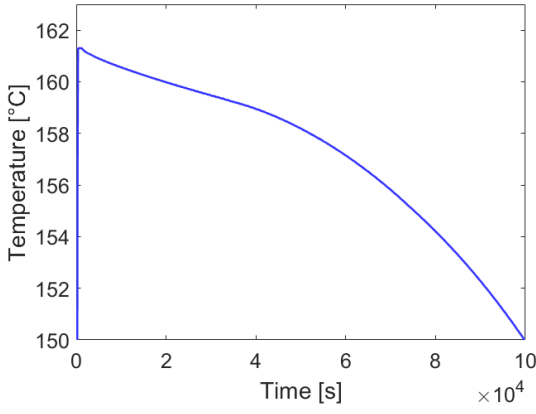
To evaluate the effect the module dimensions have on storage performance several parameters sweeps are performed. Swept parameters include the cylinder length, inner radius and the ratio r_o/r_i . For each parameter, three different values were simulated to reveal the impact they have on the HTF temperature exhaust profile. To reveal the effects of different PCM properties simulations were performed for various different specific heat capacities and thermal conductivities. Once again three different values were selected for each parameter.

8.8.1 Effect of Module Dimensions

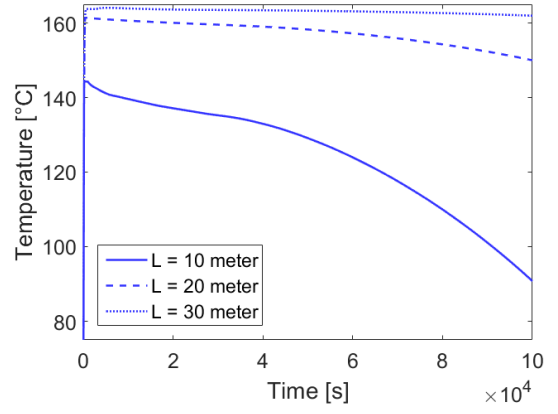
The results are presented in Figure 8.8b to Figure 8.8d. From these figures it can be observed that a longer cylinder length leads to a higher T_{max} and that the decay in temperature is delayed compared to smaller lengths. Both phenomena occur since more PCM mass is present at larger cylinder lengths. As a result, high temperatures within the PCM can be sustained for a longer period of time. The trend for the inner radius shows that a larger inner, and therefore a larger outer radius, leads to a lower T_{max} and a longer required time to achieve T_{max} . The reason for this behaviour is related to the flow velocity. Increasing the radius leads to a lower flow velocity which decreases the Reynolds number, Nusselt number and heat transfer coefficient. It turns out that increasing the inner radius decreases the energy exchange between the PCM and HTF per unit time, leading to the longer required time period to achieve T_{max} . However, a more stable temperature profile is obtained. Solidification takes place at a later stage allowing the $T_{exhaust}$ to remain high for a longer duration of time. If the radii doubles, the amount of PCM quadruples leading to a more constant temperature profile resulting from heat conduction within the PCM. Finally, Figure 8.8d indicates that changing the ratio r_o/r_i leads to significant differences in temperature profiles after approximately 33,000 seconds. For larger ratio's a higher temperature can be maintained for a longer period of time due to its larger PCM volume. The difference between ratios only becomes significant at a later stage when the solidification front reaches r_o . However, if the PCM's thermal conductivity would be increased the effect is expected to arise at an earlier point in time.

8.8.2 Effect of PCM properties

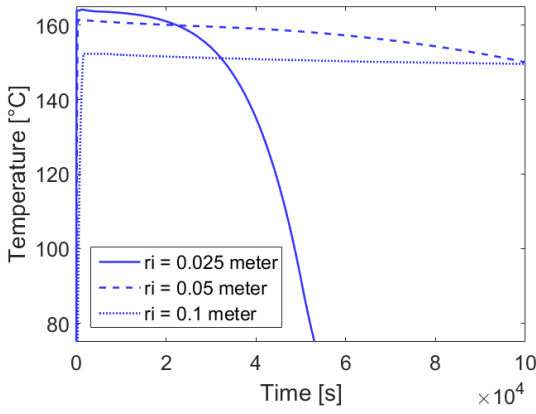
The results are presented in Figure 8.8e to Figure 8.8h. Figure 8.8e deals with the thermal conductivity during the liquid phase. For higher thermal conductivities the achievable T_{max} increases and the overall HTF pattern reaches higher temperatures. The reason for these phenomena is that for higher conductivities a higher temperature can be obtained at r_i for a longer time, leading to higher exhaust temperatures. For the thermal conductivity during the solid phase the same holds as is visible in Figure 8.8f. However, no higher T_{max} is achieved. This can easily be explained since T_{max} is reached when the PCM near r_i is in its liquid phase and therefore the solid thermal conductivity has no effect on T_{max} . Using Figure 8.8g one can observe that for higher values of the specific heat capacity during the liquid phase, the HTF maintains a higher temperature throughout the whole simulation. This behaviour is expected since more energy is dissipated towards the HTF while maintaining a high PCM temperature for large specific heats. The same trend is visible for the specific heat capacity at solid phase in Figure 8.8h. This trend starts at a later point in time since this simulation began with a fully liquid PCM. This trend becomes more evident as a larger portion of the PCM solidifies.



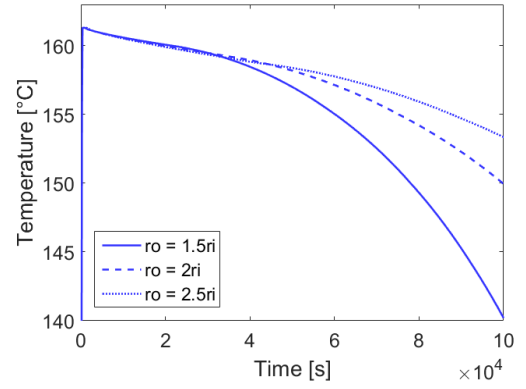
(a) Baseline case



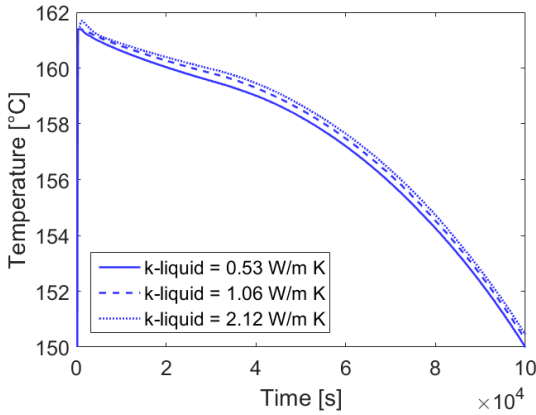
(b) Cylinder length



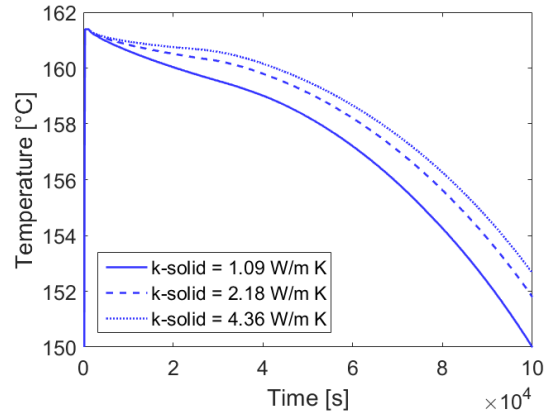
(c) Cylinder radii ($r_o = 2r_i$)



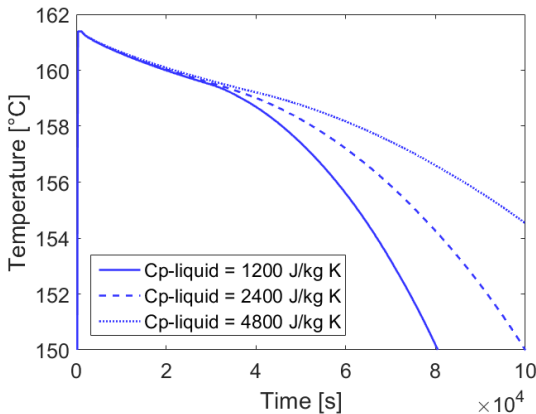
(d) Radii ratio



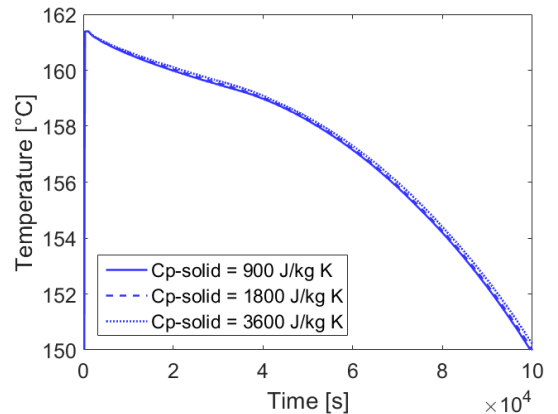
(e) Thermal conductivity - liquid phase



(f) Thermal conductivity - solid phase



(g) Specific heat capacity - liquid phase



(h) Specific heat capacity - solid phase

Figure 8.8: Effects of module dimensions and PCM properties on HTF exhaust profile.

8.9 Conclusions and Observations

Within this chapter a thermal storage system has been designed which makes use of both sensible and latent heat storage. The complete storage consists out of multiple modules installed in parallel. A single module consists of a hollow insulated cylinder with the HTF flowing internally. The cylinder is filled a PCM which acts as the main energy storage medium. Each module contains two heating elements, one at the inner radius and one at the outer radius. This allows for the storage to be charged and discharged in three different modes. The activation of each modes depends on the presence of curtailment and the operating status of the CCPP. According to three independent requirement categories several PCMs have been evaluated based on their phase change temperature, latent heat of fusion and density. After this analysis, the organic PCM A164 has been chosen as a suitable candidate.

To accurately model the performance of one storage model a cross-section of the cylinder was discretized by means of a series of nodes. To model heat transfer within the PCM and HTF their respective heat transfer equations were discretized by means of the FDM. An explicit scheme forward in time and central in space was used to minimize numerical errors while keeping the modelling approach fairly simple. Using this scheme, the equations for both types of nodes, interior and boundary, were derived. To model convection taking place at the inner section of the tube, the HTC was computed by means of the HTF's flow characteristics. With the FDM discretization method comes a certain numerical error which has been elaborated upon together with round-off errors. To show that the result is independent of the grid density, a convergence study was performed which shows that accurate results are obtained for a grid density of 101×21 for $L = 20$ meter, $r_i = 0.05$ meter and $\dot{m} = 0.007$ kg/s. The model has been verified by means of an energy balance at three separate locations at every time step for a time period of 100,000 seconds. These three locations were the PCM, HTF and the boundary between the PCM and HTF. At each point in time, the energy imbalance was found to be below 1%. Validation of the model was performed by conducting a case simulation and by comparing its results to literature. For the specific simulation case in question the results were almost identical to literature.

The numerical model has been used to evaluate the impact of seven different parameters: module length, inner radius, radii ratio, thermal conductivity of the PCM (both for liquid and solid phase) and the specific heat capacity of the PCM (both for liquid and solid phase). The results gave insights on how these parameters change the HTF exhaust temperature pattern which can be used for optimization of the storage module. In conclusion, a numerical model which can simulate a thermal storage has successfully been developed.

Chapter 9

Annual Performance

In this chapter the curtailment model, CCPP model and thermal storage model are combined to assess the annual impact of curtailment utilization on natural gas consumption. A quick overview is given on the used models and their relation to one another. This is followed by the results of the complete curtailment utilization system with and without the use of thermal storage.

9.1 Methodology

Model integration is executed as documented in the N2 chart shown in Figure 9.1. The annual curtailment pattern together with the annual operating pattern of the power plant are used to perform a simulation for $T_{exhaust}$ using the thermal storage model. The curtailment pattern determines when the storage is charged and the plant operating pattern determines when it is discharged. This simulation is performed throughout a complete year on the converged grid density to acquire accurate results. The time step of this simulation is determined by the gas velocity and step size in the z-direction as explained in chapter 8. The output of the energy storage model is an annual pattern for the natural gas temperature which enters the power plant. Using this pattern and the simulated performance curves, as presented in chapter 5, the annual fuel consumption can be computed. The outcome is compared to the annual fuel consumption without curtailment utilization which was obtained in chapter 5. It must be noted that this approach does not take into account a certain storage operation strategy. All modules perform identically representing a full load scenario. Therefore it is possible that the thermal storage can be used for a longer period of time since the CCPP does not constantly run at full load.

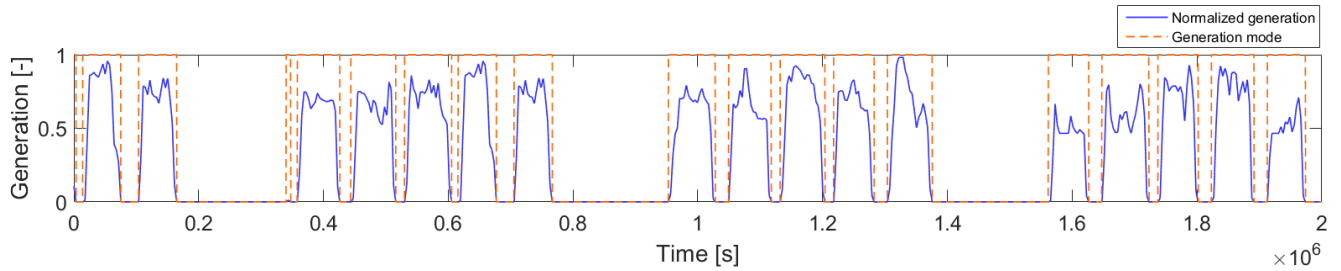
Inputs	<ul style="list-style-type: none"> • SNSP limit • RR limit • Annual demand pattern • Annual wind generation pattern 	<ul style="list-style-type: none"> • Component data • Annual operating pattern 	<ul style="list-style-type: none"> • Annual operating pattern • PCM properties • HTF properties • Storage module dimensions 	
	Curtailment model		<ul style="list-style-type: none"> • Annual curtailment pattern 	
		Combined-cycle model		<ul style="list-style-type: none"> • Annual performance summary (no curtailment utilization)
			Thermal storage model	<ul style="list-style-type: none"> • Annual fuel temperature pattern (curtailment utilization)
				Outputs

Figure 9.1: Model integration N2 chart.

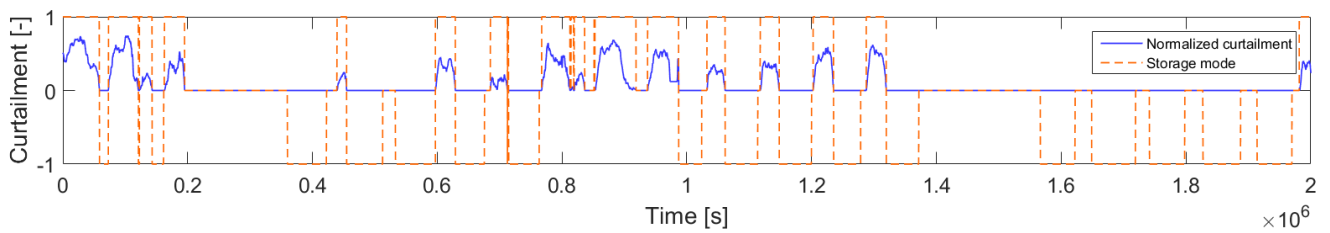
This process is visualized in Figure 9.2. Figure 9.2a displays the power plants operating pattern and with its corresponding mode. Its mode takes a value of 1 when the plant is online and a 0 when it is offline. Figure 9.2b displays the curtailment pattern coming from the curtailment model. Its corresponding storage mode takes a value 1 when the storage is charging, a 0 when its stationary (no charge or discharge) and a -1 when it is discharging. During charging, depending on the plant mode, a complete row of nodes is set to 165°C to simulate the heating elements. These two mode patterns are used as inputs for the energy storage model to obtain the natural gas temperature pattern as shown in Figure 9.2c. Whenever there is more curtailment than needed to heat the HTF to 160°C the storage is being charged. When the storage mode equals 0 the gas is stationary and the HTF slowly heats up since no cold gas enters the pipe. During a long discharge period the PCM’s temperature drops below its melting temperature and the exhaust temperature decreases until it reaches 15°C or until the storage mode changes to 0 or 1. This pattern is used to compute the total energy added to the fuel on an annual basis. For this purpose Equation 7.1.2 is used once again. The annual fuel consumption saving percentage is calculated using Equation 9.1.1. It relates the total energy added to the gas to the total energy added to the combined-cycle system. By doing so, the impact of the storage can easily

be accessed and the total annual fuel savings can be quantified by means of Figure 9.2c.

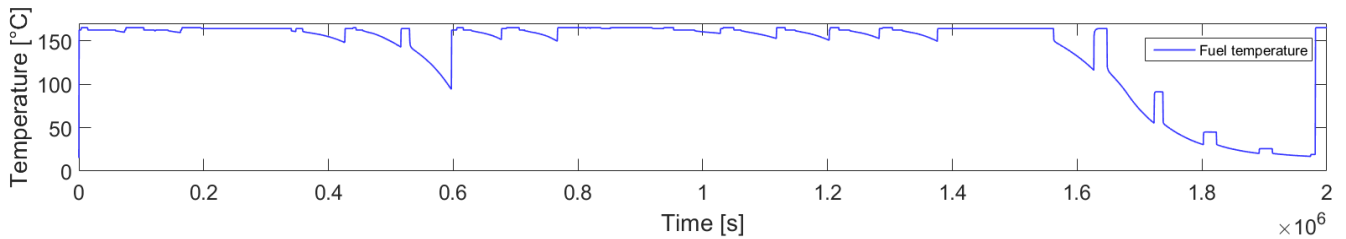
$$\text{Fuel savings percentage} = \frac{E_{gas}}{E_{system}} \cdot 100 \quad (9.1.1)$$



(a) Combined-cycle operating pattern with its corresponding mode



(b) Curtailment operating pattern and thermal storage mode



(c) Fuel temperature pattern

Figure 9.2: Illustrative simulation result.

The outcome of a complete simulation is only valid for one curtailment pattern and one storage size. To access how the outcome changes, different wind penetration levels and storage sizes investigated. The wind penetration level is changed to adjust the curtailment pattern. The storage module length and radii are changed to adjust the thermal storage characteristics. For each different curtailment pattern the SNSP limit, RR limit are taken as constants being 60%, 30% respectively. The demand is set equal to the exact demand as it was in 2015 for the Dutch grid. To assure that the outcome is practically independent of grid density two new grid convergence studies are performed for the largest length and inner radius. These are both represented in Appendix A, Figure A.8 and Figure A.9. For a length of 27.5 meter at a grid density of 121x21 the final temperature after 100,000 seconds of simulation differed 0.012% from that simulated with a 201x61 grid. For the radius, this difference was 0.019% on a 101x41 grid compared to that of a 201x61 grid. Therefore it was concluded that these grid densities are fine enough to give results independent of grid density. The reason for not refining the grid any further was due to its long corresponding computational time. On average, an annual simulation duration was around 10 hours on an ASUS N550JV-DB72T laptop.

9.2 Results

The annual fuel savings and reduction in CO₂ emissions are shown in Figure 9.3 and Figure 9.4 respectively. Unless stated otherwise, the thermal storage consists out of 2732 modules with a length of 20 meter, an inner radius of 5 cm, an outer radius of 10 cm and a HTF mass flow of 0.007 kg/s. From Figure 9.3a and Figure 9.3b a few interesting observations can be made. Firstly, all computed reductions in fuel usage are below the maximum limit of 0.85% as

calculated in chapter 5. Secondly, the annual fuel savings at a wind penetration of 10% are relatively low compared to other penetration levels. This is a direct result from the low occurrence of curtailment available. As expected, the higher the penetration level (and therefore the available curtailment), the higher the annual fuel savings. It seems that there is an exponential relation between annual savings and wind penetration level. Thirdly, decreasing the module length and inner radius leads to a reduction in fuel consumption. However, their relation is not linearly proportional. Doubling the module length does not lead to double the fuel savings. The effect that this behaviour has on the financial side of the project is further explained in chapter 10. This effect becomes more apparent for higher wind penetration levels as curtailment has a higher occurrence rate leading to smaller storage sizes becoming more effective. Shorter periods of zero-curtailment have to be overcome allowing for high savings corresponding to small storage sizes. When comparing the influence of length and radius between penetration levels a trend is clearly visible: the influence of storage size on fuel savings becomes less for higher wind penetration levels. Finally, at 50% wind penetration an optimum inner radius can be found at 7 cm. Increasing the radius beyond this point leads to a slight decrease in fuel reduction. This can be explained as follow: There is enough PCM mass available to overcome periods of low curtailment. However, the increase in radius leads to a slightly lower HTF velocity, and therefore HTC. This in turn reduces the energy transfer between the PCM and HTF.

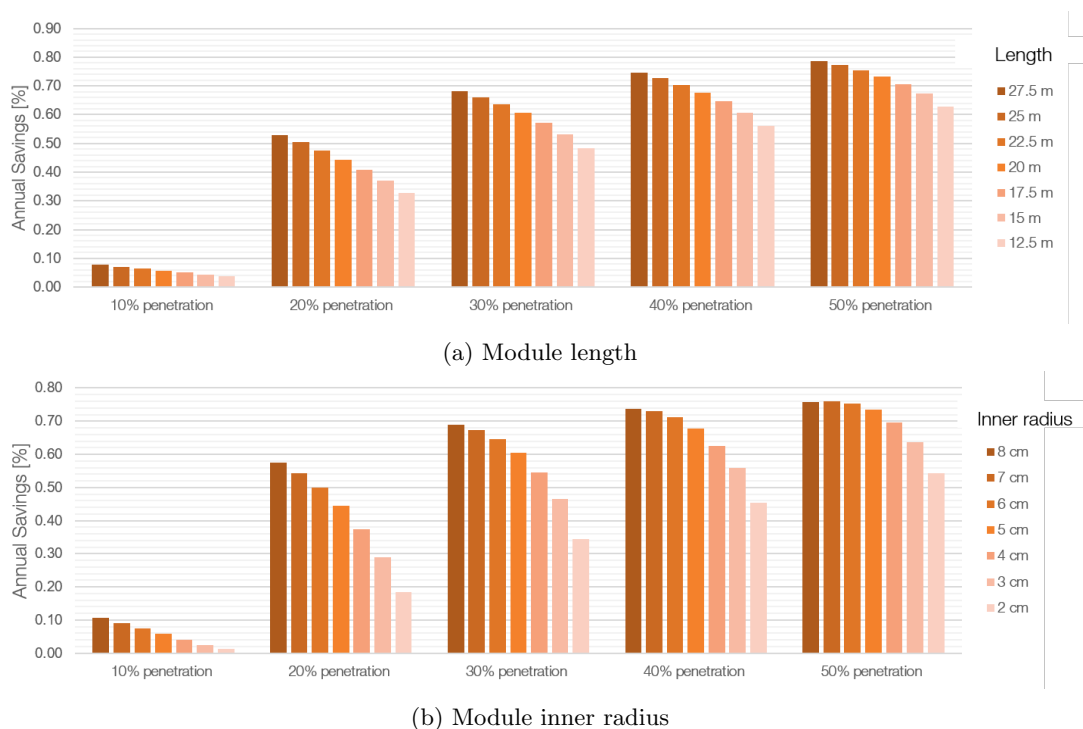


Figure 9.3: Annual fuel savings for different wind penetration levels and storage module dimensions.

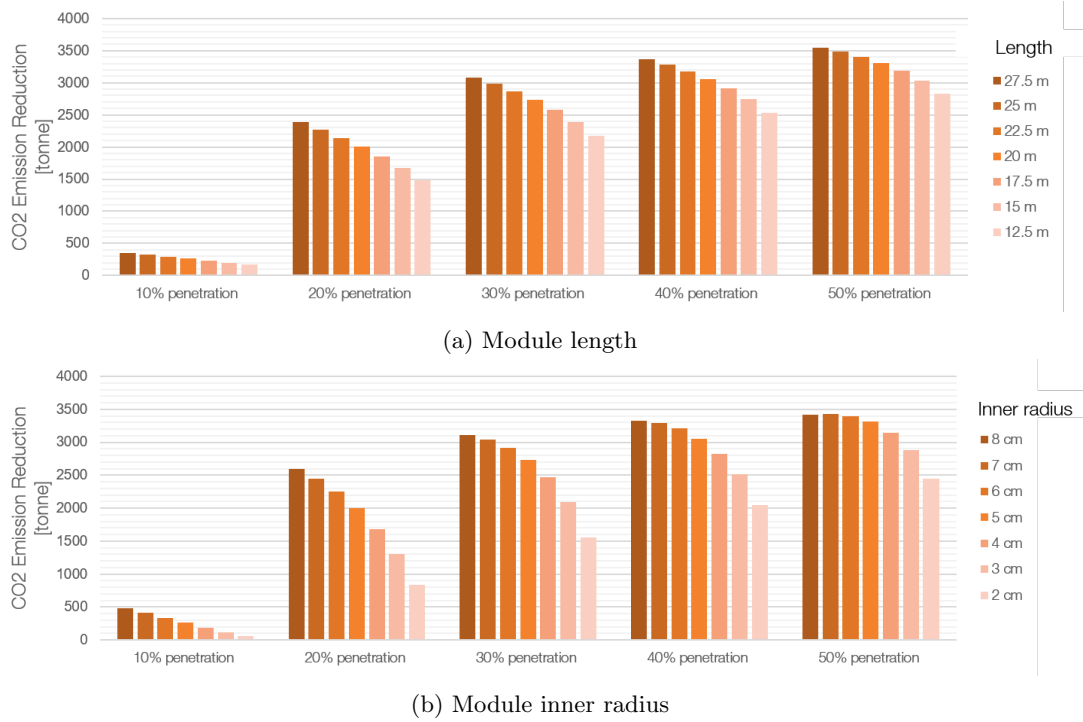


Figure 9.4: Annual reduction of CO₂ emissions for different wind penetration levels and storage module sizes.

9.3 Conclusions and Observations

Within this chapter three models have been combined successfully to simulate the annual performance of wind curtailment utilization. It combines the curtailment model from chapter 3 with both the CCPP model from chapter 5 and the thermal storage model from chapter 8. The integration was rather straightforward and involved outputs from the curtailment and CCPP models to define whether the storage was being charged, stationary or discharged. Using these patterns the storage model could simulate a HTF exhaust gas temperature throughout a complete year which was then converted to an annual fuel savings figure.

This type of simulation has been performed for different wind penetration levels, storage module lengths and storage module radii to show the impact of these parameters. It was found that the fuel savings are relatively low for wind penetration levels of 10% due to a low curtailment occurrence. For penetration levels above 20% the savings figure drastically increased compared to 10% values. It seems that there is an exponential relation between annual savings and wind penetration level. Regarding the impact of storage dimensions, it was found that doubling the storage size does not lead to double the savings. This comes forth from the intermittent nature of curtailment. For wind penetration levels below 30% it is more advantageous to increase the storage module length and radii compared to penetration levels above 30%. Increasing the module radii ultimately leads to an optimum. An indication for this behaviour was found at the maximum inner radius for a penetration of 50%. All annual fuel savings figures were below the maximum predicted percentage of 0.85% computed in chapter 5.

Chapter 10

Financial Feasibility

This chapter provides a brief overview of the financial side of curtailment utilization using the proposed method. Due to the project’s conceptual nature the outcome should not be considered definite. Many important parameters can fluctuate strongly over time such as gas prices, carbon taxes and material costs. This chapter is divided into three sections. The first deals with the financial benefits of curtailment utilization. The second section estimates associated investment costs related to the installation of a thermal storage. Finally, the payback period is computed and conclusions are drawn regarding the project’s financial health.

10.1 Financial Benefits

Two major financial benefits originate from the reduction in fuel consumption. The first being fairly obvious: a reduction in annual fuel costs. Absolute savings are highly depended on the local gas price which is highly volatile. The Netherlands currently experiences a relative low natural gas price compared to the previous ten years(105). In 2015 its average price was 7.54 EUR/GJ which is below its ten-year average of 7.73 EUR/GJ(105). The geographical price dependency for European countries is visualised in Figure 10.1. From this figure it can be concluded that the Netherlands is amongst the top three cheapest countries (Romania, Turkey, the Netherlands). The EU average fuel price in 2015 was 9.39 EUR/GJ which is significantly higher than the Dutch price of 7.54 EUR/GJ. Therefore, the implementation of curtailment utilization in the Netherlands leads to relatively low fuel cost savings compared to other European countries.

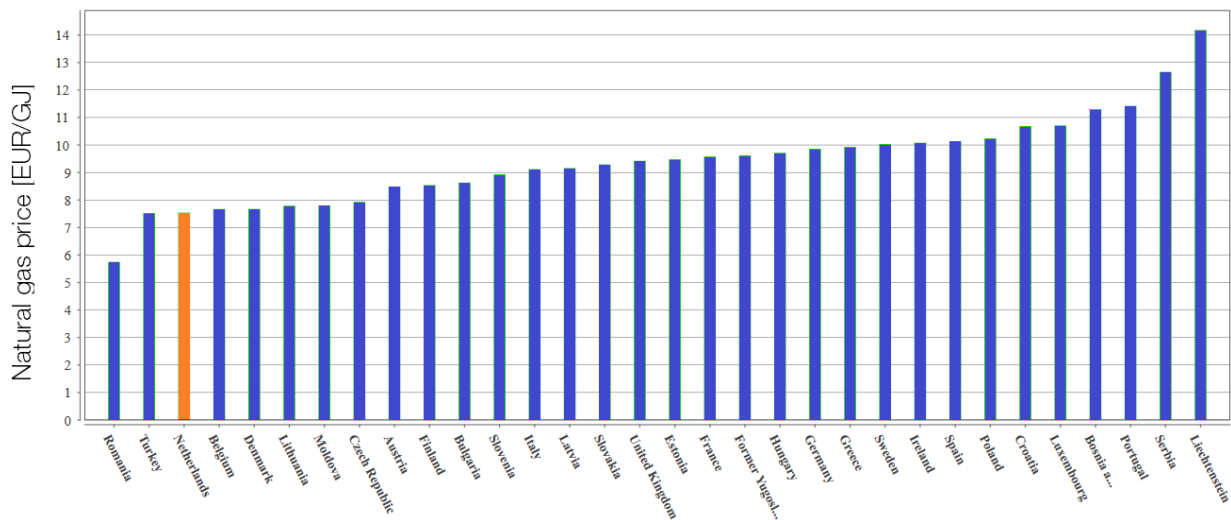


Figure 10.1: European natural gas prices for industrial consumers for the year 2015(105).

The second benefit comes from a reduction in emission allowance consumption. In 2005 the EU created the Emissions Trading System (ETS) in order to allow institutions to trade emissions allowances. These allowances represent the amount of carbon-dioxide institutions are allowed to emit yearly. For every tonne of carbon-dioxide emitted an allowance is consumed. The EU has set a maximum limit on the total amount of greenhouse gases institutions can emit each year. A fixed number of emission allowances are allocated or auctioned to institutions. Using the ETS, institutions can buy or sell allowances if they emit more or less than their own allowances represent. To reduce total emissions, the allowance limit reduces by 1.74% each year to reach an emission reduction of 21% in 2020 compared to

1990 levels for all covered sectors(106). The ETS covers more than 11,000 power stations and other energy-intensive industries. Together 45% of the total EU emissions are covered by the ETS(106). The prices at which allowances are sold is, just as the natural gas price, highly volatile. In 2016 the average price from the 1st of February till the 1st of August was 5.24 EUR/tonne CO₂ whereas it was 7.56 EUR/tonne CO₂ in 2015(107).

10.2 Investment Costs

Within the scope of this research two methods are used to estimate the investment costs related to the thermal storage. The first method estimates its total cost by means of the cost for TES per kWh as taken from Table 6.3. The average of this price range is approximately 36 EUR/kWh which is used in future calculations. Using this number and the maximum available energy within the storage its installation costs can be estimated. The total available energy is estimated by means of the specific enthalpy and total PCM mass. The second method is more straightforward and based on liberal assumptions. It estimates the PCM's mass and links this to a specific PCM cost. For organic PCM's such as A164 an average price is estimated at 2.00 EUR/kg(108). Using the total mass and price per mass the total PCM price can be computed. To include the remaining material and labour costs this cost is doubled for the final storage costs. It is unclear whether these two methods are independent of one another since the exact calculation procedure for the TES price per kWh from Table 6.3 is unknown.

A notable mention has to be made regarding investment risk corresponding to the investment costs. This risk is, amongst others, dependent on the available capital of an investor. If risk can be segmented into probability and severity, investments which require a large portion of one's capital come with a high severity. The probability of a failed investment remains the same but the consequences for the investor are more significant. Therefore, it is relevant to report the total investment costs when discussing the financial feasibility of a project. For this purpose, the investment costs are included in the following graphs for each scenario.

10.3 Payback Period

Using the previously described methods and the numbers for annual fuel savings per storage size, the annual profits and investment costs can be calculated. As an example, the balance sheet in Table 10.1 is presented for a storage module length of 15 meter and an annual fuel savings percentage of 0.53% (30% wind penetration). On the profit side one can see that a large portion of the savings comes from fuel savings rather than the sale of carbon allowances. As mentioned, the gas price is relatively low in the Netherlands. Therefore its annual profit should be taken as being close to the lower boundary rather than an European average. For the costs side it seems that both methods estimate a rather similar investment cost. Therefore, the assumption is made that the order of magnitude of the investment cost is correct. To calculate the payback period the costs from method 1 are used due to its more scientific approach. Using the data presented in Table 10.1 the payback period for this scenario equals approximately 15.2 years. The inflation rate has been set to zero since the EUR inflation rates were close to zero for 2016(109). In July 2016 the Dutch inflation rate was even negative at a rate of -0.3%(110).

Table 10.1: Annual balance sheet.

Profit			Investment Costs		
Parameter	Value	Unit	Parameter	Value	Unit
Input			Input		
Annual gas consumption	212,030	[tonne]	Number of pipes	2,732	[-]
Energy consumption	8,056,693	[GJ]	PCM volume per pipe	0.47	[m ³]
CO ₂ emitted	451,191	[tonne]	PCM density (liquid)	1,500	[kg/m ³]
Gas consumption savings	0.53	[%]	PCM latent heat of fusion	306	[kJ/kg]
			PCM specific heat capacity (liquid)	2.4	[kJ/kg K]
Price per GJ of gas	7.54	[EUR]	Price per kg of PCM	2.00	[EUR]
Price per allowance	5.24	[EUR]	Price per kWh	40.00	[EUR]
Output			Output		
Total fuel profits	321,970	[EUR]			
Total allowance profits	12,530	[EUR]			
Total profit	334,501	[EUR]	Total costs (method 1)	5,078,890	[EUR]
			Total costs (method 2)	5,793,411	[EUR]

10.4 Results

For all variations of module lengths and radii, the payback periods are computed for different wind penetration levels. This is done by using two different rates since the Dutch rates were not found to be representative for the whole of the EU. The first rate represents the most recent gas and carbon allowances prices for the Netherlands. The natural gas price is set to 7.54 EUR/GJ and the carbon allowances to 5.24 EUR/tonne. These results are presented in Figure 10.2a and Figure 10.3a. The second rate consists out of the EU averaged gas price and the average carbon allowance rate for 2015. The natural gas price is increased to 9.39 EUR/GJ and the carbon allowances to 7.56 EUR/tonne (2015 rates). The payback periods as computed with these rates are displayed in Figure 10.2b and Figure 10.3b.

From these figures it can clearly be observed that the payback periods for a wind penetration of 10% are significantly higher than those for other penetration levels. This is a direct result from the low presence of curtailment at this penetration level. As these high payback periods skew the scales, it has been omitted to provide a better overview as is visible in Figure 10.4 and Figure 10.5. Three main conclusions can be drawn. Firstly, the payback periods drastically decrease for higher wind penetrations levels due to a larger availability of curtailment. Secondly, decreasing the storage module length leads to a shorter payback period since the fuel savings do not grow proportionally with storage size as explained previously. This allows for a large scale on which this concept is applicable depending on the desired payback period and initial investment costs. Finally, all figures show that the payback periods for the Netherlands are relatively higher than those for the European average as a result of its low natural gas prices. The Netherlands has relatively unfortunate rates when it comes to payback periods in comparison to the rest of the EU.

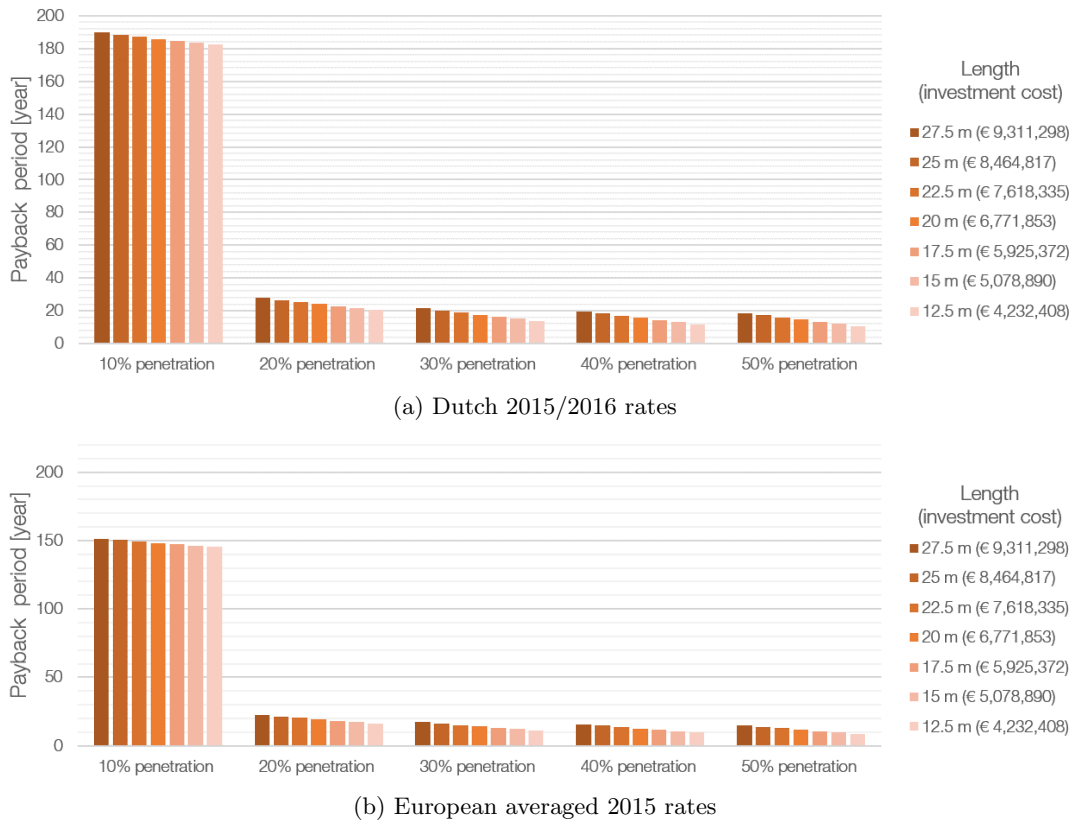


Figure 10.2: Payback periods for various module lengths (All penetration levels).

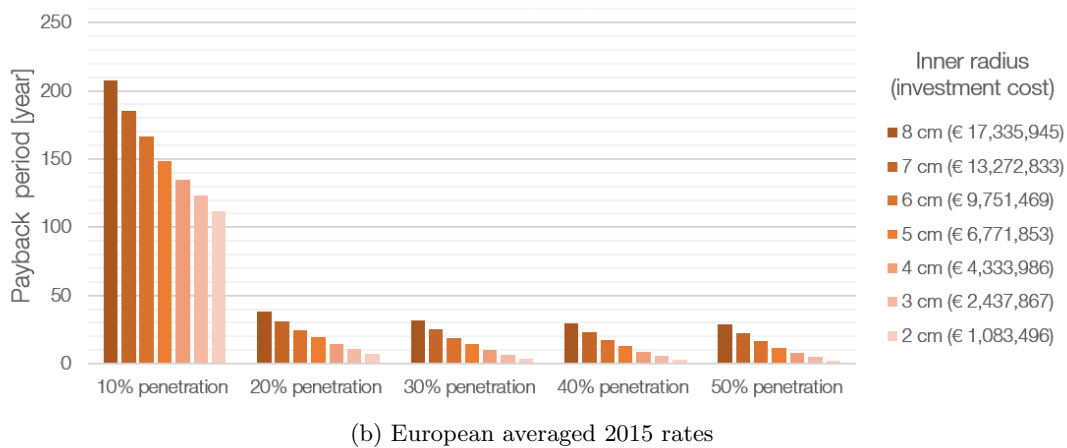
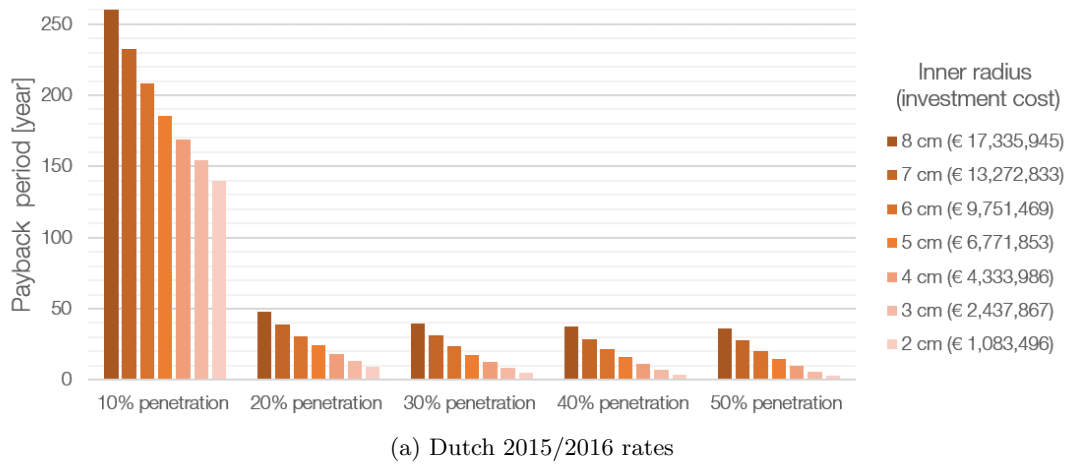


Figure 10.3: Payback periods for various module inner radii (All penetration levels).

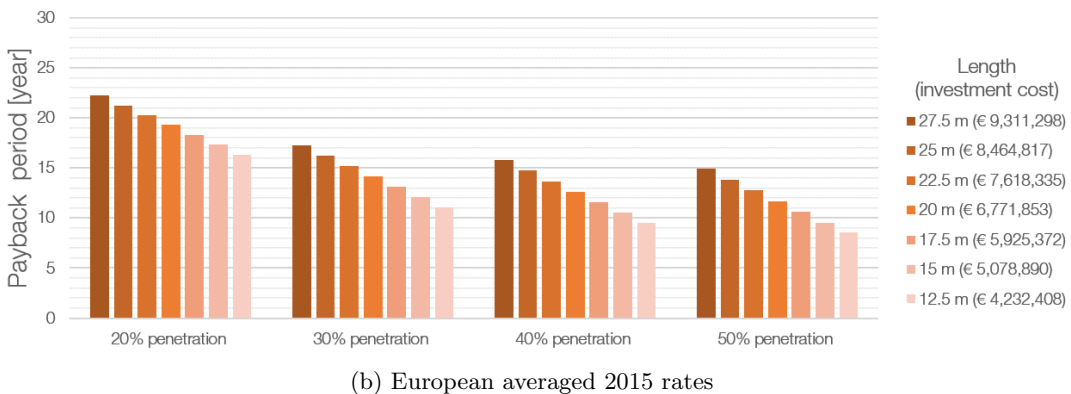
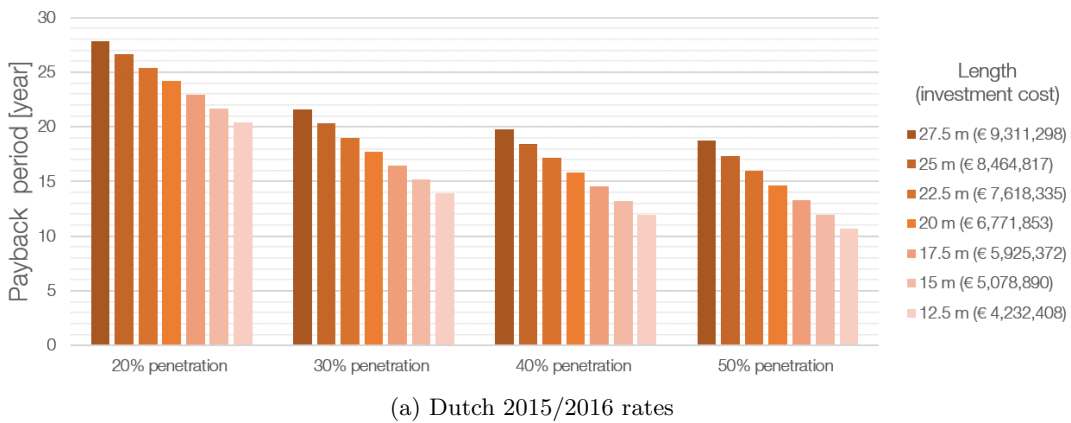


Figure 10.4: Payback periods for various module lengths.

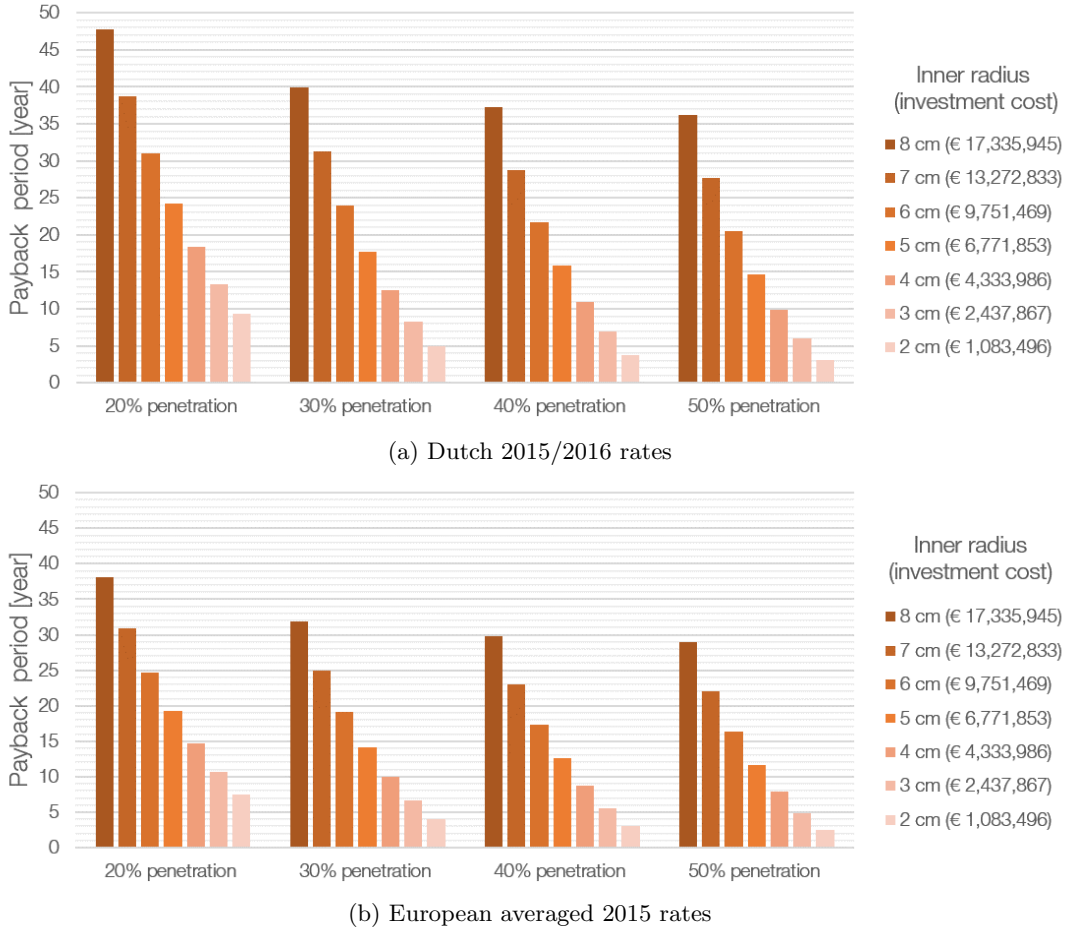


Figure 10.5: Payback periods for various module inner radii.

10.5 Environmental Performance as compared to Wind Energy

An interesting metric for a new technology is the cost required to reduce CO₂ emissions by one kilogram (hereafter referred to as λ). This metric is computed for two cases: the case of wind energy and the case of curtailment utilization. For the performance of wind turbines a 3 MW turbine with a capacity factor of 30% and a total lifespan of 20 years (τ_{WT}) is considered(111; 112). In 2009 the European Wind Energy Association (EWEA) estimated that wind turbine installation costs within Europe are approximately 1,227 EUR/kW. Due to this being a fairly old source it is assumed that by 2020 this price has decreased by 15% to 1041 EUR/kW(113). In addition, EWEA estimated that maintenance costs can be set at a rate of 1,45 cEUR/kWh. Using these numbers its annual electricity generation can be computed together with its total lifetime costs using Equation 10.5.1 and Equation 10.5.2 respectively.

$$E_{generated} = P_{max} \cdot capacity\ factor \cdot 24 \cdot 365 \quad (10.5.1)$$

$$C_{total} = C_{investment} + C_{maintenance} \cdot E_{generated} \cdot \tau_{WT} \quad (10.5.2)$$

Since the electricity generated by wind turbines displaces existing thermal generators, their annual electricity generation can directly be coupled to a reduction in global CO₂ emissions. Before proceeding, it is important to state two vital assumptions. Firstly, it is assumed that all electricity generated by wind directly displaces the generation of thermal generators. This is not always the case as explained in chapter 2. Secondly, the production and operation of wind turbines and CCPPs are also causes of CO₂ emissions which are not accounted for. The amount of displaced CO₂ depends on the "cleanness" of the thermal generators which would otherwise supply power to the grid. In the most optimistic case these generators are coal fired emitting 0.98 kg/kWh of CO₂. This case is optimistic since this number is lower for CCPP power plants, leading to a higher λ . Using Equation 10.5.3, the final price per emitted kilogram of CO₂ can be computed for the complete lifetime of a 3 MW wind turbine. Here it was found that $\lambda_{WT} = 0.035$ EUR/kg CO₂.

$$\lambda_{WT} = \frac{C_{total}}{E_{generated} \cdot 0.98 \cdot \tau_{WT}} \quad (10.5.3)$$

To compute λ_{CCPP} for a CCPP with curtailment utilization the procedure is fairly straightforward. It is computed by dividing the investment costs by the annual CO₂ reduction times the expected lifespan of the thermal storage. This is mathematically represented in Equation 10.5.4.

$$\lambda_{CCPP} = \frac{C_{total}}{annual\ CO_2\ reduction \cdot \tau_{TES}} \tag{10.5.4}$$

Since the investment cost depends on the storage size, different values for λ_{CCPP} can be found for different storage sizes. Comparing λ_{CCPP} to λ_{WT} for each storage size and wind penetration level indicates whether it is financially beneficial to use curtailment utilization instead of the installation of wind turbines to reduce CO₂ emissions from electricity generators. The results of this analysis is displayed in Table 10.2. Based on this analysis, it is cheaper to utilize curtailment to achieve the goal of reducing CO₂ emissions for all wind penetration levels above 20%. For penetration levels of 10% the storage dimensions play an important role on whether the same conclusion holds. Since the Netherlands had a wind penetration of 5.84% in 2015, it is fairly safe to assume that at this point in time that the installation of wind turbines is more efficient and required to achieve higher penetration levels. However, it has been shown that there is a turnaround point where curtailment utilization becomes more financially attractive.

Length[m]	Wind penetration [%]					Inner radius[cm]	Wind penetration [%]				
	10	20	30	40	50		10	20	30	40	50
27.5	0.689	0.127	0.106	0.099	0.096	8	0.503	0.074	0.057	0.052	0.050
25.0	0.804	0.134	0.108	0.100	0.096	7	0.549	0.078	0.059	0.054	0.051
22.5	0.981	0.146	0.113	0.102	0.097	6	0.606	0.082	0.062	0.056	0.052
20.0	1.261	0.164	0.120	0.108	0.099	5	0.677	0.088	0.065	0.058	0.053
17.5	1.793	0.195	0.133	0.116	0.104	4	0.758	0.096	0.068	0.061	0.055
15.0	2.912	0.252	0.157	0.131	0.114	3	0.891	0.105	0.074	0.064	0.058
12.5	5.919	0.396	0.212	0.160	0.134	2	1.063	0.119	0.081	0.070	0.062

Table 10.2: $\lambda_{CCPP}/\lambda_{WT}$ ratios for different storage module lengths and inner radii. Red values indicate that $\lambda_{CCPP} > \lambda_{WT}$.

10.6 Conclusions and Observations

Using the methods explained previously the project payback period has been computed for various wind penetration levels and storage module sizes. It seems highly unlikely that curtailment utilization is feasible for wind penetration levels less than 20% due to a low availability of curtailment. The payback period decreases rapidly for larger wind penetration levels making curtailment utilization becomes more attractive for higher penetration levels. Both storage module length and radii strongly influence the payback period as smaller lengths and radii leads to shorter periods. This indicates that the concept has a wide range of applicability depending on the users requirements and financial situation. It was observed that curtailment utilization in Dutch power plants leads to relatively high payback periods compared to the EU average. This is a direct result of the low natural gas price in the Netherlands. In addition, the wind penetration level of the Netherlands in 2015 was rather low compared to other European countries.

Comparing the concept’s price per kilogram reduction in CO₂ emissions to wind turbines leads to interesting insights. Firstly, at the current wind penetration level for the Netherlands, it is likely that it is cheaper to use wind turbines rather than curtailment utilization when one’s goal is to reduce CO₂ emissions as inexpensive as possible. However, there is a turnaround point at which it is more beneficial to apply curtailment utilization at CCPPs. Analysis showed that for penetration levels of 10% the storage size determines decision making. At penetration levels of 20% or higher all simulated storage sizes leads to lower CO₂ reduction prices.

Chapter 11

Conclusions and Recommendations

The research objective of this research was to assess the technical and financial feasibility of curtailment utilization to preheat natural gas entering a combined-cycle power plant by simulating the annual performance of a such a power plant. This objective was achieved by the creation of three models: one to simulate the occurrence and quantity of wind curtailment, one to simulate the off-design performance of a combined-cycle power plant and one to simulate a thermal storage system used for the storage of curtailment.

Before the development of the curtailment prediction model a distinction was made between constrained and curtailed wind. Both concepts were explained and the two main causes for curtailed wind were elaborated upon. These were frequency control and regulating and reserve requirements. These limits were represented by the SNSP and RR limits to predict the occurrence of curtailment. Model input parameters are the national demand, wind production, SNSP and RR limits. The model was verified and used to simulate various annual curtailment values for the complete ranges of the SNSP and RR limits. This simulation was performed for several national wind penetration levels to identify the impact of a higher share of IRES on curtailment.

The working principles and major components present in a CCPP were explained and its thermal efficiency mathematically expressed in terms of its gas and steam turbine thermal efficiencies. It was shown that CCPP operate more efficiently than solely a Brayton or Rankine cycle when used for electricity generation. To successfully model the power plants performance, the Siemens SGT5-4000F gas turbine was first modelled separately by means of three different simulation software: THERMOFLEX, GSP and Cycle-Tempo. For the design point simulation all three software yielded similar results and can therefore all be used for gas turbine design point simulation. For off-design simulations results differed to an extent. THERMOFLEX and Cycle-Tempo yielded similar simulation results in contrast to GSP. The developed off-design gas turbine models were used to create the CCPP model in THERMOFLEX and Cycle-Tempo. Just as for the gas turbine simulations the design point results matched well for both software. Off-design performance simulation results displayed similar results for all parameters of interest except for the turbine inlet temperature. Validation showed that off-design performance can differ significantly and that more accurate models can improve the validity of the results. CCPP results from THERMOFLEX were used together with the Hemweg 9 operating pattern for 2015 to simulate the power plants annual performance.

A summary on energy storage was created from literature to explain energy storage principles and performance values for different energy storage methods. Using this summary, it was concluded that thermal energy storage is a suitable candidate for the temporary storage of curtailment. To decide on the most efficient and practical method to utilize curtailment two concepts were evaluated based on four different criteria. These concepts were the heating of compressor exhaust air and the heating in natural gas before it enters the gas turbine. The four evaluation criteria were: most beneficial location of energy addition, maximum transferable energy, ease of energy transfer to gas by convection and any remaining practical considerations. Based on these four criteria, it was decided to investigate the effects of curtailment utilization by means of heating natural gas to approximately 160°C.

A thermal energy storage was simulated which made use of both sensible and latent heat storage. The storage consisted out of multiple modules in parallel. A single module consists of a hollow insulated cylinder with the HTF flowing internally which contains A164 as PCM. The model was verified and validated by means of an energy balance and its agreement with literature. It was used to evaluate the impact of seven different parameters on the exhaust gas temperature. These parameters were: module length, inner radius, radii ratio, thermal conductivity of the PCM (both for liquid and solid phase) and for the specific heat capacity of the PCM. The results gave insights on how these parameters change the HTF exhaust temperature pattern which can be used for optimization of the storage module.

The three models were combined to simulate the plants annual performance with wind curtailment utilization. This simulation has been performed for different wind penetration levels, storage module lengths and storage module radii. It was found that the fuel savings can be obtained up to 0.85%. Relatively low for wind penetration levels of 10% due to

a low curtailment occurrence. An exponential relation was found between annual savings and wind penetration level. For high penetration levels, an optimum storage radii was found due to its coupling with PCM mass and HTC.

The projects financial feasibility was accessed via its payback period and its price to reduce CO₂ emissions as compared to wind turbines. It seems unlikely that the use of curtailment utilization is realistic for wind penetration levels lower than 20%. This changes with the installation of wind turbines since the payback period decreases rapidly for higher penetration levels. For wind penetration levels of approximately 10% it can be financially beneficial to use small scale curtailment utilization rather than the implementation of wind turbine if one aims to reduce CO₂ emissions as inexpensive as possible.

11.1 Recommendations for Future Research

A list of recommendations is provided to identify any improvements that can be made to the performed research. These recommendations are ordered by topic for clarity. The main research recommendations are as follows:

Project Scope

- Assess the financial and technical feasibility of solar curtailment as compared to wind curtailment. Perhaps no thermal storage due to a better match between solar curtailment and CCPP operation patterns.
- Identify the benefits of using curtailment in CHP power plants as no thermal storage is required to be present.

Curtailment Model

- Implement the full curtailment model as described in (18) to model curtailment starting from basic grid parameters.
- Improve model accuracy by setting the RR limit to a hourly constant based on the day of the week and current time rather than a yearly constant.

Combined-cycle Model

- Include the transient behaviour to simulate power plant performance more accurately. This should lead to more accurate values for annual fuel consumption and electricity generation.
- Create a model for the plant architecture of the reference plant presented during validation to identify the accuracy of CCPP plant modelling in THERMOFLEX and Cycle-Tempo.

Thermal Storage Model

- Take into account heat losses rather than complete insulation to investigate the effects of long term storage on PCM temperature.
- The addition of natural convection within the PCM to improve the model accuracy.
- Account for the change in HTF flow velocity and density when it is being heated. In addition, introduce a variable HTC based on the average HTF properties of the inlet and outlet.
- Include both heating elements in the nodal network.
- Vary the module mass flows to identify its impact on storage performance.
- Optimize a single storage module to have specific performance characteristics while minimizing PCM mass and storage volume.

Model Integration

- Model the combined-cycle performance for different fuel temperatures to identify the reduction in fuel consumption per temperature increase.
- Implement a dynamic heating process for the heating elements rather than an instantaneous temperature change.
- Develop and optimize a strategy for the charge and discharge of separate storage modules when the combined-cycle is running at off-design conditions.

- Simulate the annual savings for different power plant operating patterns. These patterns should be dependent on the wind penetration level and should therefore differ for different IRES levels. If no real-life data can be found, the Hemweg 9 pattern can serve as a baseline and various patterns can be generated by means of a Markov chain. A large number of patterns can be used to evaluate the benefits of curtailment utilization on an annual basis.
- Changing the SNSP limit, RR limit and demand corresponding to each wind penetration level, one could make predictions for future scenario's rather than solely see the influence of wind penetration level.

Financial Feasibility

- Perform optimization for the storage on number of cylinders, length and thickness with as objective function minimized storage costs.
- Include maintenance costs for the thermal storage in payback period calculations.

References

- [1] European Union Committee, “The EUs Target for Renewable Energy 20 percent by 2020,” report, 2008.
- [2] International Energy Agency, “Recent Energy Trends in OECD, Excerpt from: Energy Balances of OECD Countries,” report, 2015.
- [3] International Energy Agency, “World Energy Trends, Excerpt from: Energy Balances of Non-OECD Countries,” report, 2015.
- [4] I. Schröppel, “Electrical Power Vision 2040 for Europe - a EUREL study,” *Elektrotechnik und Informationstechnik*, vol. 130, no. 3, 2013.
- [5] World Energy Council, “World Energy Resources ,” report, 2013.
- [6] L. W. M. Beurskens, M. Hekkenberg, and P. Vethman, “Renewable energy projections as published in the national renewable energy action plans of the European member states,” report, 2011.
- [7] A. S. Brouwer, M. van den Broek, A. Seebregts, and A. Faaij, “Impacts of large-scale Intermittent Renewable Energy Sources on electricity systems, and how these can be modeled,” *Renewable and Sustainable Energy Reviews*, vol. 33, pp. 443–466, 2014.
- [8] A. S. Brouwer, M. van den Broek, A. Seebregts, and A. Faaij, “Operational flexibility and economics of power plants in future low-carbon power systems,” *Applied Energy*, vol. 156, pp. 107–128, 2015.
- [9] T. M. Patrick, G. Jurgen, A. Price, and B. Droste-Franke, *Electrochemical Energy Storage for Renewable Sources and Grid Balancing*. Amsterdam: Elsevier, 2015.
- [10] M. Beaudin, H. Zareipour, A. Schellenbergglabe, and W. Rosehart, “Energy storage for mitigating the variability of renewable electricity sources: An updated review,” *Energy for Sustainable Development*, vol. 14, no. 4, pp. 302–314, 2010.
- [11] J. P. Barton and D. G. Infield, “Energy storage and its use with intermittent renewable energy,” *Energy Conversion, IEEE Transactions on*, vol. 19, no. 2, pp. 441–448, 2004.
- [12] S. Ruester, X. He, L. Vasconcelos, and J. Glachant, “Electricity storage: how to facilitate its deployment and operation in the EU,” *Think Final Report, European University Institute*, 2012.
- [13] J. Arai, K. Iba, T. Funabashi, Y. Nakanishi, K. Koyanagi, and R. Yokoyama, “Power electronics and its applications to renewable energy in Japan,” *Circuits and Systems Magazine, IEEE*, vol. 8, no. 3, pp. 52–66, 2008.
- [14] T. Kousksou, P. Bruel, A. Jamil, T. El Rhafiki, and Y. Zeraouli, “Energy storage: Applications and challenges,” *Solar Energy Materials and Solar Cells*, vol. 120, Part A, pp. 59–80, 2014.
- [15] A. Pensini, C. N. Rasmussen, and W. Kempton, “Economic analysis of using excess renewable electricity to displace heating fuels,” *Applied Energy*, vol. 131, pp. 530–543, 2014.
- [16] P. Verschuren and H. Doorewaard, *Designing a research project*, vol. 2. Eleven International Publishing, 2010.
- [17] EirGrid, SONI, “2012 Curtailment Report,” report, 2013.
- [18] E. McKenna, P. Gruinewald, and M. Thomson, “Going with the wind: temporal characteristics of potential wind curtailment in Ireland in 2020 and opportunities for demand response,” *Renewable Power Generation, IET*, vol. 9, no. 1, pp. 66–77, 2015.
- [19] E. V. Mc Garrigle, J. P. Deane, and P. G. Leahy, “How much wind energy will be curtailed on the 2020 Irish power system?,” *Renewable Energy*, vol. 55, pp. 544–553, 2013.
- [20] H. De Keulenaer, “Voltage and Frequency Control of the Grid.” Available at: ”<http://www.leonardo-energy.org/tools-and-tutorials/voltage-and-frequency-control-grid>”. Accessed online: 21-04-2016.

- [21] TenneT, “Offering of regulating and reserve capacity.” Available at: ”http://www.tennet.org/english/operational_management/system_data_preparation/offering_regulating_reserve_capacity/index.aspx”. Accessed online: 10-10-2016.
- [22] Danish Wind Industry Association, “Asynchronous (Induction) Generators .” Available at: ”<http://drmstrre.dk/wp-content/wind/miller/windpower%20web/en/tour/wtrb/async.htm>”. Accessed online: 24-10-2016.
- [23] National Grid, “Historical Demand Data .” Available at: ”www2.nationalgrid.com/UK/Industry-information/Electricity-transmission-operational-data/Data-Explorer/HTTP”. Accessed online: 16-02-2016.
- [24] Centraal Bureau voor de Statistiek, “Windenergie; elektriciteitsproductie, capaciteit en windaanbod per maand.” Available at: ”<https://www.cbs.nl/>”. Accessed online: 17-11-2015.
- [25] Center for Climate and Energy Solutions, “Leveraging natural gas to reduce greenhouse gas emissions.” Available at: ”<http://www.c2es.org/publications/leveraging-natural-gas-reduce-greenhouse-gas-emissions>”. Accessed online: 03-03-2016.
- [26] R. Kehlhofer, F. Hannemann, B. Rukes, and F. Stirnimann, *Combined-Cycle Gas Steam Turbine Power Plants*. 2009.
- [27] D. Vyncke-Wilson, “Advantages of aeroderivative gas turbines: technical and operational considerations on equipment selection,” 2013.
- [28] Coen Company, “Value-Added Applications of Supplementary Firing in Gas Turbine Based Cogeneration Plants.” Available at: ”<http://www.coen.com/library/technical-papers/value-added-applications-of-supplementary-firing-in-gas-turbine-based-cogeneration-plants/>”. Accessed online: 10-10-2016.
- [29] V. Ganapathy, “Heat-Recovery Steam Generators: Understand the Basics.” 1996.
- [30] J. H. Horlock, *Combined Power Plants: Including Combined Cycle Gas Turbined CCGT Plants*. Elsevier, 1992.
- [31] S. Sarco, “Dry Saturated Steam Tables.” Available at: ”http://www.spiraxsarco.com/Documents/Dry_Saturated_Steam_Tables-Technical_Information.pdf”. Accessed online: 22-03-2016.
- [32] Siemens, “SST-PAC 5000 - Steam Turbine Package,” report, 2016.
- [33] Siemens, “The SGT5-8000H proven in commercial operation,” report, 2011.
- [34] Nuon, “Gasgestookte centrales.” Available at: ”<https://www.nuon.com/activiteiten/productie/gas/gasgestookte-centrales/#Hemweg>”. Accessed online: 27-04-2016.
- [35] Siemens, “Elektriciteitscentrales Hemweg 9 en Diemen 34 officieel in gebruik genomen.” Available at: ”<http://www.corporate.siemens.nl/nl/pers-nieuws/elektriciteitscentrales-hemweg-9-en-diemen-34-officieel-in-gebruik-genomen.htm>”. Accessed online: 27-04-2016.
- [36] ENTSO-E, “Actual Generation per Generation Unit.” Available at: ”<https://transparency.entsoe.eu/generation/r2/actualGenerationPerGenerationUnit/>”. Accessed online: 27-04-2016.
- [37] Siemens, “Siemens Gas Turbine SGT5-4000F,” report, Siemens AG, 2008.
- [38] Siemens, “Siemens Steam Turbine SST-5000 Series,” report, Siemens AG, 2010.
- [39] Siemens, “The Hydrogen-Cooled SGen-2000H Generator Series,” report, Siemens AG, 2013.
- [40] Siemens, “SCC5-4000F (SST5-5000) for cold climate conditions.” Available at: ”http://www.slideshare.net/siemens_answers/power-generation-power-plants”. Accessed online: 05-01-2016.
- [41] Asimptote, “Technical notes Cycle-Tempo Release 5,” report.
- [42] Geocaching, “Slochteren 1.” Voltage and Frequency Control of the Grid ”https://www.geocaching.com/geocache/GC243MK_slochteren-1?guid=b2998cd0-defd-4dce-a11b-3433890aa437”. Accessed online: 23-04-2016.
- [43] Asimptote, “Cycle-Tempo.” Available at: ”<http://www.asimptote.nl/software/cycle-tempo/>”. Accessed online: 27-04-2016.
- [44] Thermoflow, “THERMOFLEX.” Available at: ”<http://thermoflex.com/>”. Accessed online: 27-04-2016.

- [45] Netherlands Aerospace Centre, “Gas Turbine Simulation Programme.” Available at: “<http://www.gspteam.com/>”. Accessed online: 20-11-2015.
- [46] W. Visser, M. Bruin, and S. Kluiters, “GSP 11 User Manual,” report, National Aerospace Laboratory NLR, 2013.
- [47] E. Deuker, H. Streb, J. Slad, M. Moeller, and M. Koenig, “SGT5-4000F Gas Turbine and Combined Cycle Power Plant Evolution Reflecting the Changing Market Requirements,” report, 2013.
- [48] X. Olsthoorn and A. Pielaat, “Tier-2 uncertainty analysis of the Dutch greenhouse gas emissions 1999.” 2002.
- [49] H. Chen, T. N. Cong, W. Yang, C. Tan, Y. Li, and Y. Ding, “Progress in electrical energy storage system: A critical review,” *Progress in Natural Science*, vol. 19, no. 3, pp. 291–312, 2009.
- [50] A. González, E. McKeogh, and B. Ó. Gallachóir, “The role of hydrogen in high wind energy penetration electricity systems: The Irish case,” *Renewable Energy*, vol. 29, no. 4, pp. 471–489, 2004.
- [51] A. Tuohy and M. OMalley, “Pumped storage in systems with very high wind penetration,” *Energy Policy*, vol. 39, no. 4, pp. 1965–1974, 2011.
- [52] T. R. Ayodele and A. S. O. Ogunjuyigbe, “Mitigation of wind power intermittency: Storage technology approach,” *Renewable and Sustainable Energy Reviews*, vol. 44, pp. 447–456, 2015.
- [53] F. Díaz-González, A. Sumper, O. Gomis-Bellmunt, and R. Villafáfila-Robles, “A review of energy storage technologies for wind power applications,” *Renewable and Sustainable Energy Reviews*, vol. 16, no. 4, pp. 2154–2171, 2012.
- [54] D. Connolly, H. Lund, B. V. Mathiesen, E. Pican, and M. Leahy, “The technical and economic implications of integrating fluctuating renewable energy using energy storage,” *Renewable Energy*, vol. 43, pp. 47–60, 2012.
- [55] S. Rehman, L. M. Al-Hadhrami, and M. M. Alam, “Pumped hydro energy storage system: A technological review,” *Renewable and Sustainable Energy Reviews*, vol. 44, pp. 586–598, 2015.
- [56] R. Hunter, G. Elliot, and O. Carlson, “Wind-diesel systems,” report, Chalmers University of Technology, Department of Electrical Machines and Power Electronics, 1994.
- [57] D. Aydin, S. P. Casey, and S. Riffat, “The latest advancements on thermochemical heat storage systems,” *Renewable and Sustainable Energy Reviews*, vol. 41, pp. 356–367, 2015.
- [58] P. Pardo, A. Deydier, Z. Anxionnaz-Minvielle, S. Roug, M. Cabassud, and P. Cognet, “A review on high temperature thermochemical heat energy storage,” *Renewable and Sustainable Energy Reviews*, vol. 32, pp. 591–610, 2014.
- [59] A. Gil, M. Medrano, I. Martorell, A. Lzaro, P. Dolado, B. Zalba, and L. F. Cabeza, “State of the art on high temperature thermal energy storage for power generation. Part 1 Concepts, materials and modellization,” *Renewable and Sustainable Energy Reviews*, vol. 14, no. 1, pp. 31–55, 2010.
- [60] H. P. Garg, S. C. Mullick, and V. K. Bhargava, *Solar thermal energy storage*. Springer Science and Business Media, 1985.
- [61] M. Felderhoff, R. Urbanczyk, and S. Peil, “Thermochemical heat storage for high temperature applicationsa review,” *Green*, vol. 3, no. 2, pp. 113–123, 2013.
- [62] N. Pflieger, T. Bauer, C. Martin, M. Eck, and A. Wörner, “Thermal energy storage - overview and specific insight into nitrate salts for sensible and latent heat storage,” *Beilstein Journal of Nanotechnology*, vol. 6, no. 1, pp. 1487–1497, 2015.
- [63] D. Gardner, “Hydrogen production from renewables,” *Renewable Energy Focus*, vol. 9, no. 7, pp. 34–37, 2009.
- [64] S. Schiebahn, T. Grube, M. Robinius, V. Tietze, B. Kumar, and D. Stolten, “Power to gas: Technological overview, systems analysis and economic assessment for a case study in Germany,” *International Journal of Hydrogen Energy*, vol. 40, no. 12, pp. 4285–4294, 2015.
- [65] C. Derive, D. Madet, and M. Roche, “Hydrogen in gas turbines,” *International Journal of Hydrogen Energy*, vol. 12, no. 7, pp. 501–504, 1987.
- [66] H. Ibrahim, A. Ilinca, and J. Perron, “Energy storage systems Characteristics and comparisons,” *Renewable and Sustainable Energy Reviews*, vol. 12, no. 5, pp. 1221–1250, 2008.
- [67] S. M. Shoenung, “Characteristics and technologies for long-vs. short-term energy storage: a study by the DOE energy storage systems program,” report, Technical report. SAND2001-0765. Sandia National Laboratories. United States Department of Energy. Published March, 2001.

- [68] S. Faias, P. Santos, J. Sousa, and R. Castro, "An overview on short and long-term response energy storage devices for power systems applications," vol. 5, p. 6, 2008.
- [69] T. E. Lipman, R. Ramos, and D. M. Kammen, "An assessment of battery and hydrogen energy storage systems integrated with wind energy resources in California," *University of California, Berkley*, 2005.
- [70] I. Hadjipaschalis, A. Poullikkas, and V. Efthimiou, "Overview of current and future energy storage technologies for electric power applications," *Renewable and sustainable energy reviews*, vol. 13, no. 6, pp. 1513–1522, 2009.
- [71] C. D. Parker, "Leadacid battery energy-storage systems for electricity supply networks," *Journal of Power Sources*, vol. 100, no. 1, pp. 18–28, 2001.
- [72] W. Smith, "The role of fuel cells in energy storage," *Journal of Power Sources*, vol. 86, no. 12, pp. 74–83, 2000.
- [73] S. C. Smith, P. K. Sen Sr, and B. Kroposki Sr, "Advancement of energy storage devices and applications in electrical power system," in *Power and Energy Society General Meeting-Conversion and Delivery of Electrical Energy in the 21st Century, 2008 IEEE*, pp. 1–8, IEEE.
- [74] D. Anderson and M. Leach, "Harvesting and redistributing renewable energy: on the role of gas and electricity grids to overcome intermittency through the generation and storage of hydrogen," *Energy policy*, vol. 32, no. 14, pp. 1603–1614, 2004.
- [75] P. Denholm and G. L. Kulcinski, "Life cycle energy requirements and greenhouse gas emissions from large scale energy storage systems," *Energy Conversion and Management*, vol. 45, no. 13, pp. 2153–2172, 2004.
- [76] C. Schaber, P. Mazza, and R. Hammerschlag, "Utility-scale storage of renewable energy," *The Electricity Journal*, vol. 17, no. 6, pp. 21–29, 2004.
- [77] D. Lilley, "Adiabatic Flame Temperature Calculation," in *1st International Energy Conversion Engineering Conference (IECEC)*, p. 5979.
- [78] D. Erickson, S. Day, and R. Doyle, "Design Considerations for Heated Gas Fuel," report, GE Power Systems.
- [79] A. Rao, D. Dewanji, and M. Gallo, "Heat Exchangers AE4237 (Lectures 4 and 5), HT Basics Part 1 and 2," 2013.
- [80] University of Pennsylvania - School of Engineering and Applied Science, "External Flow Correlations." Available at: "<http://www.seas.upenn.edu/~meam333/correlation/CorrelationsList.pdf>". Accessed online: 03-05-2016.
- [81] B. Wischnewsk, "Calculation of thermodynamic state variables of air." Available at: "http://www.peacesoftware.de/einigewerte/calc_luft.php5". Accessed online: 04-08-2016.
- [82] B. Wischnewsk, "Calculation of thermodynamic state variables of methane." Available at: "http://www.peacesoftware.de/einigewerte/calc_luft.php5". Accessed online: 04-08-2016.
- [83] National Institute of Standards and Technology, "Isothermal Properties for Methane." Available at: "http://webbook.nist.gov/cgi/fluid.cgi?T=160&PLow=1&PHigh=18&PInc=17&Applet=on&Digits=5&ID=C74828&Action=Load&Type=IsoTherm&TUnit=C&PUnit=bar&DUnit=kg%2Fm3&HUnit=kJ%2Fkg&WUnit=m%2Fs&VisUnit=Pa*s&STUnit=N%2Fm&RefState=DEF". Accessed online: 04-08-2016.
- [84] Industrial Refrigeration Consortium, "Fluid Property Calculator." Available at: "<https://www.irc.wisc.edu/properties/>". Accessed online: 04-08-2016.
- [85] Enerji Servis, "Natural Gas Preheaters." Accessed online: howpublished = Available at: "http://enerjiservis.power-serv.com/?page_id=173", type = Web Page.
- [86] DURR, "Gas preheaters for gas pressure regulating stations and gas relaxation systems ." Available at: "<http://www.durr-thermeco2.com/en/applications/item/757-gas-preheaters-for-gas-pressure-regulating-stations-and-gas-relaxation-systems>". Accessed online: 04-08-2016.
- [87] Y. B. Tao and Y. L. He, "Numerical study on performance enhancement of shell-and-tube latent heat storage unit," *International Communications in Heat and Mass Transfer*, vol. 67, pp. 147–152, 2015.
- [88] A. S. Fleischer, *Thermal Energy Storage Using Phase Change Materials: Fundamentals and Applications*. Springer, 2015.
- [89] K. Thakare and A. G. Bhave, "Review on latent heat storage and problems associated with phase change material," *International Journal of Research in Engineering and Technology*, vol. 4, pp. 176–182, 2015.

- [90] B. Zalba, J. M. Marín, L. F. Cabeza, and H. Mehling, “Review on thermal energy storage with phase change: materials, heat transfer analysis and applications,” *Applied Thermal Engineering*, vol. 23, no. 3, pp. 251–283, 2003.
- [91] “Phase Change Material Products Limited.” Available at: ”<http://www.pcmproducts.net/>”. Accessed online: 03-08-2016.
- [92] S. D. Sharma and K. Sagara, “Latent heat storage materials and systems: a review,” *International Journal of Green Energy*, vol. 2, no. 1, pp. 1–56, 2005.
- [93] M. Kenisarin and K. Mahkamov, “Solar energy storage using phase change materials,” *Renewable and Sustainable Energy Reviews*, vol. 11, no. 9, pp. 1913–1965, 2007.
- [94] Phase Change Material Products Limited, “PlusICE Phase Change Materials.” Available at: ”<http://www.pcmproducts.net/files/PlusICE%20Range-2013.pdf>”. Accessed online: 03-08-2016.
- [95] H. Mehling and L. F. Cabeza, *Heat and cold storage with PCM*. Springer, 2008.
- [96] A. Elgafy, O. Mesalhy, and K. Lafdi, “Numerical and experimental investigations of melting and solidification processes of high melting point PCM in a cylindrical enclosure,” *Journal of heat transfer*, vol. 126, no. 5, pp. 869–875, 2004.
- [97] R.-T. Lee and W.-Y. Chiou, “Finite-element analysis of phase-change problems using multilevel techniques,” *Numerical Heat Transfer*, vol. 27, no. 3, pp. 277–290, 1995.
- [98] *VDI Heat Atlas*. Springer, 2010.
- [99] M. Costa, D. Buddhi, and A. Oliva, “Numerical simulation of a latent heat thermal energy storage system with enhanced heat conduction,” *Energy Conversion and Management*, vol. 39, no. 34, pp. 319–330, 1998.
- [100] P. Talukdar, “Natural/Free Convection (lecture slides).”
- [101] M. Lacroix, “Numerical simulation of a shell-and-tube latent heat thermal energy storage unit,” *Solar Energy*, vol. 50, no. 4, pp. 357–367, 1993.
- [102] Y. A. Cengel and J. G. Afshin, *Heat and Mass Transfer: Fundamentals and Applications Fourth Edition*. McGraw-Hill, 2011.
- [103] Y. Zhang and A. Faghri, “Heat transfer enhancement in latent heat thermal energy storage system by using the internally finned tube,” *International Journal of Heat and Mass Transfer*, vol. 39, no. 15, pp. 3165–3173, 1996.
- [104] Z. Gong and A. S. Mujumdar, “Finite-element analysis of cyclic heat transfer in a shell-and-tube latent heat energy storage exchanger,” *Applied Thermal Engineering*, vol. 17, no. 6, pp. 583–591, 1997.
- [105] Eurostat, “Gas prices by type of user.” Available at: ”<http://ec.europa.eu/eurostat/tgm/refreshMapView.do?tab=map&plugin=1&init=1&toolbox=types&pcode=ten00118&language=en#>”. Accessed online: 03-08-2016.
- [106] European Union Committee, “The EU Emissions Trading System (EU ETS),” report, 2013.
- [107] European Energy Exchange, “ Results EUA Primary Auction Spot .” Available at: ”<https://www.eex.com/en/market-data/emission-allowances/auction-market/european-emission-allowances-auction/european-emission-allowances-auction-download>”. Accessed online: 03-08-2016.
- [108] J. Kosny, N. Shukla, and A. Fallahi, “Cost Analysis of Simple Phase Change Material-Enhanced Building Envelopes in Southern U.S. Climates,” report, U.S. Department of Energy, 2013.
- [109] European Central Bank, “Inflation and the Euro.” Available at: ”<https://www.ecb.europa.eu/stats/prices/hicp/html/inflation.en.html>”. Accessed online: 04-08-2016.
- [110] Centraal Bureau voor de Statistiek, “Inflatie voor het eerst in bijna 30 jaar negatief.” Available at: ”<https://www.cbs.nl/nl-nl/nieuws/2016/31/inflatie-voor-het-eerst-in-bijna-30-jaar-negatief>”. Accessed online: 04-08-2016.
- [111] P. Morthorst and S. Awerbuch, “The Economics of Wind Energy,” report, 2009.
- [112] International Renewable Energy Agency, “Renewable Energy Technologies: Cost Analysis Series,” report, 2012.
- [113] G. Doyle and G. Vantsiotis, “Costs of low-carbon generation technologies,” report, Mott MacDonald, 2011.
- [114] Netherlands Aerospace Centre, “GSP 11 User Manual,” report, 2016.

- [115] ThermoFlow, “Fully-flexible design and simulation of combined cycles, cogeneration systems, and other thermal power systems.” Accessed online: howpublished = Available at: ”http://www.thermoflow.com/combinedcycle_TFX.html”, type = Web Page.
- [116] L. M. Enrquez, “Comparison SAM ThermoFlow for Linear Fresnel (LF) Plants.”.

Appendix A

A.1 Hemweg 9 Operating Pattern (2015)

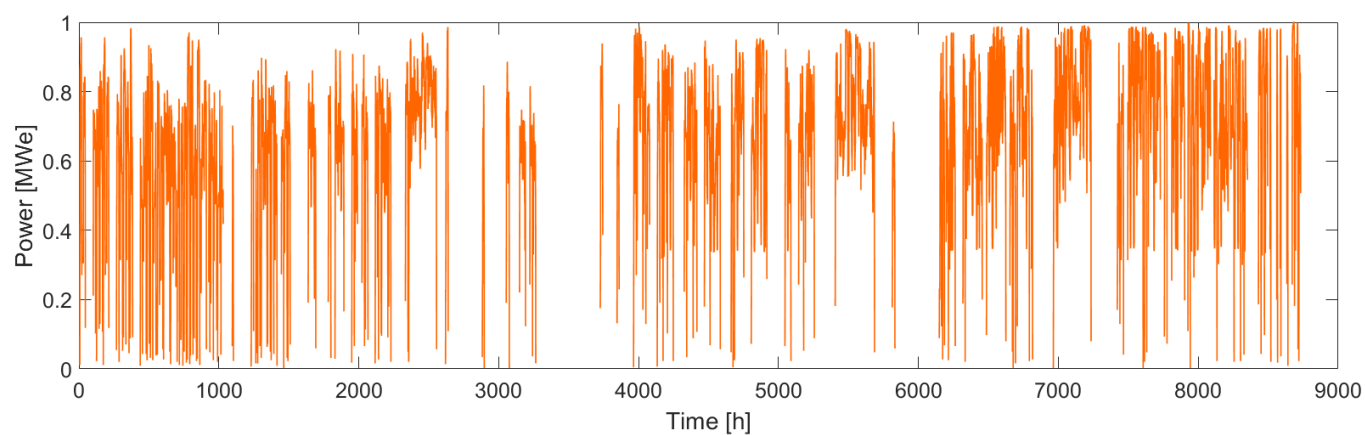


Figure A.1: Normalized operating pattern for the Hemweg 9 during the year 2015(36).

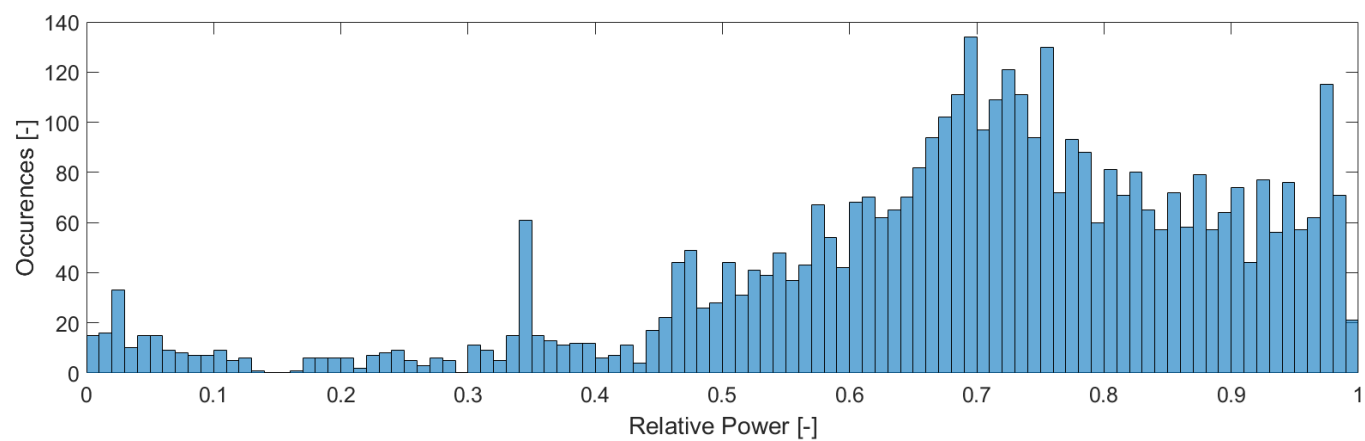


Figure A.2: Operating pattern occurrences for the Hemweg 9 during the year 2015(36).

A.2 Software Characteristics and Model Architectures

Table A.1: Combined-cycle modelling software characteristics.

Software	Computational approach	Source
GSP	GSP is based on non-dimensional modelling of different gas turbine components by means of aero-thermodynamic relations and steady state characteristics ("component maps"). Non-dimensional modelling uses a cross-section average for specific properties at both the inlet and exit of an apparatus. A design point is calculated first from a set of user specified design point data to size the gas turbine. The deviation from the design point is calculated by solving a set of non-linear differential equations. These equations are determined by the mass balance, heat balance, the equation for conservation of momentum and the power balance for each separate component.	(114)
THERMOFLEX	THERMOFLEX is a modular program with a graphical interface that allows to create a model from icons representing a specific component. The program can simulate both design and off-design simulation. It uses steady state characteristics to model compressor and turbine performance. Aero-thermodynamic relations are used to compute component performance such as the Dittus-bolter equation to compute the HTC.	(115; 116)
Cycle-Tempo	Uses mass, molar and energy balances to compute thermodynamic properties, gas compositions and mass flows. Cycle-Tempo uses predefined compositions for air, natural gas and flue gas to compute flow properties throughout the systems. Relations are used for the thermodynamic properties for both steam and water. No compressor or turbine performance maps are used.	(41)

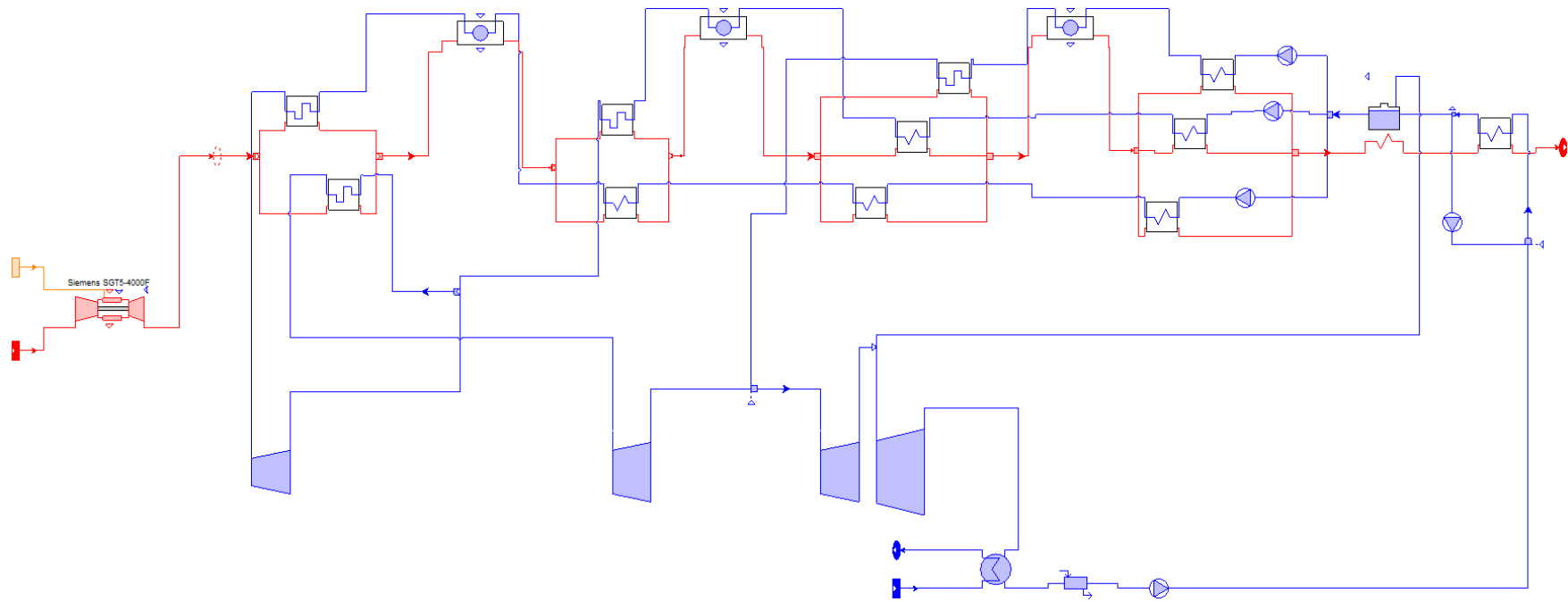


Figure A.3: Combined-cycle model architecture in THERMOFLEX.

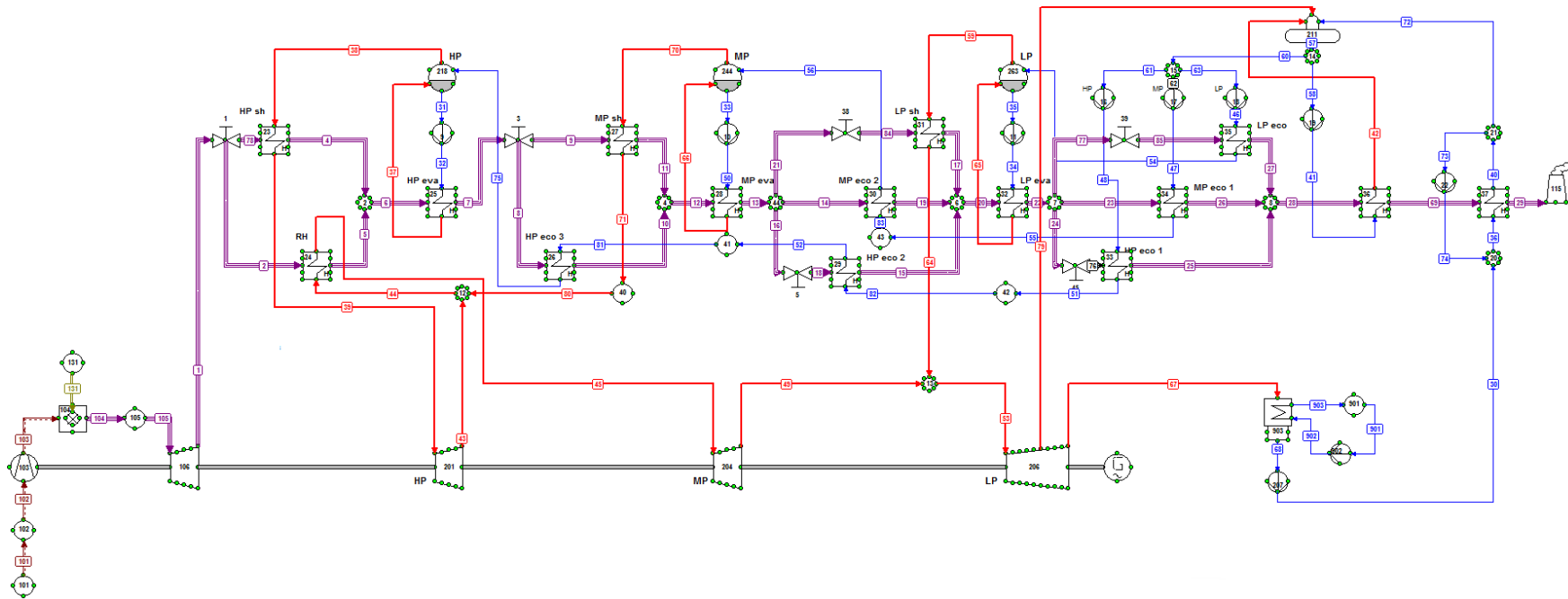


Figure A.4: Combined-cycle model architecture in Cycle-Tempo.

A.3 Gas Turbine and Combined-cycle Simulation Settings

Table A.2: Gas turbine simulation settings.

Parameter	THERMOFLEX	GSP	Cycle-Tempo	Unit
General				
Design gross power output	289.996	289.996	289.996	[MWe]
Inlet				
Design mass flow	670.70	670.700	670.680	[kg/s]
Pressure ratio	0.997	0.990	0.990	[-]
Compressor				
Design rotor speed	3000	3000	3000	[rpm]
Design gear ratio	-	1.000	-	[-]
Design pressure ratio	17.200	17.200	17.200	[-]
Design efficiency	0.890	0.890	0.890	[-]
Heat transfer fraction	-	0.500	-	[-]
dMass flow / dAngle	-	2.00	-	[%]
dM(PR-1) / dAngle	-	0.00	-	[%]
dETA _w / dAngle ²	-	-0.01	-	[%]
Bleed fraction	0.0779	0.0779	0.0779	[-]
Combustion chamber				
Fuel mass flow		19.120	19.120	[kg/s]
Design combustion efficiency	1	0.995	0.995	[-]
Design point rel. pressure loss	0.050	0.050	0.050	[-]
Design fuel	Slochteren natural gas	Slochteren natural gas	Slochteren natural gas	[-]
Turbine				
Shaft number	1	1	1	[-]
Design rotor speed	3000	3000	3000	[RPM]
Design gear ratio	-	1.000	-	[-]
Design efficiency		0.9097	0.965	[-]
Generator				
Design efficiency	0.986	0.990	0.990	[-]

Table A.3: Combined-cycle simulation settings.

Parameter	THERMOFLEX	Unit
General		
Design gross power output	427	[MWe]
Heat recovery steam generator		
HP steam temperature	565	[°C]
HP steam pressure	125	[bar]
HP evaporator pinch point	15	[°C]
MP steam temperature	565	[°C]
MP steam pressure	30	[bar]
MP evaporator pinch point	12	[°C]
LP steam temperature	300	[°C]
LP steam pressure	5	[bar]
LP evaporator pinch point	20	[°C]
Water side pressure drop	1	[%]
Gas side pressure drop (evaporators)	1	[mbar]
Gas side pressure drop (other)	4	[mbar]
Pump isentropic efficiency	80	[%]
Pump mechanical efficiency	97	[%]
Steam turbines		
HP mechanical efficiency	99.8	[%]
HP design rotor speed	3000	[RPM]
MP mechanical efficiency	99.8	[%]
MP design rotor speed	3000	[RPM]
LP mechanical efficiency	99.8	[%]
LP design rotor speed	3000	[RPM]
Condenser		
Pressure	0.27	[bar]
Minimum pinch	1	[°C]
Pump efficiency	80	[%]
Generator		
Design efficiency	0.986	[-]

A.4 Gas Turbine Performance Literature

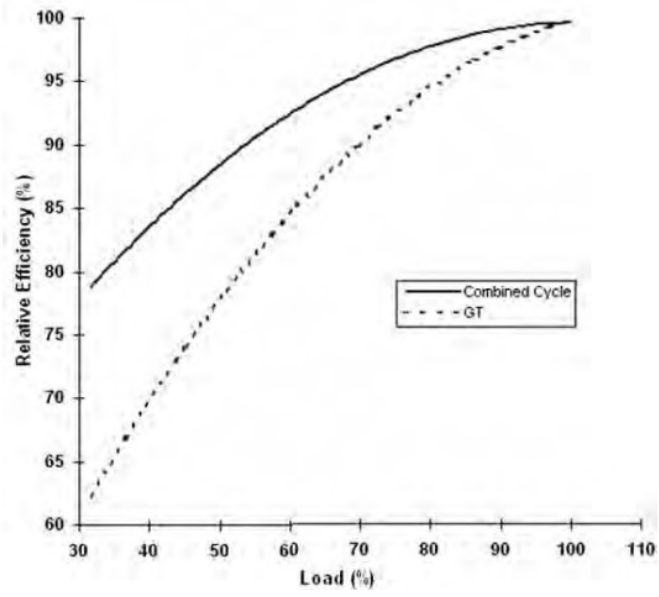


Figure A.5: Part-load efficiencies for the gas turbine and combined-cycle(26).

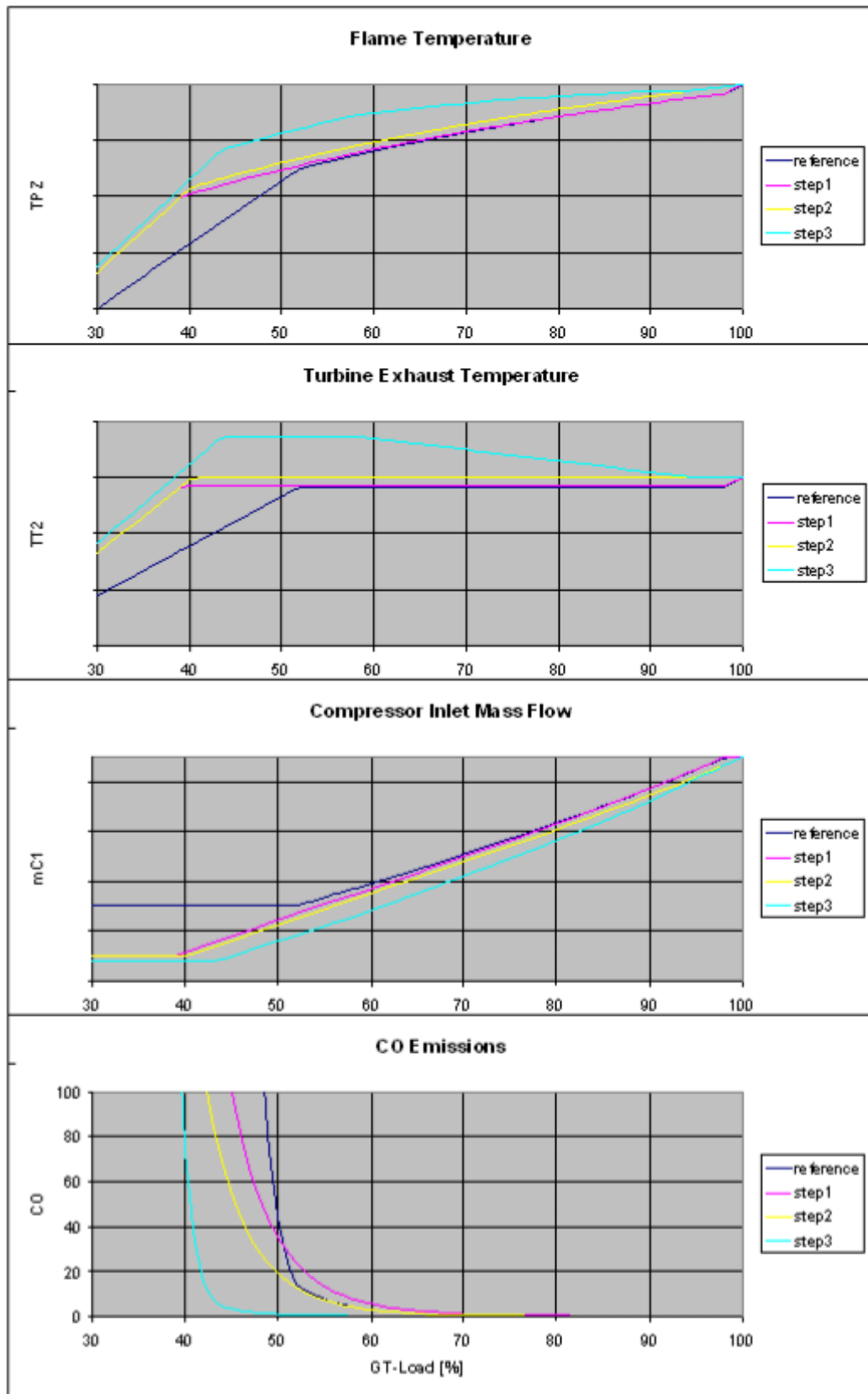


Figure A.6: Influence of SGT5-4000F development steps. Step one allows a further decrease of minimum compressor air mass flow. Step two includes a modified burner design which enabled a high exhaust gas temperature. Step three lead to a further increase in turbine exhaust temperature(47).

A.5 Temperature-density Curve for Methane

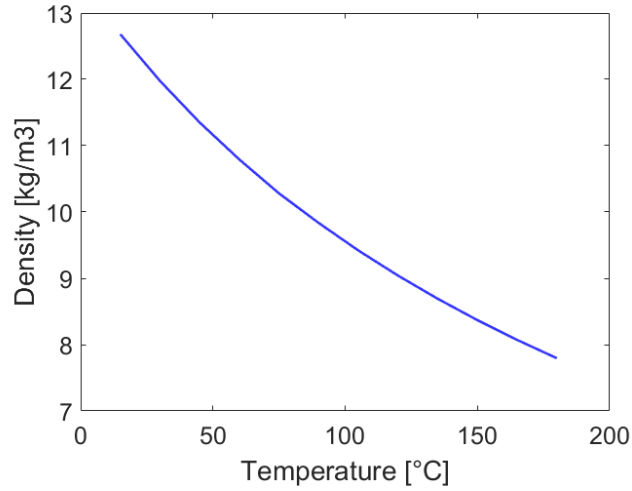


Figure A.7: Temperature-density curve for methane at 18.25 bar(82).

A.6 Grid Convergence Studies for Swept Parameters

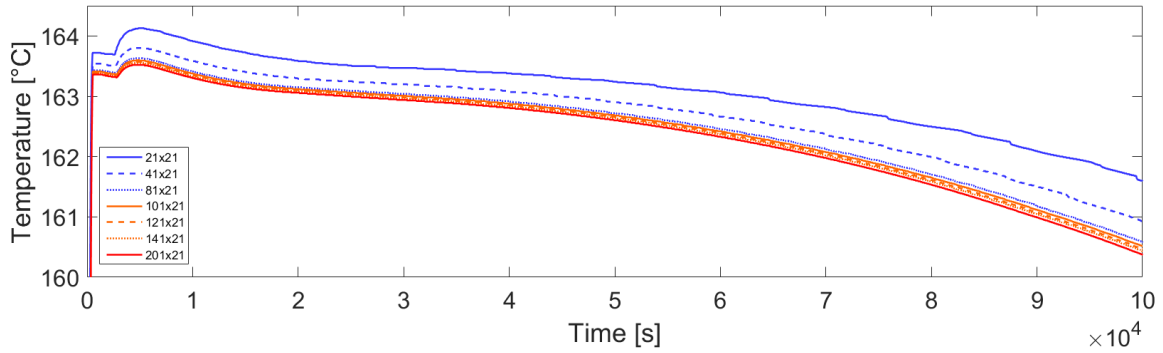


Figure A.8: Convergence study for the longest module length.

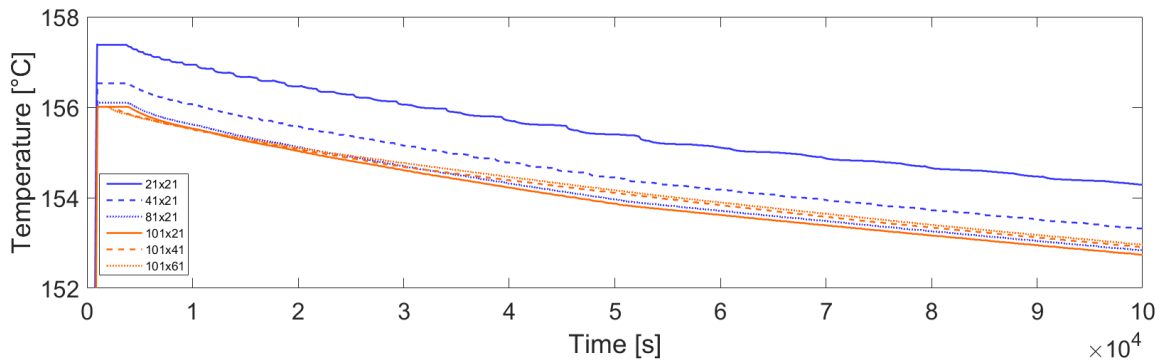


Figure A.9: Convergence study for the largest module inner radius.

